

**KOCAELİ UNIVERSITY  
GRADUATE SCHOOL OF NATURAL AND APPLIED  
SCIENCES**

**DEPARTMENT OF MECHATRONICS ENGINEERING**

**MASTER OF SCIENCE THESIS**

**DESIGN AND ANALYSIS OF 60KW RADIAL FLUX  
ELECTRICALLY EXCITED EDDY CURRENT BRAKE FOR  
ELECTRICAL TRUCK**

**MUSTAFA BARIS TOPCUOGLU**

**KOCAELİ 2019**

**KOCAELI UNIVERSITY**  
**GRADUATE SCHOOL OF NATURAL AND APPLIED SCIENCES**  
**DEPARTMENT OF MECHATRONICS ENGINEERING**

**MASTER OF SCIENCE THESIS**

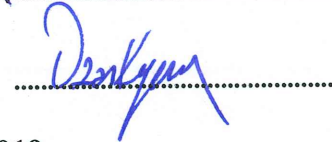
**DESIGN AND ANALYSIS OF 60KW RADIAL FLUX  
ELECTRICALLY EXCITED EDDY CURRENT BRAKE FOR  
ELECTRICAL TRUCK**

**MUSTAFA BARIŞ TOPÇUOĞLU**

**Prof. Dr. Zafer BİNGÜL**  
Advisor, Kocaeli Univ.

**Assoc. Prof. Metin AYDIN**  
Jury Member, Kocaeli Univ.

**Assist. Prof. Ozan KEYSAN**  
Jury Member, Middle East Technical U.



**Thesis Defended on: 24.12.2019**

## **FOREWORD**

I would like to thank to my father, Safa TOPCUOGLU. He taught me that the first step in solution is to understand the problem entirely. In my first school years, I was asking math questions to him. By closing the book, he had been asking me to explain the problems, and then we were finding the solution. This was my first step on engineering. Thank you, Dad, for everything which you teach me and thank you for everything you've contributed to my life.

I express my gratitude to my advisor Professor Dr.Zafer BINGUL. His vision and suggestions did great contribution to my paper and thesis work. I am glad to work such a good advisor.

I am glad to get advice from Mehmet GULEC for my paper and thesis work. At the beginning of my study, he directed my paper and thesis into being well prepared and systematical research.

I would like to thank to my brother Onur COBANOGLU for his perfect contribution to my paper and thesis. He reminded me that an academics work has to answer questions which are who, what, where, when, how and why. I updated my whole works by thinking that questions. He also taught me usage of academics language.

I wish to thank my sister Merve TOPCUOGLU for her great support and guidance for me. She taught me significant mathematical terms and equations before school. It encouraged me on engineering at initial. That was the reason for me to love engineering.

I am very grateful to my mother Dilsad ERDOGAN for her dedicated and attentive support. Whenever I need, she always helps me to get motivation, to get inspiration and feel serenity. I'm grateful for every second I spend with her.

I would like to thank Ozan KEYSAN, Assistant Professor at METU. He directed me to several companies and academic studies. I also learnt a lot of machine design knowledge from the lessons and the documents that he prepared. I started to learn the software which is the basis of this thesis in the machine laboratory.

I wish to thank structural analysis team manager Tayfun GULEM and Group Sales Manager Serkan YILMAZ for demo license supply. I am also grateful to Umut GUNDOGAR for his endless technical support on Ansys MAXWELL.

I wish to thank Mustafa ALTINTAŞ for his endless support at work and for his friendship. I express my gratitude to my colleague Ozgun KUCUK for his thermal design support. Finally, I thank to FEV Turkey Company and Dr Murat DEMIRCI for them to provide me a great opportunity to work on the latest EV automotive projects. This chance expanded my vision.

September – 2019

Mustafa Baris TOPCUOGLU

## CONTENTS

FOREWORD.....	i
CONTENTS .....	ii
LIST OF FIGURES .....	iv
LIST OF TABLES.....	vii
LIST OF SYMBOLS AND ABBREVIATIONS.....	viii
ABSTRACT .....	xi
ÖZET .....	xii
INTRODUCTION .....	1
1. SECONDARY BRAKES IN TRUCKS .....	3
1.1. Conventional Retarders .....	3
1.1.1. Jake brakes.....	4
1.1.2. Back pressure brakes.....	5
1.1.3. Hydro-mechanic retarders .....	6
1.1.4. Low voltage eddy current brakes .....	7
1.2. New Generation Truck Retarders .....	8
1.2.1. Regenerative brake integrated with super-capacitor module .....	8
1.2.2. Regenerative brake integrated with resistor module .....	10
1.2.3. Regenerative brake integrated with eddy current brake.....	11
1.3. Thesis Objective .....	15
1.4. Thesis Method.....	16
1.5. Requirements for the Proposed Eddy Current Brake .....	16
1.5.1. Nominal torque and speed values .....	16
1.5.2. Nominal electrical parameters as an input .....	19
1.5.3. Dimensions.....	19
2. THEORY AND MODELLING OF PROPOSED GEOMETRY .....	20
2.1. Magnetic Analysis by Magnetic Equivalent Circuit for Proposed Structure.....	21
2.2. Eddy Current Brake Theory and Modelling for Proposed Structure.....	23
2.3. Regenerative Brake on Electric Vehicle.....	26
2.4. Half bridge Controller and Control Method .....	27
2.5. Thermal Lumped Parameter Model For The Proposed Geometry.....	29
2.5.1. Thermal Model of ECB .....	31
2.6. Material Selection.....	35
2.6.1. Core Material .....	35
2.6.2. Disc Material.....	37
2.6.3. Heat sink.....	39
2.6.4. Fan .....	40
3. COMPARISON OF THE GEOMETRICAL VARIATIONS ON PROPOSED ECB BY ANALYTICAL CALCULATIONS AND FEA SIMULATIONS .....	41
3.1. Disc Conductivity Comparison.....	41
3.2. Pole Pitch Ratio .....	44
3.2.1. Small scaled prototype comparison on pole pitch ratio .....	47

3.3. Number of Pole .....	49
3.3.1. Small scaled prototype comparison on number of poles.....	52
3.4. Disc Thickness .....	54
3.4.1. Small scaled prototype comparison on disc thicknesses .....	56
3.5. Airgap Distance .....	56
3.5.1. Small scaled prototype comparison on number of poles.....	58
3.6. Rotor Thickness.....	59
3.7. Thermal Calculation .....	60
4. RESULTS .....	62
4.1. Final Geometry and Parameters of Designed ECB.....	62
4.2. Controlling Proposed ECB by Constant Current .....	63
4.3. Results and Conclusions.....	64
4.3.1. Performed analysis .....	64
4.3.2. Results .....	65
5. CONCLUSIONS AND FUTURE WORKS.....	76
REFERENCES .....	78
PERSONAL PUBLICATION.....	83
CURRICULUM VITAE .....	84

## LIST OF FIGURES

Figure 1.1.	Secondary brake classification.....	3
Figure 1.2.	Engine diesel cycles .....	4
Figure 1.3.	Schematic of standard technology jake brake retarder for a 6-cylinder engine .....	4
Figure 1.4.	Exhaust brake.....	5
Figure 1.5.	Engine brake performance ranges from various engine tests and simulation results .....	5
Figure 1.6.	(a) Voith Retarder VR 123 and (b) Cross section view .....	6
Figure 1.7.	Brake torque vs speed curve of VR 123 retarder .....	6
Figure 1.8.	(a)AD 50 90 eddy current retarder (b)torque vs speed curve .....	7
Figure 1.9.	Brake system.....	9
Figure 1.10.	Brake convertor.....	9
Figure 1.11.	Configuration of the FC-battery-powered hybrid system for the tramway.....	10
Figure 1.12.	PowerMela Break Chopper: (a) Module (b) Diagram .....	11
Figure 1.13.	Proposed ECB usage for electrical vehicles.....	11
Figure 1.14.	Classification of eddy current brake .....	13
Figure 1.15.	At maximum slope angle, the forces effecting on the truck .....	17
Figure 2.1.	Proposed eddy current brake system integrated on vehicle axe .....	20
Figure 2.2.	Cross section of proposed ECB .....	21
Figure 2.3.	Linear projection of proposed geometry and flux lines .....	22
Figure 2.4.	Eddy current brake regions .....	24
Figure 2.5.	Four quadrant operation modes of electric motor .....	27
Figure 2.6.	One phase eddy current and one leg chopper circuit IGBT (a) on and (b) off.....	28
Figure 2.7.	Constant current control .....	28
Figure 2.8.	Cross section for thermal analysis .....	29
Figure 2.9.	Heat transfer way .....	30
Figure 2.10.	Heat transfer for cylindrical parts .....	31
Figure 2.11.	Thermal lumped model of the proposed ECB .....	32
Figure 2.12.	Thermal conduction and convection direction .....	34
Figure 2.13.	B H curve of steel 1010 .....	36
Figure 2.14.	Thermal and electrical conductivity of the disc material at 20 ° C .....	37
Figure 2.15.	Electrical resistivity versus temperature for disc material .....	38
Figure 2.16.	Conductivity of the disc material vs critical speed .....	38
Figure 2.17.	Cost for different disc materials .....	39
Figure 2.18.	Linear projection of proposed 3D cylindrical heat sink .....	39
Figure 2.19.	Selected fan blades to have a reference cfm ratio .....	40
Figure 3.1.	Torque speed curve for different disc material obtained by 2D FEA .....	42
Figure 3.2.	Maximum torque and critical speed values obtained by 2D FEA .....	42

Figure 3.3. Torque speed curve for different disc material obtained by analytical calculations .....	43
Figure 3.4. Determination of angle for pole pitch calculation.....	44
Figure 3.5. Torque vs speed curves of different pole pitch ratio obtained by 2D FEA .....	45
Figure 3.6. Maximum torque and critical speed values of different pole pitch ratios obtained by 2D FEA .....	46
Figure 3.7. Torque speed curve for different pole pitch ratio obtained by analytical calculations .....	46
Figure 3.8. Small scaled ECB torque vs pole pitch ratio curve at 1000 min <sup>-1</sup> obtained by 3D FEA.....	49
Figure 3.9. Torque speed curve for different number of poles obtained by 2D FEA .....	50
Figure 3.10. Maximum torque and critical speed values for different pole numbers obtained by 2D FEA.....	51
Figure 3.11. Torque speed curve for different pole numbers obtained by analytical calculations .....	51
Figure 3.12. Total torque vs number of poles at 1000 min <sup>-1</sup> obtained by 3D FEA.....	53
Figure 3.13. B <sub>gap</sub> max vs number of poles at 1000 min <sup>-1</sup> obtained by 3D FEA.....	53
Figure 3.14. Torque speed curve for different disc thicknesses obtained by 2D FEA.....	54
Figure 3.15. Maximum speed and critical speed for different disc thicknesses obtained by 2D FEA.....	55
Figure 3.16. Torque speed curve for different disc thicknesses obtained by analytical calculations .....	55
Figure 3.17. Speed vs torque curve with different disc thickness at 1000 min <sup>-1</sup> obtained by 3D FEA.....	56
Figure 3.18. Torque speed curve for different airgap obtained by 2D FEA.....	57
Figure 3.19. Maximum speed and critical speed for different airgaps obtained by 2D FEA .....	57
Figure 3.20. Torque speed curve for different airgap obtained by analytical calculations.....	58
Figure 3.21. Air gap distance vs total torque obtained by 2D FEA .....	59
Figure 3.22. Speed vs torque graph for different rotor yoke thicknesses obtained by 2D FEA.....	59
Figure 3.23. Critical speed and maximum torque vs rotor thickness graph obtained by 2D FEA.....	60
Figure 4.1. 3D View of designed ECB.....	63
Figure 4.2. Torque speed curve for each current density ratio obtained by 3D FEA.....	63
Figure 4.3. Performed analysis .....	65
Figure 4.4. Geometrical variation result for each step.....	65
Figure 4.5. Torque vs time response curve obtained by 3D FEA .....	66
Figure 4.6. Comparison of the torque speed curve for 2D FE, 3D FE and analytical calculation .....	66
Figure 4.7. Flux density on the disc at t=0 obtained by FEA.....	68

Figure 4.8. Flux density on the disc at $t=9.7\text{ms}$ steady state obtained by FEA.....	69
Figure 4.9. Contour drawing of the flux density on a line in the middle of the disc obtained by FEA .....	70
Figure 4.10. 3D drawing of the flux density on the line obtained by FEA.....	70
Figure 4.11. Contour drawing of the eddy current density on the line obtained by FEA.....	71
Figure 4.12. 3D drawing of the eddy current on the line obtained by FEA.....	71
Figure 4.13. Magnetic flux density in the stator core at $100\text{ min}^{-1}$ obtained by FEA.....	71
Figure 4.14. Magnetic flux density in the stator core at $664\text{ min}^{-1}$ obtained by FEA.....	71
Figure 4.15. 3D view of eddy current vectors obtained by FEA.....	74
Figure 4.16. Closer 3D view of eddy current vectors obtained by FEA.....	74
Figure 4.17. 3D drawing of eddy current vectors for the small scaled of the ECB obtained by FEA .....	75





## LIST OF TABLES

Table 1.1.	Numerical value for brake requirement calculations.....	18
Table 1.2.	Numerical results of brake requirement .....	19
Table 1.3.	Numerical value used in the volume calculations.....	19
Table 2.1.	Core material comparison .....	36
Table 3.1.	Parameters used in analytical calculations for different disc materials.....	43
Table 3.2.	Parameters used in analytical calculations for different pole pitch ratios .....	47
Table 3.3.	Prototype ECB dimensions and nominal design parameter .....	48
Table 3.4.	Parameters used in analytical calculations for different pole numbers.....	52
Table 3.5.	Parameters used in analytical calculations for different disc thicknesses.....	55
Table 3.6.	Parameters used in analytical calculations for different air gaps .....	58
Table 3.7.	Thermal calculation results for final geometry.....	60
Table 3.8.	Temperature findings for 60kW continuous brake operation.....	61
Table 4.1.	Final design for proposed ECB.....	62
Table 4.2.	Comparison of the retarders.....	67

## LIST OF SYMBOLS AND ABBREVIATIONS

A	: Area, (m <sup>2</sup> )
A <sub>g</sub>	: Airgap area, (m <sup>2</sup> )
A <sub>v</sub>	: Front area of truck, (m <sup>2</sup> )
B	: Flux density, (T)
B <sub>net</sub>	: Net flux density in the disc, (T)
B <sub>al</sub>	: Aluminum flux density, (T)
B <sub>disc</sub>	: Aluminum flux density, (T)
B <sub>g</sub>	: Airgap flux density, (T)
D	: Diameter, (m)
E	: Electric potential, (V/m)
F	: Electromotive force, (A.t)
F <sub>air</sub>	: Air resistance force parallel to road, (N)
F <sub>pr</sub>	: Force parallel to road, (N)
F <sub>fr</sub>	: Friction force, (N)
I <sub>EC</sub>	: Generated eddy current in aluminum disc, (A)
J	: Moment of inertia, (kg.m <sup>2</sup> )
J	: Current density, (A/mm <sup>2</sup> )
K	: Correction coefficient for the thesis analytical torque approach
L	: Inductance of winding
L <sub>c</sub>	: Characteristic length
M <sub>t</sub>	: Gross weight of the truck, (kg)
N	: Number of turn
P <sub>iECB</sub>	: Power input of ECB, (W)
P <sub>mech</sub>	: Mechanical power, (W)
P <sub>winding</sub>	: Thermal power at windings, (W)
P <sub>disc</sub>	: Generated power in disc, (W)
Q <sub>cond</sub>	: Power of thermal conduction, (W)
R <sub>alu/2</sub>	: Half of thermal resistance of aluminum disc, (°C/W)
R <sub>amb</sub>	: Resistance of a material at ambient temperature, (ohm)
R <sub>cu</sub>	: Thermal convection resistance of copper winding, (°C/W)
R <sub>iso</sub>	: Thermal resistance of winding isolation, (°C/W)
R <sub>m</sub>	: Reynolds number
R <sub>st-in</sub>	: Inner radius of stator, (m)
R <sub>st-out</sub>	: Outer radius of stator, (m)
R <sub>t</sub>	: Radius of wheel, (m)
R <sub>th</sub>	: Thermal resistance, (°C/W)
R <sub>wh</sub>	: Wheel radius, (m)
T	: Temperature, (°C)
T <sub>b</sub>	: Brake torque, (Nm)
T <sub>m</sub>	: e-motor torque, (Nm)
T <sub>br</sub>	: Torque at shaft, (Nm)
T <sub>w</sub>	: Torque at wheel, (Nm)

$V_L$	: Voltage applied to terminals of brake chopper circuit, (V)
$c_d$	: Coefficient of air drag
$c_r$	: Coefficient of rolling resistance
$g$	: Gravitational constant, ( $m/s^2$ )
$h$	: Thermal convection coefficient, ( $W/m^2K$ )
$h_{sink}$	: Thermal convection coefficient of heatsink, ( $W/m^2K$ )
$i$	: Current, (A)
$i_L$	: Winding current, (A)
$i_{ripple}$	: Ripple current of constant current control, (A)
$k$	: Thermal conduction heat transfer coefficient, ( $W/mK$ )
$l$	: Stator length, (m)
$p$	: Number of poles
$r_{cu}$	: Resistance of copper winding, (ohm)
$r_i$	: Inner radius, (m)
$r_o$	: Outer radius, (m)
$sh_r$	: Single speed transmission ratio
$t$	: Disc thickness, (m)
$t_{on}$	: Transistor stay on time, (second)
$v_c$	: Characteristic speed, (m/s)
$\vec{F}$	: Brake force on the rotor disc, (N)
$\mathcal{R}$	: Reluctance, ( $H^{-1}$ )
$\mathcal{R}_{yr}$	: Reluctance of rotor yoke, ( $H^{-1}$ )
$\mathcal{R}_{al}$	: Reluctance of aluminum disc, ( $H^{-1}$ )
$\mathcal{R}_g$	: Reluctance of air gap, ( $H^{-1}$ )
$\mathcal{R}_{tooth}$	: Reluctance of stator tooth, ( $H^{-1}$ )
$\mathcal{R}_{yst}$	: Reluctance of stator yoke, ( $H^{-1}$ )
$Q_{cond}$	: Conduction heat transfer, (W)
$\alpha$	: Slop angle of road, (degree)
$\alpha$	: Thermal resistance, (degree)
$i$	: Winding current, (A)
$v$	: Linear speed of the rotor, (m/s)
$v_{wh}$	: Wheel speed, ( $min^{-1}$ )
$v_{ve}$	: Vehicle speed, (m/s)
$v_{mm}$	: e-motor maximum speed, ( $min^{-1}$ )
$v_{shaft}$	: Shaft speed, ( $min^{-1}$ )
$w_{sh}$	: Radial speed, (rad/s)
$\varphi$	: Flux, (weber)
$\mu_0$	: Permeability of vacuum, (H/m)
$\mu_r$	: Relative permeability
$\mu_{eff}$	: Efficiency
$\delta$	: Skin depth, (m)
$\sigma$	: Electrical conductivity, (S/m)
$\sigma_{Ftan}$	: Tangential stress, (Pa)
$\tau$	: Pole pitch ratio
$\rho_{air}$	: Air density, ( $kg/m^3$ )
$\chi$	: Length to diameter ratio
$\odot$	: Current directed towards reader side

⊗ : Current reversely directed towards reader side

### **Abbreviations**

2D : Two Dimensional  
3D : Three Dimensional  
AFEE-ECB : Axial Flux Electrically Excited Eddy Current Brake  
ECB : Eddy Current Brake  
FEA : Finite Element Analysis  
CFD : Computational Fluids Dynamics  
CFM : Cubic Feet Per Minute  
LFM : Linear Feet Per Minute  
LV : Low Voltage  
RFEE-ECB : Radial Flux Electrically Excited Eddy Current Brake  
Rpm : Revolution Per Minute  
SOC : State of Charge

## **DESIGN AND ANALYSIS OF 60KW RADIAL FLUX ELECTRICALLY EXCITED EDDY CURRENT BRAKE FOR ELECTRICAL TRUCK**

### **ABSTRACT**

With the development of fully electric and hybrid vehicles, drive-by-wire which means that electrically controllable systems, begins to replace mechanical systems recently. Regenerative brake is one of the drive-by-systems. Because regenerative brake cannot operate when battery is in high state of charge, there must be complementary system working with regenerative brake according to electrical vehicle regulations. In the thesis, the complementary eddy current brakes were designed in two different power ranges. Electrical machine structure of these designs are radial flux electrically excited ECBs with rotor out-runner. First design has four poles,  $1000 \text{ min}^{-1}$  critical speed, maximum torque of 10 Nm. As its geometric structure, it has 70mm of outer radius, 2mm of air gap and 2mm of conductive disc thickness. Steel 1010 and aluminum are selected for core material and the conductive disc, respectively. Second design has six poles,  $950 \text{ min}^{-1}$  critical speed, maximum torque of 2600 Nm. It has 134 mm of outer radius, 1.5 mm of air gap and 1.5 mm of conductive disc thickness. Steel 1010 and aluminum alloy 220 are chosen for core material and conductive disc, respectively. In design, magnetic equivalent circuit based analytical calculations are performed. To analyze thermal characteristic of the design, analytical calculations were made. In order to investigate the effect of disc material, pole pitch ratio, pole number, disc thickness, air gap on brake torque, finite element analysis (FEA) were developed.

The proposed brake design has low response time, frictionless and quite working conditions as opposed to the conventional brake. This brake does not require maintenance and external supply. Due to it is electrically excited by regenerative brake power; it has no electrical energy shortage risk. Even if it has lower power density comparing the other brake solutions, it is not significant for heavy duty vehicles (trucks, off-road traction etc). Since there is no space constraint in this type of vehicles, the volume and weight of the brake will not be very important. Especially the brake disc is rotating during braking operation that this added cooling effect on the disk. This provides superiority on thermal feature of the proposed design.

**Keywords:** Finite Element Analysis, Radial Flux Electrically Excited High Voltage Eddy Current Brake, Retarders for Full Electric Heavy-duty Vehicle.

# ELEKTRİKLİ KAMYONLAR İÇİN 60KW ELEKTRİK UYARTIMLI RADYAL AKILI GİRDAP AKIM FRENİNİN TASARIMI VE ANALİZİ

## ÖZET

Tamamen elektrikli ve hibrit taşıtların geliştirilmesiyle, elektrikle kontrol edilebilen drive-by-wire sistemlerin, yakın zamanda mekanik sistemlerin yerini almaya başlamıştır. Rejeneratif fren de bu sistemlerden biridir. Yüksek gerilim batarya yüksek şarj durumundayken rejeneratif fren çalışmadığı için, elektrikli araç yönetmeliklerine göre rejeneratif fren ile çalışan tamamlayıcı bir sistem bulunmalıdır. Tezde, tamamlayıcı sistem olarak girdap akım frenleri iki farklı güç aralığında tasarlanmıştır. Bu tasarımların elektrikli makine yapısı, dıştan donen rotorlu ve elektrikli uyartımlı ECB'lerdir. İlk tasarım, dört kutuplu, 1000 dk-1 kritik hız ve maksimum 10 Nm tork değerine sahiptir. Geometrik yapı olarak 70mm dış yarıçapa, 2 mm hava boşluğuna ve 2mm iletken disk kalınlığına sahiptir. Çekirdek malzemesi ve iletken disk için sırasıyla çelik 1010 ve alüminyum seçilmiştir. İkinci tasarımın altı kutbu var, 950 dk-1 kritik hız, maksimum 2600 Nm tork. 134 mm dış yarıçapa, 1,5 mm hava boşluğu ve 1,5 mm iletken disk kalınlığına sahiptir. Çelik 1010 ve alüminyum alaşımı 220 sırasıyla çekirdek malzemesi ve iletken disk için seçilmiştir. Tasarımda manyetik eşdeğer devre bazlı analitik hesaplamalar yapıldı. Tasarımın termal karakteristiğini analiz etmek için analitik hesaplamalar yapıldı. Disk malzemesinin etkisini araştırmak için, kutup aralığı oranı, kutup sayısı, disk kalınlığı, fren torku üzerindeki hava boşluğu, sonlu elemanlar analizi (FEA) geliştirildi.

Önerilen fren tasarımı geleneksel frenin aksine düşük tepki süresine, sürtünmesiz ve daha uzun omurlu bir yapıya sahiptir. Bu fren bakım ve harici besleme gerektirmez. Rejeneratif fren gücü ile elektrikli olarak uyarıldığından; elektrik enerjisi kesilme riski yoktur. Diğer fren çözümlerine kıyasla daha düşük güç yoğunluğuna sahip olsa bile, ağır hizmet araçları (kamyonlar, arazi çekişi vb.) için yer kısıtlaması olmadığından, frenin hacmi ve ağırlığı çok önemli olmayacaktır. Özellikle fren disk frenleme işlemi sırasında dönmekte ve bu da disk üzerinde soğutma etkisi yaratmaktadır. Bu, önerilen tasarımın termal özelliklerinde bir üstünlük sağlar.

**Anahtar Kelimeler:** Sonlu Elemanlar Analizi, Radyal Akı Elektrikli Uyartımlı Yüksek Gerilim Girdap Akım Freni, Tam Elektrikli Ağır Vasıta İçin Frenler.

## **INTRODUCTION**

By severe environmental concerns, there is a huge technology shift on commercial vehicles from combustion engine powered vehicles to electric motor-powered vehicles. There are several reasons for the shift: Combustion engine powered vehicles creates severe air pollution by producing Carbon dioxide and other global warming gases [1]. Due to climate change and global warming, it is known that the world cannot continue by the same manner. In addition, semi-conductor, transistor and battery technologies have been significantly developing. 400 km range cars are available. Also new battery technologies such as lithium air battery researches promise 800km range for electric cars [2], [3]. Because of the reasons, fully electric car domination has begun and in future, only electric vehicles will exist on the roads. Prepared regulations, laws and taxes also indicate this change.

After the change, some modules will not be used. These are fuel tanks, fueled-engine, transmission; retarder brakes integrated with transmission. Instead of these, battery packages, electric motors, regenerative brake systems will be used. While this transform occurs, there should not be any safety or function loss for the vehicles because most of the automotive regulations and safety concerns remain same, but while regenerative brake system is being used place of retarder, a new safety fault condition takes form. The fault condition is that: Regenerative brake has a similar function like retarder. With this, ECE R13 [4] brake regulation appears to be achieved but in high state of charge condition, the battery cannot drain current from regenerative brake and the brake operation cannot occur. To overcome the problem, several method or modules are proposed in literature.

One of the methods is using supercapacitor [5]. In high state of charge condition of high voltage battery, the current coming from regenerative brake is stored in the capacitor. The module has high power sink capacity, but it has finite energy storage as batteries. Also, it requires additional DCDC converter for energy conversion.

Second method is using discharge resistor to consume the current coming from regenerative brake [6]. The system has no limit to current sink. It is also compact, lightweight. The critical point is that the system has a suitable thermal design.

In the thesis, another method is proposed. The method is usage of eddy current brake coupled with shaft. In high state of charge condition, the current produced by regenerative brake will be utilized on ECB. With that of usage, second brake is utilized to assist to regenerative brake. The possible advantage of the proposed solution is that: generated heat is dissipated by rotating part. Hence, convection resistance of the system may reduce, and system may have a better cooling capacity than other solutions. The proposed usage is shown in Figure 1.13.

Eddy current brakes have wide range of usage. They are used in railway transportation. Due to having no friction, it has no maintenance requirement [7,8]. In addition, elevator systems have this type of ECBs. Another type of ECBs is rotational type which is used in roller coasters, some climbing safety equipment and conventional trucks. In the trucks, the ECBs are powered from low voltage 24-volt batteries. Because of high electric current demand, this type of ECBs is not preferred in the market. Instead of it, oil-based retarder system integrated on shaft is used. The system also requires cooling high [9,10,11]. One drawback of the ECBs is that, at low speeds, they have limited or zero brake [12].



## 1. SECONDARY BRAKES IN TRUCKS

As mentioned before, with the powertrain change in the automotive market, some brakes systems will be not applicable, and some new brakes systems will be utilized. To see, advantages and disadvantages of this change, secondary brakes will be investigated in this part. Also, the new brake types which are either not used or rarely used will be represented. Secondary brakes in trucks can be classified in two groups as shown in Figure 1.1.

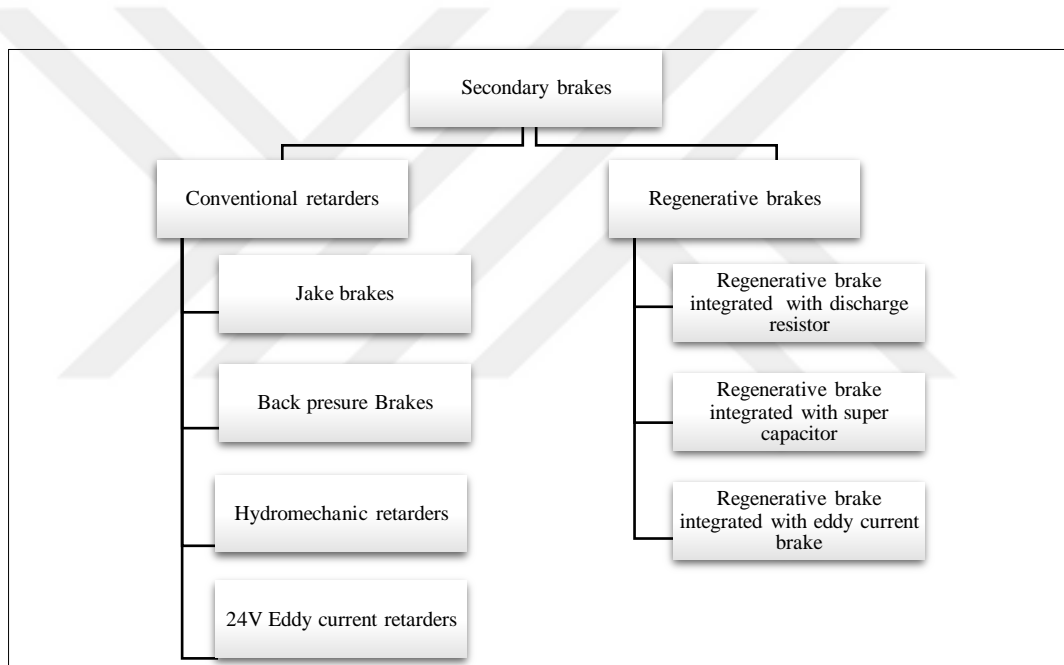


Figure 1.1. Secondary brake classification

### 1.1. Conventional Retarders

As mentioned, combustion engine integrated brakes will not be utilized in new generation trucks because combustion engine will be replaced with electrical motor. To see negative side of the change, these brakes must be investigated. There are four types of secondary brake systems which will be vanished in new generation trucks: low voltage ECB, hydro-mechanic retarder, Jake brake and back pressure brake.

### 1.1.1. Jake brakes

In commercial diesel engine performs four phases. The phases are seen in Figure 1.2. First is intake phase. In the phase, while stroke goes down, air enters the cylinder via suction valve. In second phase, the air is compressed while a stroke goes up. Then in third phase, with injected fuel combustion occurs and piston goes down. In fourth phase, combusted fuel is discarded via exhaust valve and cycle is completed.

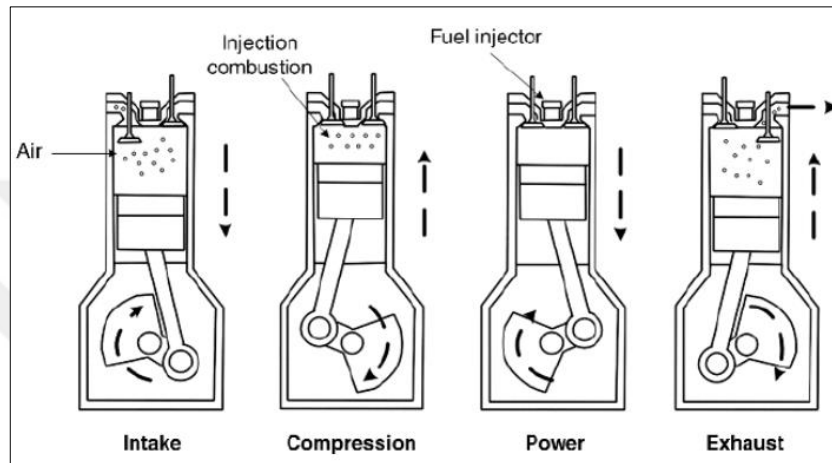


Figure 1.2.Engine diesel cycles [13]

Jake retarder working principle is directly related with engine working. In compression phase, exhaust valve needed to be closed in normal state, is opened in brake operation.

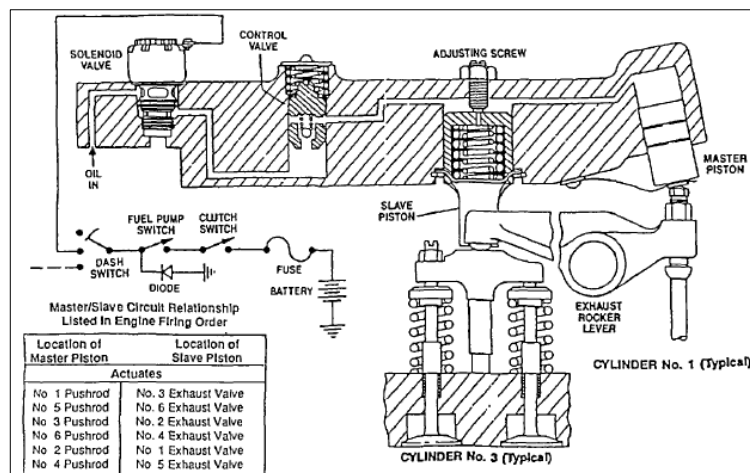


Figure 1.3.Schematic of standard technology jake brake retarder for a 6-cylinder engine [14]

Without fuel injection, intake air is discarded in a controlled way via exhaust valve. The air creates a vacuum effect and it causes to vehicle to slow down.

In 1992, Meistrick explains the working principle of standard Jacobs Jake retarder for 6-cylinder engine which is shown in Figure 1.3. When the solenoid valve is energized, the exhaust valve is opened with the master-slave pistons. Then it releases compressed air

### 1.1.2. Back pressure brakes

Back pressure brake performs in that way: a valve integrated with exhaust manifold controls and adjusts exhausted air. By increasing the flow resistance, it increases the pressure on exhaust manifold which causes to engine strokes to slow down.



Figure 1.4.Exhaust brake

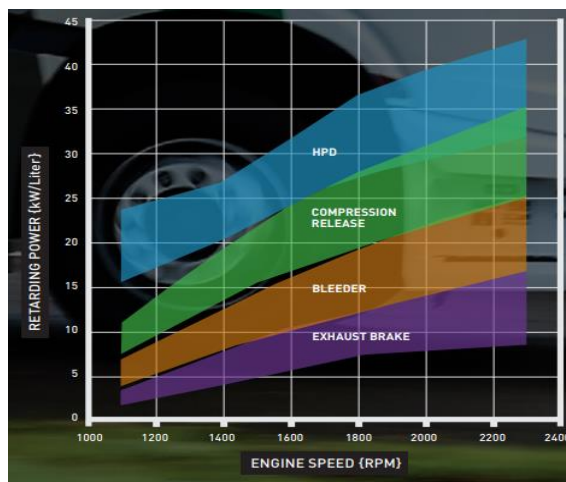


Figure 1.5.Engine brake performance ranges from various engine tests and simulation results [15]

Comparing to engine brakes, it has lower brake power. An example brake system is shown in Figure 1.4. As seen, there is a valve in the exhaust manifold to adjust the braking pressure.

According to brake data taken from product website, in Figure 1.5, output brake torque of engine brake types are shown. The figure demonstrates engine brake performance ranges from various engine tests and simulation results [15-17].

### 1.1.3. Hydro-mechanic retarders

Hydro-mechanical retarders are widely used in trucks. The retarders consist of seal,

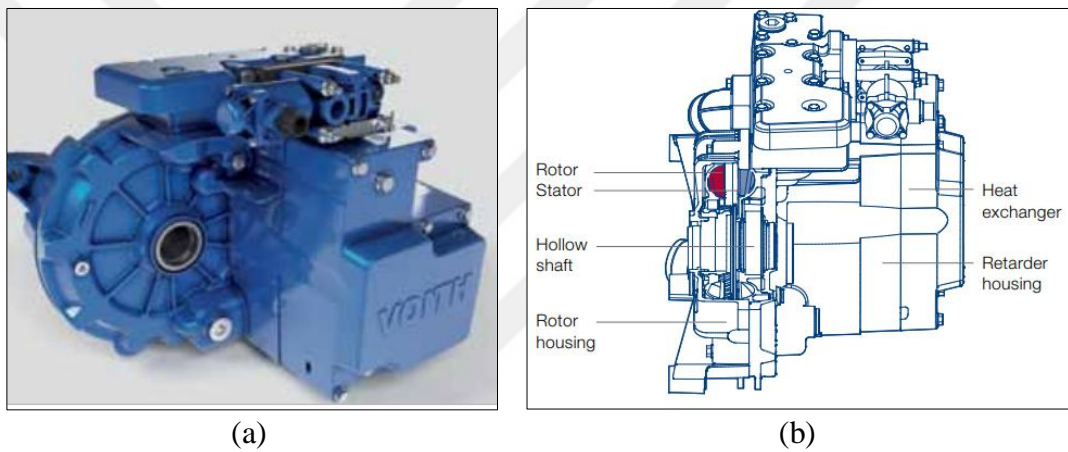


Figure 1.6.(a) Voith Retarder VR 123 [32] (b) Cross section view

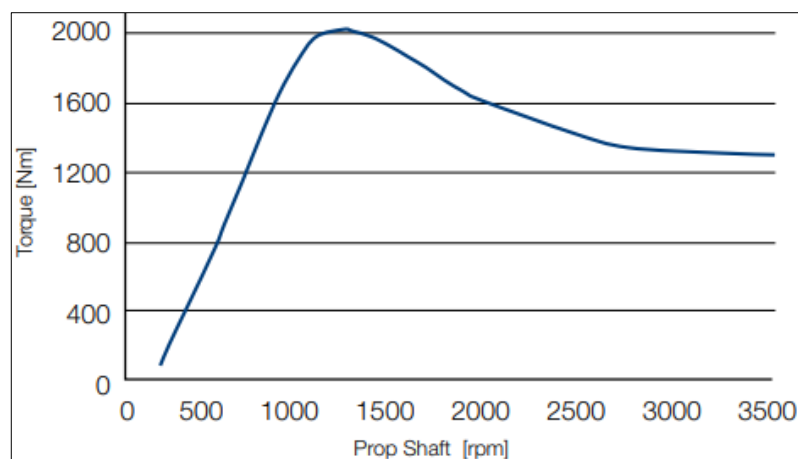


Figure 1.7.Brake torque vs speed curve of VR 123 retarder

rotor, stator and oil tank. When brake signal received, oil in tank transfer between rotor and stator. Then rotating oil creates brake torque by crashing to stator. [18] This kinetic energy transforms into heat. To increase performance, the brakes needs gearbox integrated with transmission output.

As seen in Figure 1.6 (a) hydro-mechanical retarder of Voith Company is seen. In Figure 1.6 (b) red colored part belongs to rotor and blue colored part belongs to stator [19]. In Figure 1.7 brake torque vs speed characteristic of VR 123+ hydro-mechanic retarder is shown.

#### 1.1.4. Low voltage eddy current brakes

Eddy current brake supplied from low voltage battery is used in trucks. The brakes are quiet, frictionless and fast response systems. However, they have high current needs and low power densities. Due to this, they are not commonly preferred in trucks. In next part, as a general eddy current review, there will be more detailed eddy current literature survey.

In Figure 1.8 (a), low voltage retarder of Telma Company seen [20]. It is an axial flux, eight poles electrically excited eddy current brake. On rotor, there are fan blades to cool down the brake. In the curve 1,2,3,4 are operation modes, for each curve while number of excited winding increases, total brake torque is increased proportionally as shown in Figure 1.8 (b).

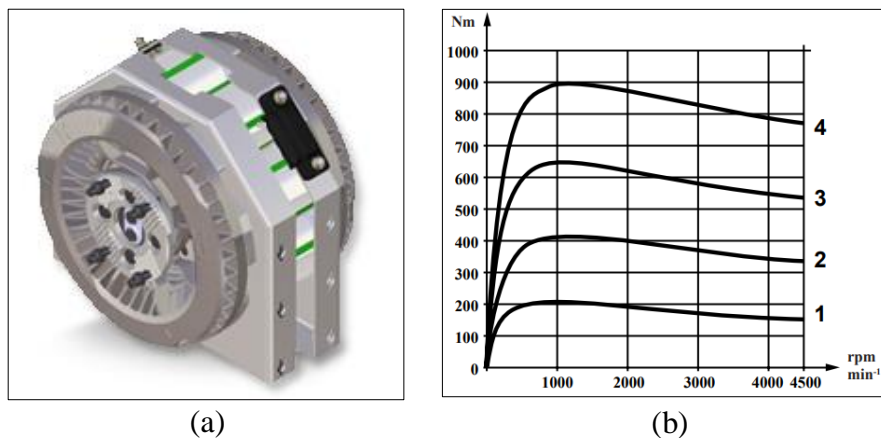


Figure 1.8.(a)AD 50 90 eddy current retarder (b)torque vs speed curve

## **1.2. New Generation Truck Retarders**

In prior section, conventional retarders mentioned are also divided into two groups. These are input and output retarders. Input retarders are Jake brake and back pressure brake which is directly related to engine work. Due to this direct relation, the retarder systems cannot be used in new generation fully electric trucks. Output retarder is hydro-mechanic retarders and low voltage supplied eddy current retarders. Due to that conventional hydro-mechanical retarders are designed to work integrated with transmission and brake oil reservoir requirements; the retarders are going to disappear in new generation trucks. The other retarder which is supplied from low voltage and drains too much current, for instance AD 50 90 drains 160 A for full brake, is not preferable when 600-750-volt battery system is available. In this condition, regenerative brake is a good alternative for truck retarder. As mentioned before the regen system cannot be used without a sub system for full charge battery condition. The regenerative brake must operate with sub system such as discharge resistor module or super-capacitor or eddy current brake.

### **1.2.1. Regenerative brake integrated with super-capacitor module**

Feng (2012) studied on regenerative braking system integrated with supercapacitor and braking resistor for rail vehicle. Design process and control method is represented. In proposed system is shown in Figure 1.9 and in Figure 1.10. During brake process, if battery voltage is low, system works as a conventional regenerative brake system. T1, T2 and Trz are in off state and battery is being charged. If battery in high state and super capacitor is in low state, brake converter behaves as a step-down converter and charge the capacitor T2, TRZ closed and T1 working with PWM to adjust bus voltage of supercapacitor. If battery and super capacitor is in high state, only resistance brake is performed and TRZ works in PWM mode. The advantage of the system is that with super capacitor usage, system power density increases compared to system having only battery. The disadvantages of the system is that it requires brake converter, the system has to be integrated with discharge resistor incase whole system has high state of charge. In addition, supercapacitor modules are as expensive as lithium ion batteries.

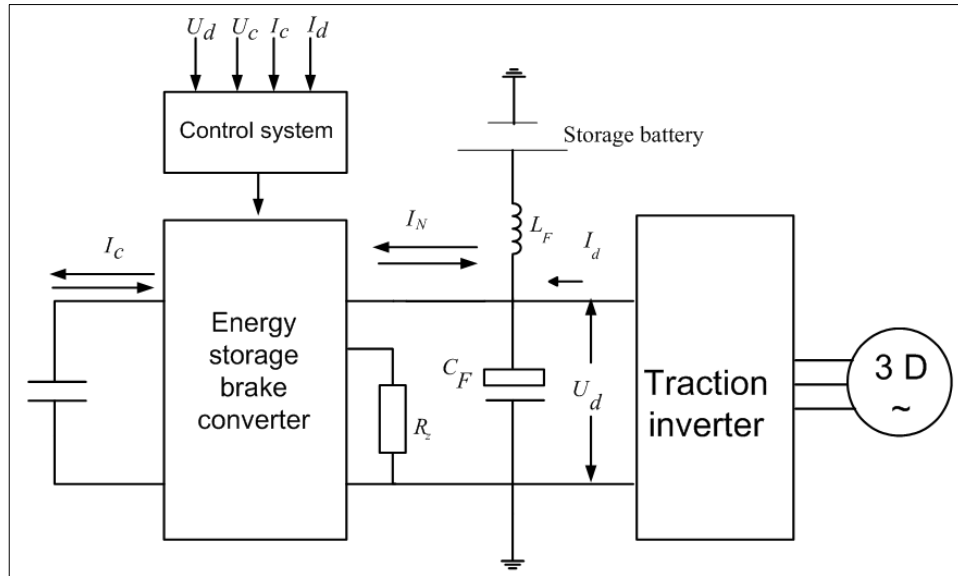


Figure 1.9. Brake system [21]

In 2014 Li-qiang investigates regenerative brake system integrated with super capacitor for electric vehicle by using Simulink and AVL CRUISE software [22]. It is said that during regenerative brake, battery has charging limitation due to power constraints and using super-capacitor increases this limit. Up to %88 regeneration is

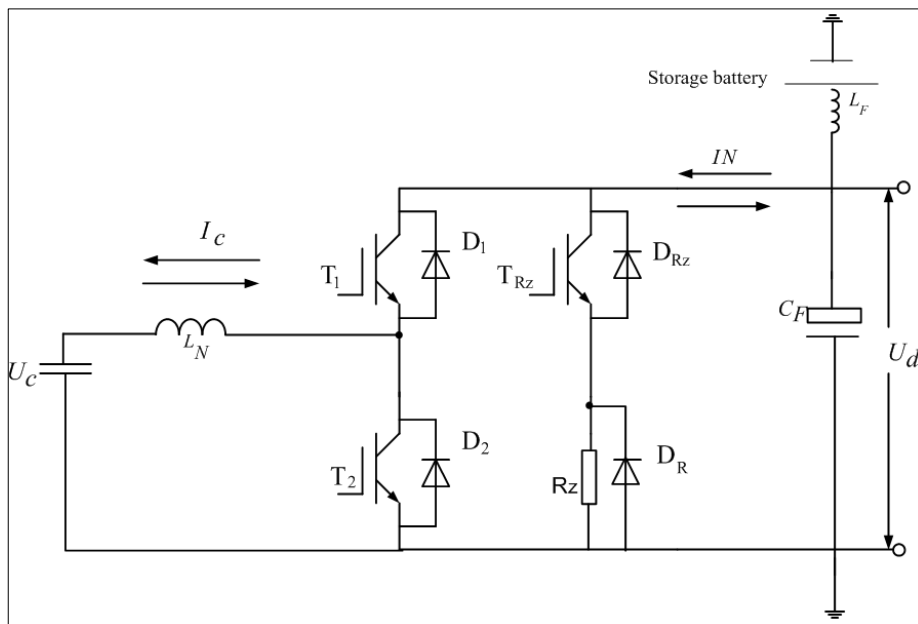


Figure 1.10. Brake convertor [21]

declared. However, there is no solution in case of high state of charge condition for battery and super-capacitor.

In 2016 Naseri proposes supercapacitor and battery mix electrical storage system to have both high power and high energy density [23]. Battery performance and supercapacitor performance are compared according to the parameters which are energy density, power density, temperature range and price. Also power electronic converter types which is integrated with battery and supercapacitor is compared. Regenerative limit due to high SOC is emphasized.

### 1.2.2. Regenerative brake integrated with resistor module

Garcia (2010) analyzed metro tramway system in Spain by using MATLAB-Simulink based on real road data. As shown in Figure 1.11, the system consists of four traction motors which is driven by inverter. To gain regenerative brake power, there is a battery. There is a chopper resistor in case battery has high SOC. The system is mainly powered by fuel cell. To adjust voltage level, there are two converters [24].

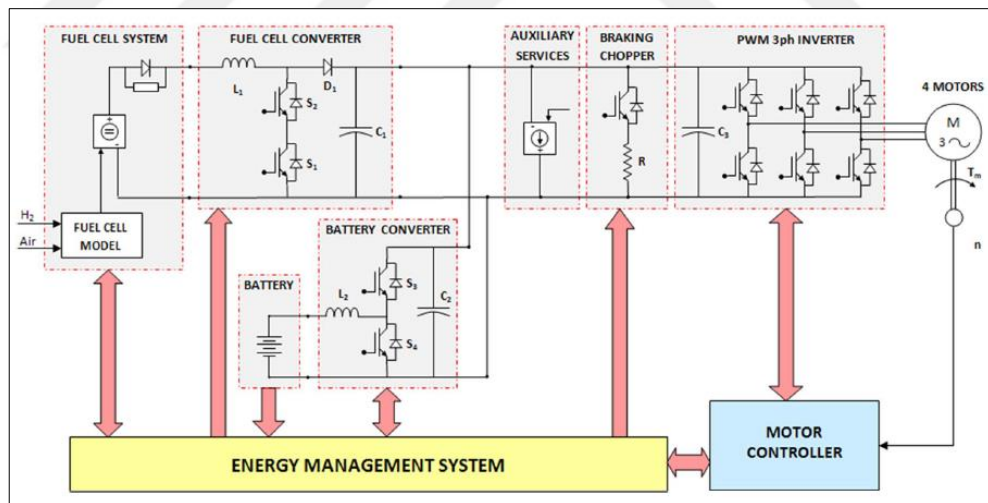


Figure 1.11. Configuration of the FC-battery-powered hybrid system for the tramway [37]

STW Technic has a brake chopper system for automotive [25]. As seen in Figure 1.12 (a), there are two high voltage cable colored orange. There are two cooling port colored yellow for transformer oil input. There is one signal low voltage connector between



the cables and the cooling port. As seen in Figure 1.12 (b), there is a power electronic circuit consist of three phase brake chopper to adjust power delivered to star connected three power resistor. The module usage is similar to usage in Figure 1.. The module is parallel connected to inverter and battery bus. These three systems communicate to each other via CAN network. The advantage of the system is that breaking has not any SOC limitation with proper thermal cooling. Also, compact design makes packaging easy in vehicle yet the oil cooling system is not common in vehicle. Due to this, it requires second cooling system addition to water/glycol cooling system.

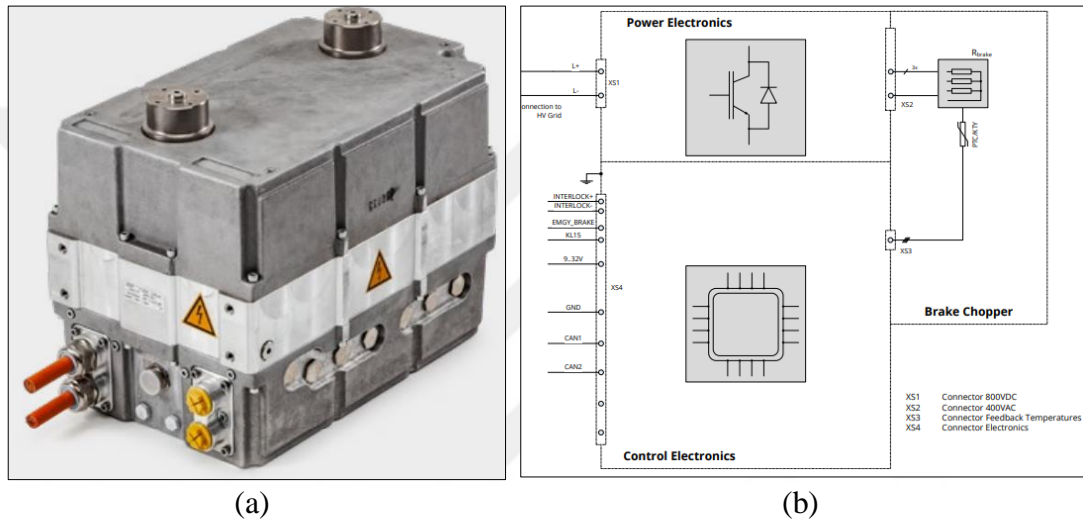


Figure 1.12. PowerMela Break Chopper: (a) Module (b) Diagram

### 1.2.3. Regenerative brake integrated with eddy current brake

In this thesis, instead of discharge resistor module or super capacitor, eddy current brake usage, supplied by high voltage, is proposed shown in Figure 1.13. Similar to mentioned system, ECB, high voltage battery and inverter are connected parallel via contactor. The ECB system is in use while the battery cannot be used for charging. Before analyzing the proposed system, ECB literature must be reviewed. ECBs are classified into three class via their movement type, flux direction and excitation method as shown in Figure 1.14.

In 1942, Smythe derives mathematical expressions by using Maxwell equations and ohm law to obtain numeric equations of induced eddy current on thin rotating disc [26]. Due to disc thickness is low, skin effect is neglected. Circular permanent

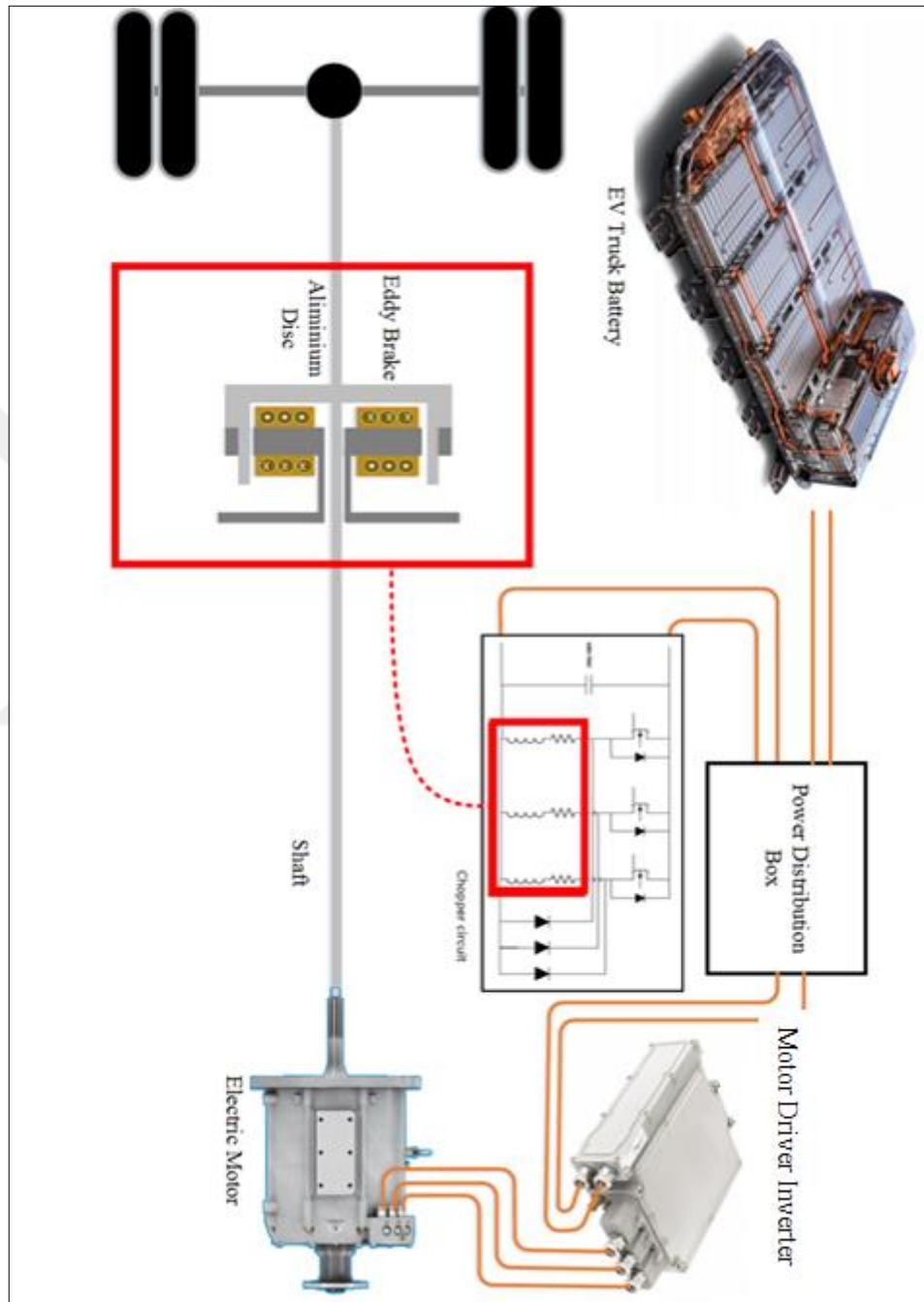


Figure 1.13. Proposed ECB usage for electrical vehicles

magnets provide axial flux passing through the thin disc. He also explains temperature effect on disc resistivity and then effect on brake torque. Field reduction due to generated eddy current is referred.

In 1977, Singh analyzed eddy current brake having two-sided stator with electrical excitation and having one rotor which is conductive disc [27]. For thick and thin disc, analytical expressions are derived on proposed geometry. Skin effect is being regarded for each disc. According to Singh findings, for a thin plate, at high speed region, torque is inversely proportional to speed. For a thick plate, torque is inversely proportional to square root of speed.

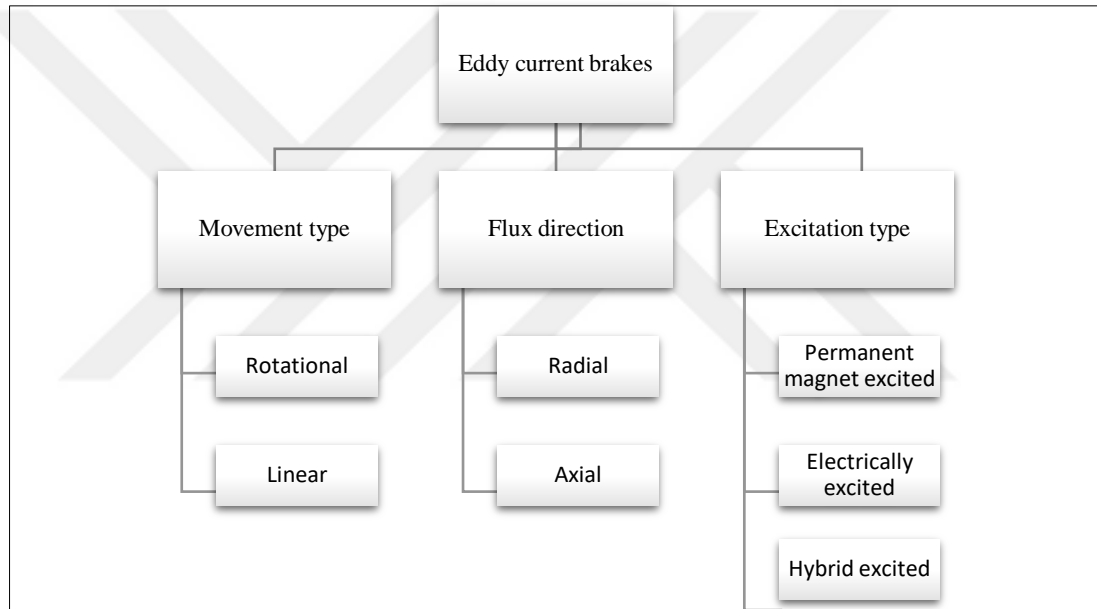


Figure 1.14. Classification of eddy current brake

In 2000, Hong studies on linear, electrically excited ECB for railway application [28]. The proposed system is not required external power source due to it uses regenerative power during brake. By small scaled prototype test, a 2D FEA analysis is verified. By PI controller constant torque control is proposed. However, thermal effects are not mentioned in the work.

In 2004, Anwar proposes two stages torque functions which depend on excitation currents and rotor radial speed [29]. By using experimental data and utilizing

MATLAB polyfit function, coefficients of the functions are defined. The torque functions with estimated parameter matches with real vehicle test data.

In 2011, Liu investigates two rotor, axial flux, and electrically excited eddy current brake [30]. Based on numeric equation torque characteristic is studied. In 0 to 1200 rpm range torque speed data is collected by test setup. Thermal effect on brake torque is investigated.

In 2012, Sharif validates analytical calculations by experimental test for radial flux permanent magnet excited ECB [31]. Skin effect and armature reaction are analyzed. It is claimed that airgap distance and magnetic flux density has no effect on critical speed unlike electrical resistivity. Factors effecting maximum torque is obtained. To validate mathematical calculation, different rotors are tested. Results are compared.

In 2016, Wang derives analytical model for axial flux, quasi-halbach permanent magnet for 2D geometry [32]. He also uses two correction coefficients to correlate from 2D to 3D. 3D FEA results and 3D correlated analytical results are compared. It is also resulted that quasi-halbach permanent magnet structure provides thinner back-iron, yet back iron should not be replaced with non-ferromagnetic material.

In 2016, Gulec investigates axial flux electrically excited eight poles ECB by using magnetic equivalent circuit of proposed ECB [33]. Influence of resistivity and permeability of the disc material on output torque is also obtained. According to obtained results, required disc properties are defined. Magnetic equivalent circuit approach is validated by 3D FEA analysis and prepared test setup. Brake power is determined by power dissipation function depends on disc conductivity, skin depth, radial speed and airgap flux density. In design process, a stator tooth to pole ratio is optimized. Airgap distance is determined by needed brake torque. In results, for 3A, 5A and 7A excitation currents, Magnetic equivalent circuit calculations, FEA simulation results and experimental results are compared. It is claimed that difference of the results is based on resistance change of the disc via thermal change.

In the same year, Gulec also proposes novel axial flux hybrid excited ECB [34]. The excitation is provided by permanent magnets and the way of magnetic flux is directed

by electrical excitation. The proposed ECB and conventional ECBs are compared by magnetic equivalent circuit calculations, FEA simulations and experimental results. It is concluded that results are similar and accurate. Proposed ECB has %35 more torque and %60 faster response time than conventional ECBs.

In 2017, Cho studies on axial type eddy current brake which has rotor consisting of two layers [35]. First layer non-laminated iron and second layer is 0.15 mm copper coating. Armature reaction, skin effect is investigated analytically and experimentally. FEA simulation is also performed. To calculate armature reaction analytically, Reynolds number is exploited. Effect of coating thickness on brake torque is investigated.

In 2018, Tarvildilu investigates axial flux ten poles electrically excited ECB by analytical calculations, FEA simulations and experimental results for aviation application [36]. The ECB has two-sided stator with permanent magnets and one side copper rotor. The three results are compared. At higher speed due to high thermal effect FEA simulations and experimental results have higher difference. To have a required power density and to reduce volume and weight, genetic algorithm performed. Magnet to pole pitch ratio, magnet height, magnet length, copper thickness and number of poles are optimized with genetic algorithm. To perform the optimization, MATLAB and Ansys Maxwell tools are coupled.

In 2018, Jin's proposed model is linear, hybrid excited ECB with two layer stator [37]. Analytical and FEM torque results are graphically compared. Eddy current losses for thin conductive layer, back iron and excitation losses are calculated as a heat source for thermal analysis. Thermal conduction and convection is taken into consideration. CFD analysis is performed. 2D thermal lumped parameter is verified by experiment. As a result, thermal findings are used to correct output torque calculations.

### **1.3. Thesis Objective**

The new regulations, new legislations and increased DC charge stations are the signs of future vehicle trends. In future, vehicles will be fully electrified. Also, commercial trucks and other heavy-duty vehicles will be fully electrified. With this change, for

heavy duty vehicles will not provide brake regulation and safety standards fully because regenerative brake is not able to operate as a secondary brake at high state of charge condition. The first goal of the thesis is to cover this open point. Therefore, new generation trucks will be safer for both drivers and pedestrian. The second goal is to propose new usage method of eddy current brake on fully electrified heavy-duty vehicles. The Third goal is to design ECB having optimum brake torque/volume ratio. With this aim, there will be affordable, efficient safety module for future generation heavy duty vehicles.

#### **1.4. Thesis Method**

In this thesis work, these steps are followed:

- 1- By using web data; a heavy-duty truck and a suitable powertrain module will be selected. According to ECE R13 regulation and selections, requirements of ECB will be defined.
- 2- Theory of related topics related to the ECB and modelling of proposed geometry will be investigated.
- 3- Regarding to cost, efficiency, manufacturability; materials will be selected, or options will be determined.
- 4- With selected materials, to reach optimum brake-torque/volume, geometric variations will be investigated by using FE analysis and analytical calculations.
- 5- Final Design parameters will be listed. The results will be clarified.
- 6- Possible future works will be explained.

#### **1.5. Requirements for the Proposed Eddy Current Brake**

##### **1.5.1. Nominal torque and speed values**

For the analysis, truck weights are defined as 18000 kg. Volvo FMX series D11K460 truck is selected as a model [38]. Maximum speed value at its cluster is 130 km/h equal to 36 m/s. According to the power range and speed range of the truck, e-motor SUMO HD HV3500-9P is suitable [39]. Tire radius is 532mm. According to parameters, single speed transmission ratio can be calculated by equations below:

In Equation (1.1) and (1.2),  $v_{wh}$  represents the speed of wheel.  $R_T$  is radius of wheel.  $v_{ve}$  is the vehicle speed.  $sh_r$  represents single speed transmission ratio.  $v_{mm}$  is the maximum speed of the selected e-motor which is equal to  $3400 \text{ min}^{-1}$ .

$$v_{wh} = \frac{30v_{ve}}{R_t\pi} \quad (1.1)$$

$$sh_r = \frac{v_{mm}}{v_{wh}} \quad (1.2)$$

In normal road grade is maximum %6 equal to  $3.5^\circ$  slope [40]. The forces acting on the truck is shown in the Figure 1.15. In Equation (1.3),  $M_t$  is the gross weight of the truck.  $g$  represents gravitational constant.  $\alpha$  is slop angle.  $F_{pr}$  represents force parallel to road.

$$F_{pr} = M_t g \sin(\alpha) \quad (1.3)$$

In Equation (1.4) and (1.5),  $F_{air}$  is air drag force.  $\rho_{air}$  is air density.  $C_d$  is drag coefficient.  $C_r$  is coefficient of rolling resistance.  $A_v$  is front area of the truck.

$$F_{air} = 0.5\rho_{air}C_dA_vv_{ve}^2 \quad (1.4)$$

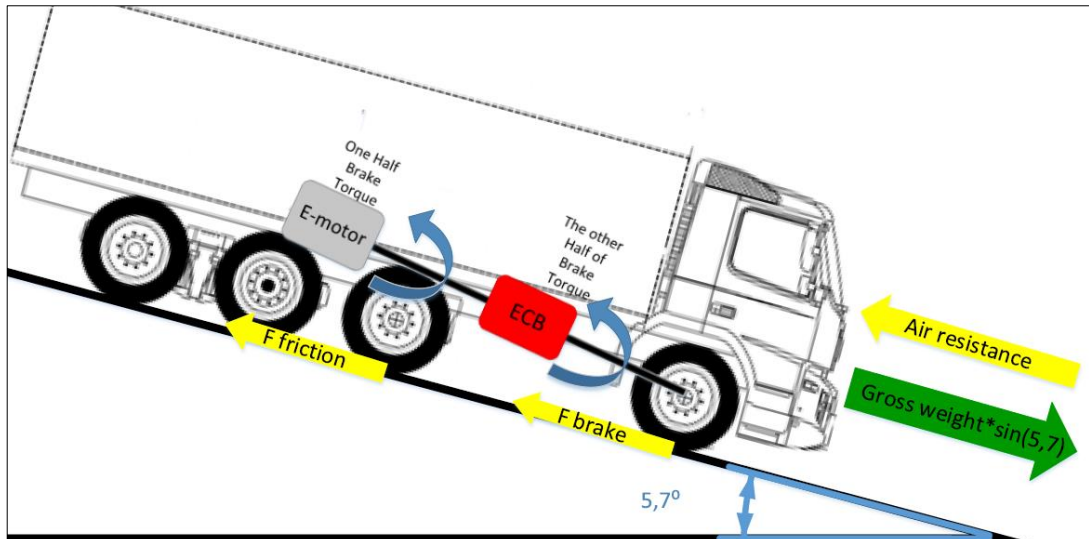


Figure 1.15. At maximum slope angle, the forces effecting on the truck

$$F_{fr} = M_t g c_r \cos(\alpha) \quad (1.5)$$

In Equation (1.6), (1.7) and (1.8)  $T_{wh}$  represents torque at wheel.  $T_{br}$  is needed brake torque on shaft of truck.  $F_{net}$  represents net force on truck.

$$F_{net} = F_{pr} - F_{air} - F_{fr} \quad (1.6)$$

$$T_{wh} = F_{net} R_t \quad (1.7)$$

$$T_{br} = \frac{T_{wh}}{sh_r} \quad (1.8)$$

According to parameters shown in Table 1.1, proposed ECB should be designed for 900 Nm and  $644 \text{ min}^{-1}$  on shaft.

Table 1.1. Numerical value for brake requirement calculations

$M_t$ (kg)	18000	$F_{air}$ (N)	139.5
$g$ (m/s <sup>2</sup> )	9.8	$F_{fr}$ (N)	1232
$v_{ve}$ (m/s)	36	$F_{net}$	9396
$R_t$ (meter)	0.522	$\rho_{air}$ (kg/m <sup>3</sup> )	1.225
$v_{mm}$ (min <sup>-1</sup> )	3400	$A_v$ (m <sup>2</sup> )	7.75
$v_{wh}$ (min <sup>-1</sup> )	658	$c_r$	0.007
$sh_r$	5.24	$c_d$	0.6
$F_{pr}$ (N)	10768	$\alpha$ (degree)	3.5
$T_{wh}$ (Nm)	4904	$T_{br}$ (Nm)	939



### 1.5.2. Nominal electrical parameters as an input

In Equation (1.9),  $w_{sh}$  represents radial speed of truck shaft.  $v_{sh}$  represents speed in rpm.  $\mu_{eff}$  is total efficiency of inverter and e-motor during regenerative brake.  $P_{iECB}$  is the available power input for proposed ECB.

$$P_{iECB} = w_{sh} T_{br} \mu_{eff} \quad (1.9)$$

Table 1.2. Numerical results of brake requirement

$w_{sh}$ (rad/s)	69.5	$\mu_{eff}$	0.9
$v_{sh}$ (min-1)	664	$P_{iECB}$ (W)	56322
$T_{br}$ (Nm)	900		

### 1.5.3. Dimensions

According to the reference values taken from [41]:

For mechanical concerns, tangential stress should be in 12000 Pa to 33000 Pa.  $l$  is the stator length. In Equation (1.10) and (1.11),  $D$  is diameter of stator.  $\chi$  must be selected in the range between 2 and 0.4.

$$\chi = \frac{1}{D} \quad (1.10)$$

$$T_{br} = \sigma_{Ftan} 4\pi r_i^3 \chi \quad (1.11)$$

If radius is selected small due to Equation (2.10) and  $v = wr$ , generated eddy current decreases and then armature effect decreases. Critical speed increases. Due to that  $\chi$  is selected near the upper limit in the range. Due to Equation (2.21), low  $r_i$  and high  $l$  results lower thermal resistance and better cooling performance.

Table 1.3. Numerical value used in the volume calculations

$\sigma_{Ftan}$ (Pa)	30000	$\chi$	1.5
$r_i$ (meter)	0.116	$l$ (meter)	0.35

## 2. THEORY AND MODELLING OF PROPOSED GEOMETRY

The proposed geometry is shown in Figure 2.1. In the figure single speed transmission, vehicle chassis and ball bearings between stator and rotating axle and e-motor are not shown. There is rotating truck axle which is connected to both single speed transmission and e-motor. The axle transmits e-motor torque to single speed transmission. Fan blade, rotor of ECB and heat sink are connected to Rotating axle. Fan rotates by the same speed with axle. It creates air flow through heat sink. So, Convection resistance of the heat sink decreases.

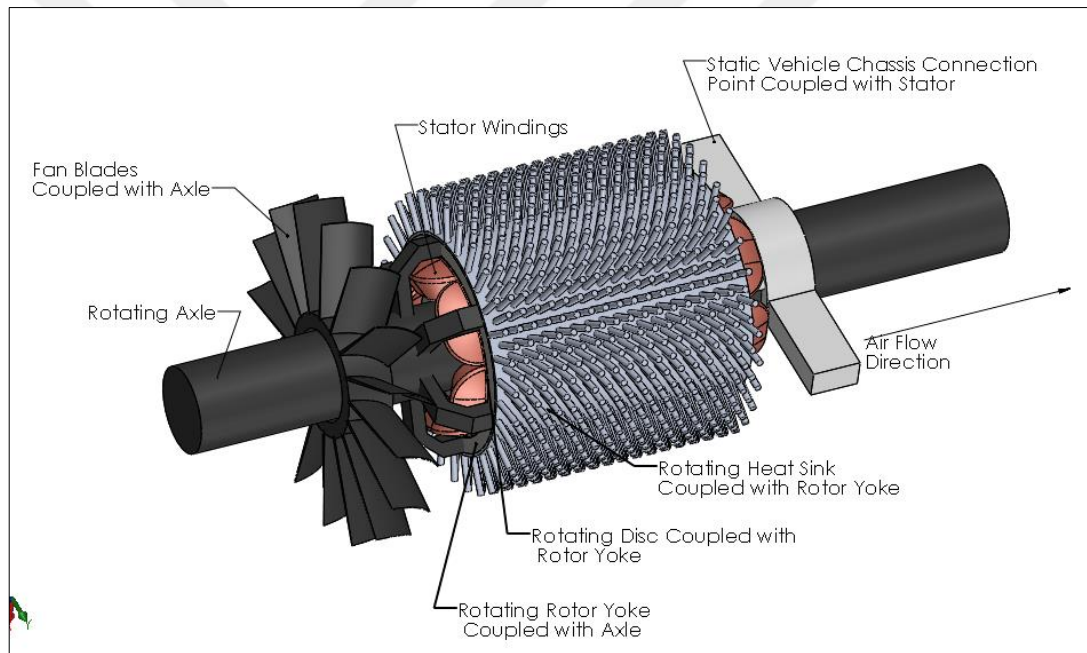


Figure 2.1. Proposed eddy current brake system integrated on vehicle axle

Inside rotating rotor, there is stator core which does not move. It is connected vehicle chassis via connection point. Due to rotor and stator windings, stator core is not seen in the figure. Ball bearings which is not seen in the figure, separates rotating axle and static stator. Air flow direction which is passing through heat sink pin, is also seen.

## 2.1. Magnetic Analysis by Magnetic Equivalent Circuit for Proposed Structure

In Figure 2.2, cross-section of the proposed system and flux lines is shown. Heat sink, fan blades are not shown. Rotating rotor part consists of steel 1010 laminated electrical steel and thin aluminum alloy disc. Laminated Steel 1010 is used as a rotor yoke. Lamination significantly eliminates eddy currents in rotor yoke. The function of it is to complete magnetic circuit. The thin disc is the conductive region where eddy current is generated. Stator also consists of laminated steel 1010. Function of windings is to create magneto motive force. They are excited by DC current. Due to thermal considerations current density is selected as  $5\text{A}/\text{mm}^2$ .

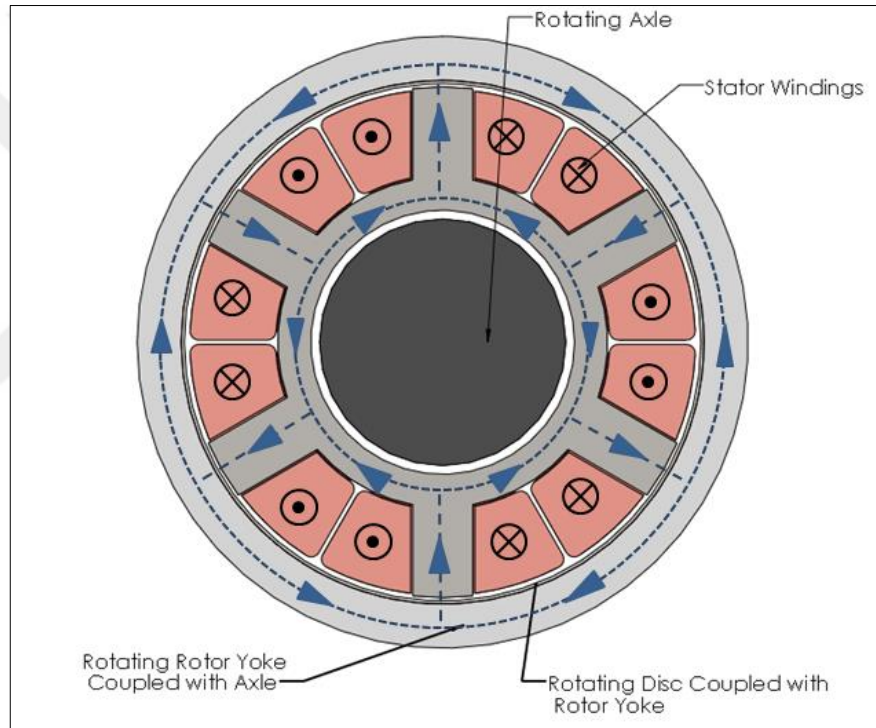


Figure 2.2. Cross section of proposed ECB

In Figure 2.3, equivalent magnetic circuit of proposed geometry is shown.  $N$  is the number of turns per pole.  $i$  is current per coil. In Equation (2.1),  $R_{yr}$  and  $R_{ys}$  are magnetic resistances of rotor yoke and stator yoke.  $R_{disc}$  and  $R_g$  are magnetic resistances of aluminum and airgap.  $R_{tooth}$  is magnetic resistance of stator tooth. Generated eddy currents are also shown in the Figure 2.3. The generated eddy current

exponentially increases until pole edge. After that it decreases more rapidly and exponentially.

$$N_i = (0.25R_{yr} + R_{disc} + R_g + R_{tooth} + 0.25R_{ys})\phi \quad (2.1)$$

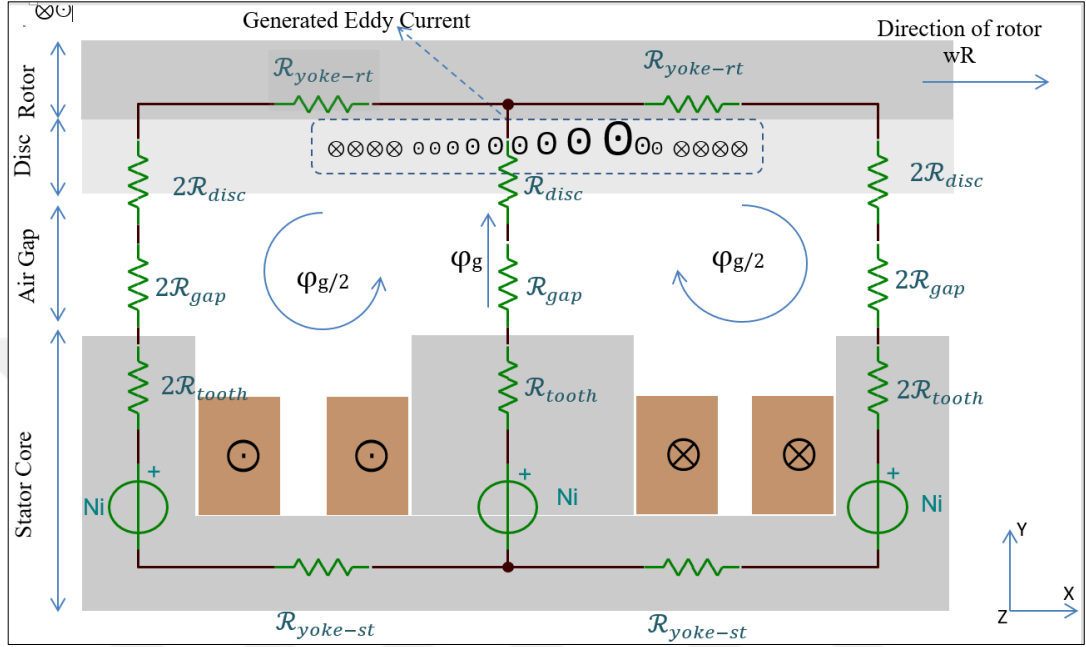


Figure 2.3. Linear projection of proposed geometry and flux lines

In Equation (2.2),  $B_g$  and  $B_{al}$  are magnetic flux densities on airgap and aluminum disc.  $\phi$  is magnetic flux passing through stator tooth. Equation (2.1) and (2.2) are used to find flux density on aluminum disc at static condition.  $B_g$  and  $B_{disc}$  are nearly equal if disc material is selected as non-magnetic.

$$B_g \cong B_{disc} = \frac{\phi}{A_g} \quad (2.2)$$

Equation (2.3) represents common reluctance formula.  $l$  is length of the reluctance.  $A$  is area.  $\mu_0$  is permeability of vacuum and  $\mu_r$  is relative permeability of the material.

$$R = \frac{l}{\mu_0 \mu_r A} \quad (2.3)$$

In Equation (2.4) and (2.5),  $N_i$  is total ampere-turn of one pole. Due to constant current density,  $N_i$  is proportional to winding area.  $R_{st-out}$  and  $R_{st-in}$  are out radius and inner

radius of the stator.  $p$  is pole number.  $\tau$  is pole pitch ratio.  $A_w$  is the winding area of one coil per pole.  $J$  is current density.

$$A_w = \frac{(R_{st-out}^2 - R_{st-in}^2)\pi}{2p} - (R_{st-out} - R_{st-in}) \frac{2\pi R_{st-out}\tau}{2p} \quad (2.4)$$

$$A_w J = Ni \quad (2.5)$$

At dynamic condition, created eddy current opposes the magnetic flux. This is called armature reaction. It will be discussed in the ECB Theory part.

## 2.2. Eddy Current Brake Theory and Modelling for Proposed Structure

In Equation (2.6), eddy current is generated on a conductive disc according to Maxwell Equations. Line integral of electric potential is equal to flux change rate by time on area.

$$\oint \vec{E} \cdot d\vec{l} = - \frac{\partial \vec{B}}{\partial t} \cdot d\vec{A} \quad (2.6)$$

For proposed geometry, magnetic flux density vector has only  $B_y$  vector and it is assumed that along  $z$  axis and  $y$  axis flux density does not change, according to this, the Equation (2.7) is derived:

$$\vec{E} \cdot d\vec{z} = - \frac{\partial B_y}{\partial x} \frac{dx}{dt} d\vec{z} d\vec{x} \quad (2.7)$$

$\frac{dx}{dt}$  is  $v$  the linear velocity of the rotor, equation becomes to Equation (2.8):

$$\vec{E}_z = -B_y v \quad (2.8)$$

In Equation (2.9), ratio of electrical potential to resistivity according to Ohm's law gives current density.

$$\vec{J} = \frac{\vec{E}}{\rho} \quad (2.9)$$

By Equation (2.8) and ohm law, Equation (2.10) is derived. In Equation (2.10) and (2.11),  $\rho$  is the resistivity of conductive region.  $t$  is conductive disc thickness.  $\delta$  is skin depth [33].

$$\vec{J}_z = -\frac{\vec{B}_y \times v}{\rho} e^{\frac{t}{\delta}} \quad (2.10)$$

$$\delta = \sqrt{\frac{2}{\mu_0 \mu_r \sigma \omega}} \quad (2.11)$$

In Equation (2.12), by using Lorenz Force Law on proposed ECB geometry, force per pole equation is derived.  $l$  length of the stator.  $p$  is number of pole. It is assumed that  $B_y$  is not changing along radial direction.

$$\vec{F} = \vec{l} \times \vec{B}_y \quad (2.12)$$

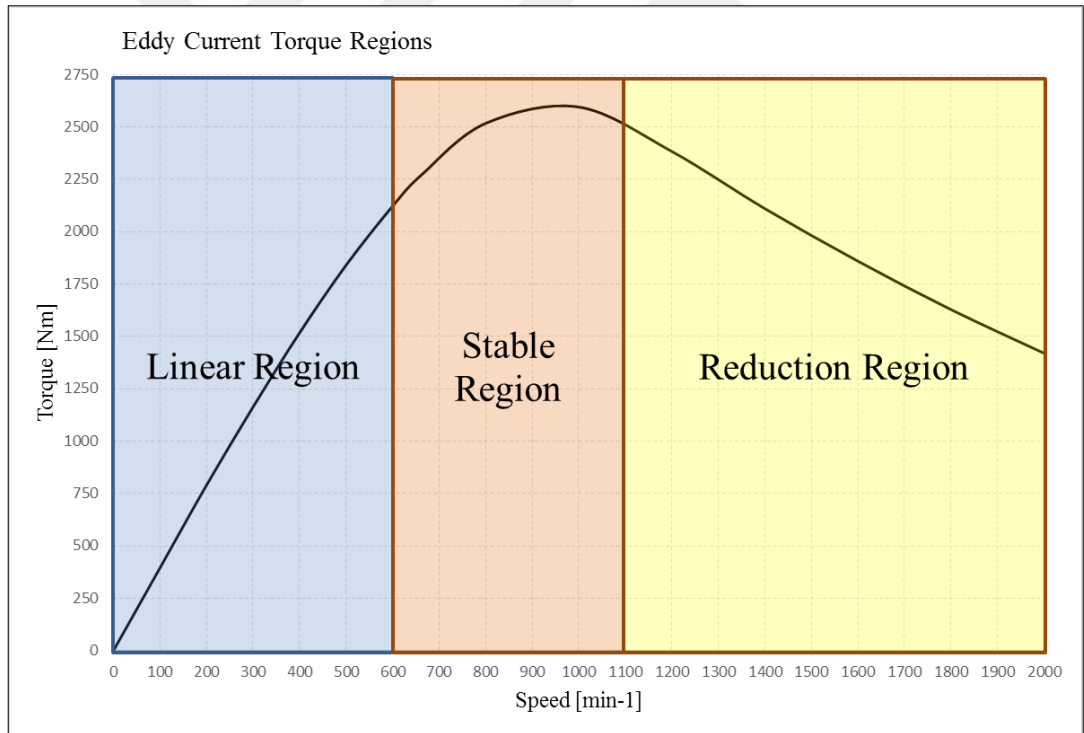


Figure 2.4. Eddy current brake regions

In Equation (2.13), integral of the Equation (2.12) along disc thickness and along one pole pitch gives Equation (2.13).

$$\vec{F} = l \int_0^{\frac{2\pi}{p}} \vec{B}_y \int_0^t \vec{J} \, dr d\theta \quad (2.13)$$

In Equation (2.14),  $T_b$  is total brake torque  $r_i$  is inner radius of the conductive disc. Due to disc is thin enough; inner radius change with disc thickness is ignored.

$$T_b = p \vec{F} r_i \quad (2.14)$$

The equations above are enough to calculate brake torque in linear region. However, beyond the region, armature reaction becomes a dominant parameter with increasing speed for ECB. Generated eddy current opposes the magnetic flux density at airgap.  $B_0$  and  $B_{net}$  difference becomes significant. Because of the phenomena, torque speed graph of eddy current can be analyzed in three regions as shown in Figure 2.4. First is linear speed region where armature reaction effect is less, and brake torque is proportional to rotor speed. Second is stable speed region where ECB reaches the maximum torque. Increase of brake torque is not linear at the region but brake torque increase with increase of the rotating disc. Third is reduction region where brake torque is decreasing with increase of speed. At this region generated eddy current dominantly makes magnetic flux density decrease in the disc, due to Equation (2.8) net magnetic flux,  $B_y$  decreases. To analytically investigate the brake torque in stable region and reduction region Reynolds number may be used [34,42,43,44]. In Equation (2.15),  $\mu$  is magnetic permeability.  $\sigma$  is conductivity.  $L_c$  is characteristic length.  $v_c$  is characteristic velocity.

$$R_m = \sigma \mu_0 L_c v_c \quad (2.15)$$

In Equation (2.16) and (2.17),  $A$  is flow area assumed as rectangle,  $P$  is perimeter of flow. Flow is generated eddy current. Flow area is equal to multiplication of the disc thickness and tooth length by neglecting fringing. Perimeter of the flow is equal to twice of the sum of tooth length and disc thickness.

$$L_c = \frac{4A}{P} \quad (2.16)$$

$$L_c = \frac{4\pi R t}{2\pi R t + p t} \quad (2.17)$$

In Equation (2.18),  $w$  is radial velocity and  $R$  is radius of the conductive disc.

$$v_c = wR \quad (2.18)$$

In Equation (2.19),  $B_{net}$  is average flux density on the conductive disc.  $B_0$  is the initial flux density at velocity zero.

$$B_{net} = B_0 e^{-R_m} \quad (2.19)$$

In Equation (2.20),  $K$  is a coefficient which corrects formula below. Calculation with Reynolds number provides average value of magnetic flux density in airgap but in the Equation (2.20), square of flux density is used. Rms value of magnetic flux density along one pole has to be used. In addition, that fringing effect in the airgap is ignored. To compensate the issues,  $K$  coefficient is determined. By comparing the simulation results,  $K$  is defined as 1.5 for analytical calculations.  $p$  is pole number.  $\tau$  is pole pitch ratio.  $t$  is disc thickness. By deriving equation above, total torque is derived:

$$T_b = KB_0^2 e^{-2\mu_0 \sigma \frac{4\pi R \tau t}{2\pi R \tau + p t}} wR^3 \sigma t 2\pi \tau l e^{\frac{t}{\delta}} \quad (2.20)$$

In Chapter 4, for each geometrical variation, total brake torque is analytically investigated.

### 2.3. Regenerative Brake on Electric Vehicle

To understand regenerative brake concept in electric vehicles, four operation quadrant of the electric motor has to be clarified. In Figure 2.5, four quadrants operation of motor is seen. In first quadrant, motor speed and torque is positive. In the quadrant motor drains power from battery and vehicles goes in forward direction. In second quadrant, while torque is positive, speed is negative. In the quadrant motor generates power and charge the battery and vehicles goes in reverse direction, proportional charging power, braking power is formed. In third quadrant, motor speed and torque is negative. In the quadrant, motor also consumes power from battery and vehicle goes in reverse direction. In Fourth quadrant, while torque is negative, speed is positive. In the quadrant motor also generates power and charges the battery and vehicles goes in



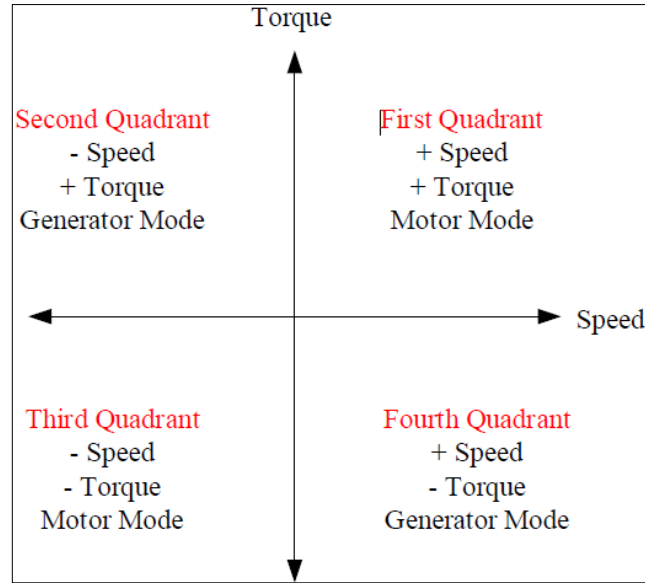


Figure 2.5. Four quadrant operation modes of electric motor

reverse direction and in reverse direction, proportional charging power, braking power is formed. The phenomenon can be explained by Equation (2.21):

$$T_{\text{motor}} - T_{\text{br}} = J \frac{dw}{dt} \quad (2.21)$$

As seen Equation (2.21), moment of inertia does not allow instant speed change, but motor torque can be changed instantly. Because of that when  $|T_{\text{motor}} > T_{\text{br}}|$ , vehicle is driven in motor mode forward or reverse direction. When  $|T_{\text{motor}} < T_{\text{br}}|$ , vehicle is driven in generator mode. The potential charging power is directly related with  $T_{\text{br}}$  and  $v_{\text{shaft}}$ . In electrical trucks, first and second quadrant operation is more important because most of the driving operation consists of driving forward and braking. Due to reverse speed is relatively low, braking charge power in second quadrant is not too much and negligible. In the thesis, first and second quadrant operation data is used.

#### 2.4. Half Bridge Controller and Control Method

IGBTs are used to control eddy current module and adjust current being drained from regenerative brake. To supply DC current to ECB winding, bulk capacitor is utilized, otherwise there forms time variable DC current which is drained from traction motor. The variable current may change the torque speed characteristic of proposed ECB. In

the Figure 2.6 (a), red arrow shows the current path. When IGBT is on state, current pass through eddy current coil represented with orange rectangle. In this region, current rises due to inductance. In Figure 2.6 (b), when IGBT turns off, inductance current discharges on the diode by decreasing. By adjusting the on and off times of the IGBTs, demanded average current is drained from the regen system. Demanded current is shown in Figure 2.7.

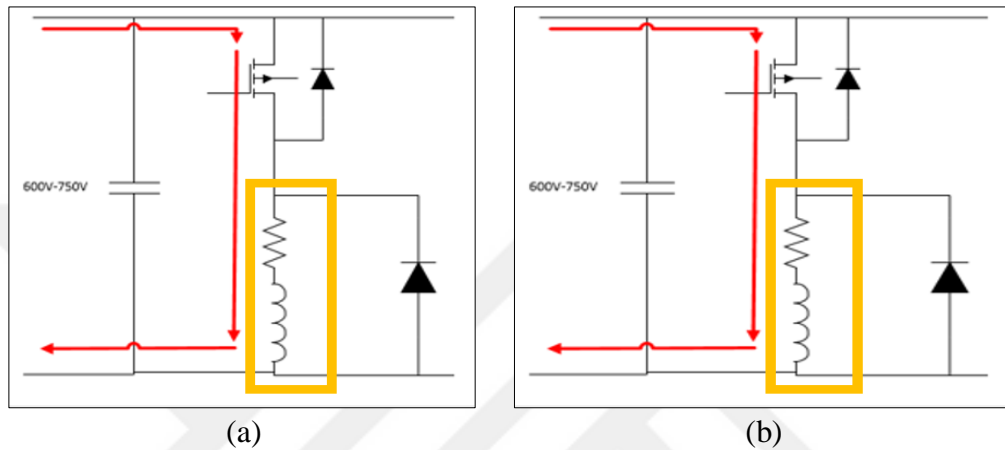


Figure 2.6. One phase eddy current and one leg chopper circuit IGBT (a) on and (b) off

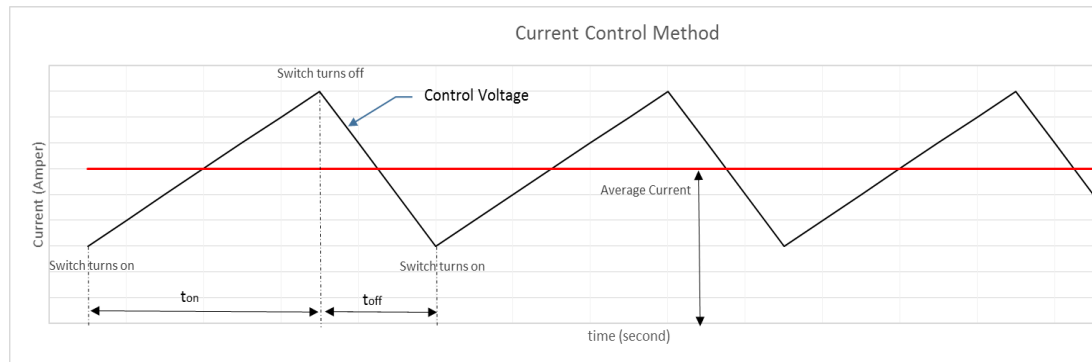


Figure 2.7. Constant current control

In the system frequency of the switching defines current ripple. The faster switching results the lesser current ripple while increasing switching loss. In Equation (2.21), (2.22) and (2.23),  $V_L$  is voltage applied on the terminal of bulk capacitor.  $L$  is inductance of one phase of the eddy current brake.  $i_L$  is current on windings.  $\Delta$  is total

change.  $t_{on}$  is the time the transistor stays on. If the R and Transistor  $V_{on}$  are neglected, current ripple is:

$$V_L = \frac{L di_L}{dt} \quad (2.21)$$

$$\Delta i_L = \frac{V_L}{L} t_{on} \quad (2.22)$$

$$i_{ripple} = 0.5 \Delta i_L \quad (2.23)$$

## 2.5. Thermal Lumped Parameter Model For The Proposed Geometry

Cross section view of proposed ECB is represented in the Figure 2.8. Fan blades, thin conductive disc, rotor yoke and heat sink are shown. They are rotating with same speed. The positions of the ball bearings separating the stator and the rotating axle are seen.

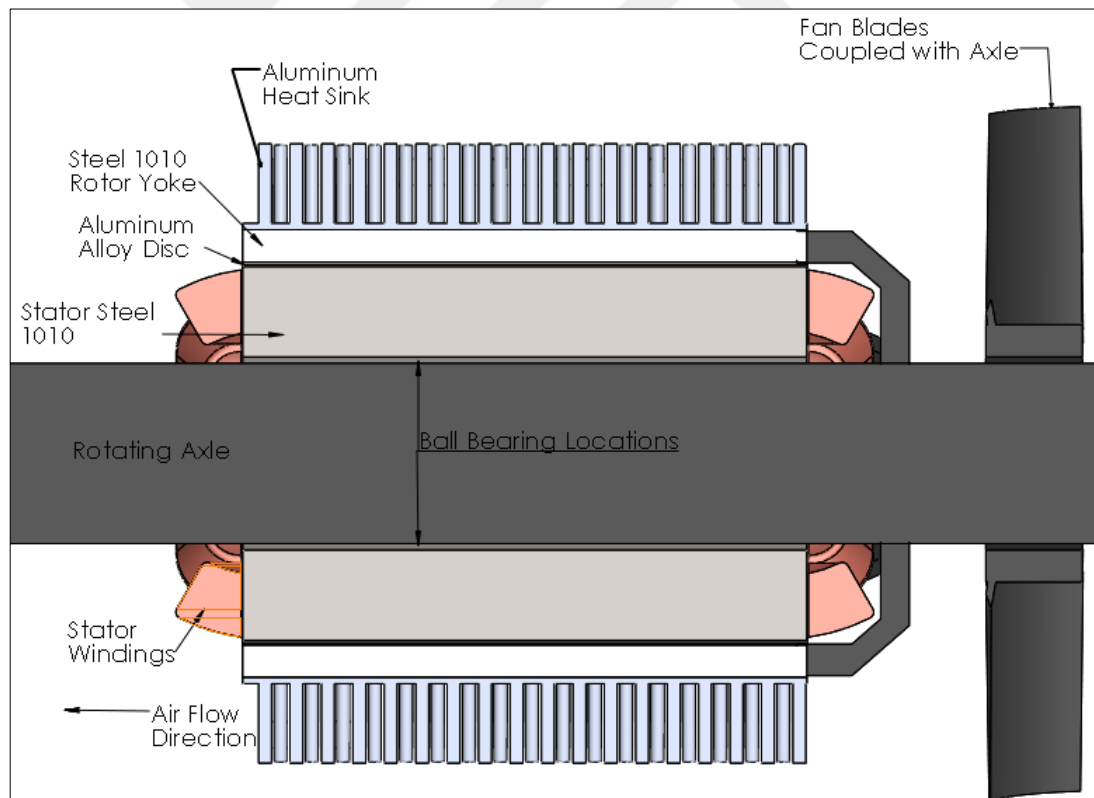


Figure 2.8. Cross section for thermal analysis

Importance of the thermal analysis for the thesis is that conductivity of the disc decreases by increasing disc temperature. This has direct effect on generated eddy current via Equation (2.9), Equation (2.15) and Equation (2.24).

$$R=R_{amb}(1+\alpha\Delta T) \quad (2.24)$$

$\alpha=0.004308$  for aluminum

To perform thermal calculation, 2D lumped model will be used. Heat transfer occurs by both conduction and convection. Due to rotor being designed laminated and isolation material between laminations, axial thermal conduction is neglected, and only radial conduction is calculated. Thermal radiation is also neglected due to small value. In Equation (2.25), Conduction heat transfer is seen in Figure 2.9 in medium  $k_1$  and  $k_2$ , [45].

$$Q_{cond}=-k_1A\frac{T_1-T_2}{L_1}=-\frac{T_1-T_2}{R_{th2}}=-k_2A\frac{T_2-T_3}{L_2}=-\frac{T_2-T_3}{R_{th3}} \quad (2.25)$$

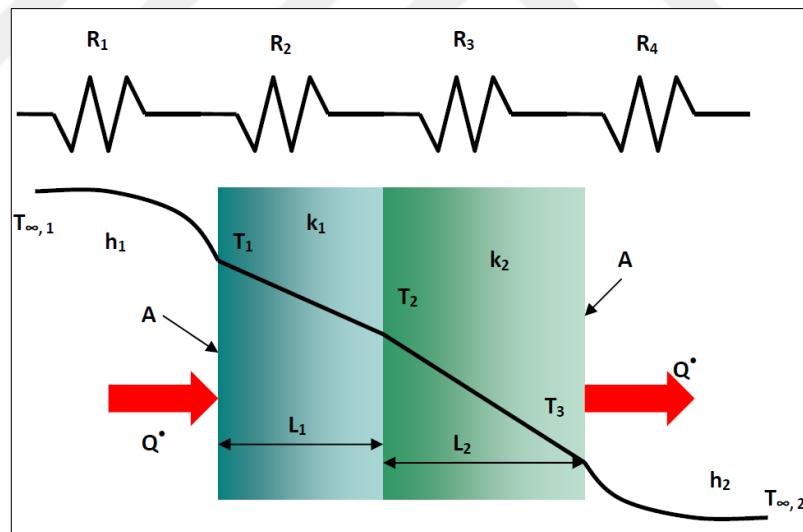


Figure 2.9. Heat transfer way [45]

In Equation (2.26), convection heat transfer is seen in Figure 2.9. in medium  $h_1$  and  $h_2$ .

$$Q_{conv}=-\frac{T_{\infty 1}-T_1}{h_1A}=-\frac{T_{\infty 1}-T_1}{R_{th1}}=-\frac{T_3-T_{\infty 2}}{h_2A}=-\frac{T_3-T_{\infty 2}}{R_{th4}} \quad (2.26)$$

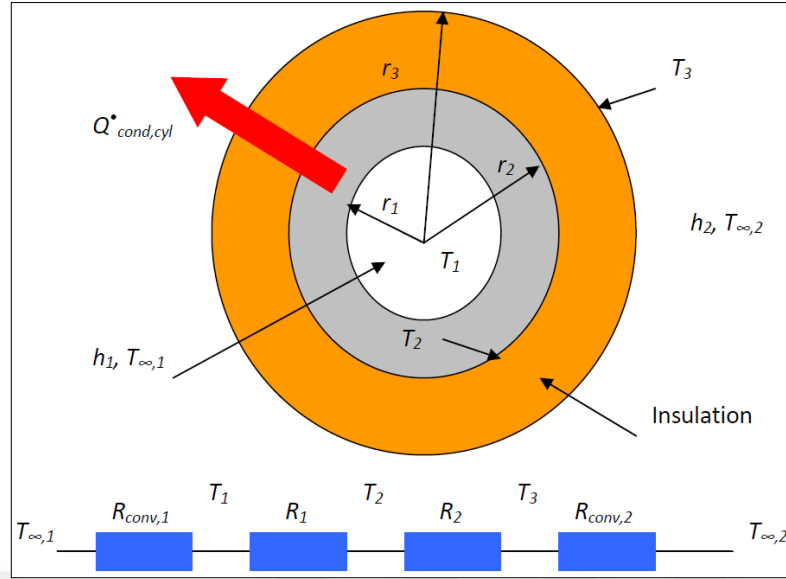


Figure 2.10. Heat transfer for cylindrical parts [45]

In Equation (2.27), for Cylindrical Conduction heat transfer is seen in Figure 2.10.

$$Q_{\text{cond}} = -k_1 2\pi L \frac{T_1 - T_2}{\ln(r_1/r_2)} = \frac{T_1 - T_2}{R_{\text{th}2}} = -k_1 2\pi L \frac{T_1 - T_2}{\ln(r_2/r_3)} = \frac{T_2 - T_3}{R_{\text{th}3}} \quad (2.27)$$

### 2.5.1. Thermal Model of ECB

Total heat generated on the aluminum disc is equal to total mechanical brake power generated [46]. There is also hysteresis loss on the rotor steel as a second heat source on rotor, but it is neglected due to being negligible comparing to mechanical brake power. In Equation (2.28),  $T_{\text{brake}}$  is torque;  $w$  is radial speed of RCB.  $P_{\text{disc}}$  is power dissipated on conductive disc.  $P_{\text{mech}}$  is the mechanical output.

$$T_b = \frac{P_{\text{disc}}}{w}, P_{\text{disc}} = P_{\text{mech}} \quad (2.28)$$

There are seven thermal mediums in proposed design: stator steel 1010, windings which are also heat source, inside air, the conductive disc which is also heat source, rotor steel 1010, pure aluminum rounded heat sink and outside air. The model is shown in Figure 2.11. According to the model thermal resistances:

In Equation (2.29),  $R_{\text{alu}/2}$  is the thermal conduction resistance of half of the aluminum alloy disc.  $r_{\text{od}}$  is outer radius of disc.  $r_{\text{ad}}$  is average radius of disc.  $r_{\text{id}}$  is inner radius of disc.  $k_{\text{alu}}$  is thermal conduction coefficient of aluminum disc.  $l$  is stator length.

$$R_{\text{alu}/2} = \frac{\ln(r_{\text{od}}/r_{\text{ad}})}{k_{\text{alu}}2\pi l} \approx \frac{\ln(r_{\text{ad}}/r_{\text{id}})}{k_{\text{alu}}2\pi l} \quad (2.29)$$

In Equation (2.30),  $R_{\text{steel}}$  is the thermal conduction resistance of rotor yoke.  $k_{\text{st}}$  is thermal conduction coefficient of aluminum disc.

$$R_{\text{steel}} = \frac{\ln(r_{\text{o}}/r_{\text{i}})}{k_{\text{st}}2\pi l} \quad (2.30)$$

In Equation (2.31),  $R_{\text{heat sink}}$  is the thermal convection resistance of rotor yoke. Thermal conduction resistance of it is neglected.  $A_1$  is total surface area of the heat sink.

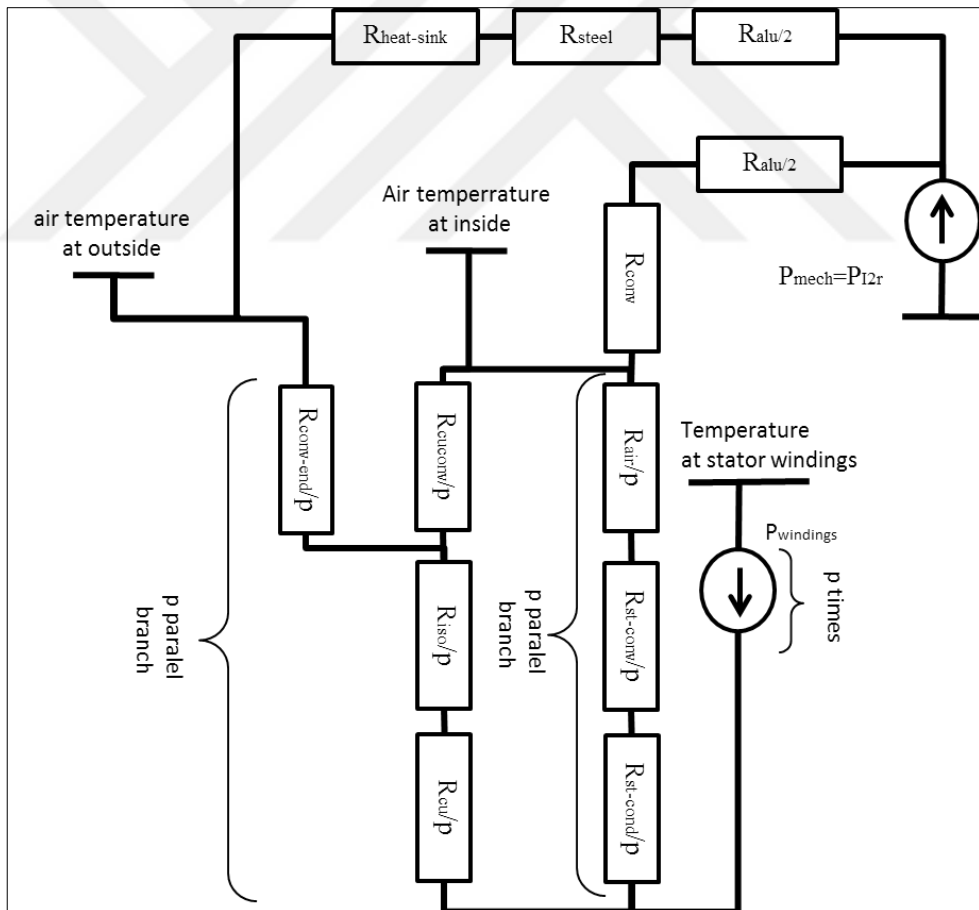


Figure 2.11. Thermal lumped model of the proposed ECB

$$R_{\text{heat sink}} = \frac{1}{h_{\text{sink}} A_1} \quad (2.31)$$

In Equation (2.32),  $R_{\text{conv}}$  is the thermal convection resistance of disc.  $A_2$  is total surface area of the inner side of the disc.

$$R_{\text{conv}} = \frac{1}{h_{\text{conv}} A_2} \quad (2.32)$$

In Equation (2.33),  $R_{\text{air}}$  is the thermal conduction resistance of inside air. The heat is conducted from disc to inside air then to stator pole steel.  $k_{\text{in-air}}$  is inside conduction coefficient.  $g$  is airgap length. There are  $R_{\text{air}}$  resistors connected in parallel as many as the number of poles in thermal model shown in Figure 2.11.

$$R_{\text{air}} = \frac{g}{k_{\text{in-air}} A_3} \quad (2.33)$$

In Equation (2.34),  $P_{\text{winding}}$  is the power generated on winding due to winding current  $I$  and copper resistance  $r_{\text{cu}}$ . There are  $P_{\text{winding}}$  sources as many as the number of poles.

$$P_{\text{winding}} = I^2 r_{\text{cu}} \quad (2.34)$$

In Equation (2.55),  $R_{\text{st-cond}}$  is the thermal conduction resistance of stator tooth.  $k_{\text{st}}$  is inside conduction coefficient. There are  $R_{\text{st-cond}}$  resistors connected in parallel as many as the number of poles.  $A_4$  is the tooth area.

$$R_{\text{st-cond}} = \frac{L_{\text{th}}}{k_{\text{st}} A_4} \quad (2.35)$$

In Equation (2.36),  $R_{\text{st-conv}}$  is the thermal convection resistance of stator tooth.  $h_{\text{st}}$  is inside convection coefficient. There are  $R_{\text{st-conv}}$  resistors connected in parallel as many as the number of poles.  $A_5$  is the tooth area.

$$R_{\text{st-conv}} = \frac{1}{h_{\text{st}} A_5} \quad (2.36)$$

$h_{\text{conv}}$ ,  $h_{\text{sink}}$  Parameters are defined by the air flow ratio, due to this; fan with high CFM rate must be selected for 664 axle rpm.  $R_{\text{cu}}$ ,  $R_{\text{iso}}$ ,  $R_{\text{cu-conv}}$ , thermal resistances have more complicated parameters and they must be analyzed by 3D FEM thermal analysis

software. For analytical calculation, copper windings are assumed as rectangular layers as shown in Figure 2.12.

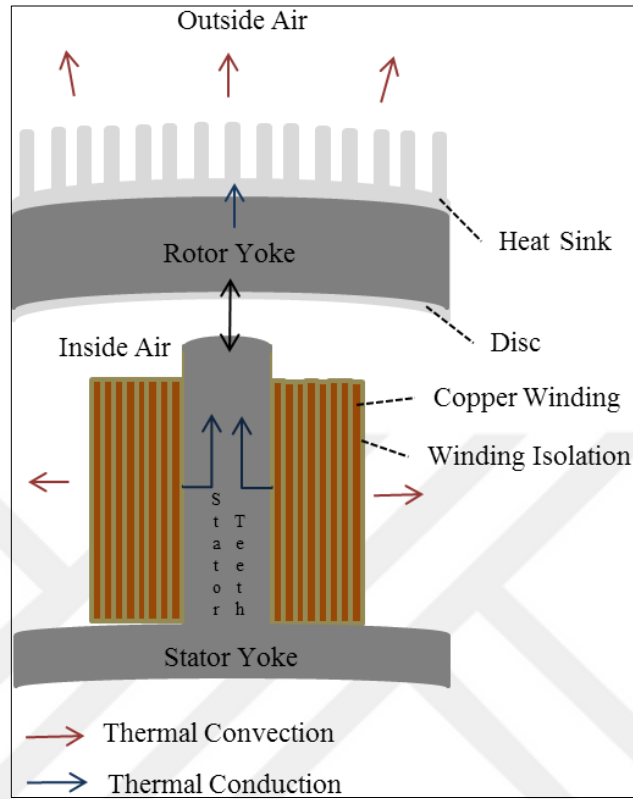


Figure 2.12. Thermal conduction and convection direction

In Equation (2.37),  $R_{\text{cu-cond}}$  is the thermal conduction resistance of copper.  $k_{\text{cu}}$  is conduction coefficient.  $A_6$  is the copper area.  $L_{\text{cu}}$  is the total length of copper.

$$R_{\text{cu-cond}} = \frac{L_{\text{cu}}}{k_{\text{cu}} A_6} \quad (2.37)$$

In Equation (2.38),  $R_{\text{iso}}$  is the thermal conduction resistance of total isolations.  $k_{\text{iso}}$  is conduction coefficient.  $A_7$  is the copper area.  $L_{\text{iso}}$  is the total length of isolation.

$$R_{\text{iso}} = \frac{L_{\text{iso}}}{k_{\text{iso}} A_7} \quad (2.38)$$

In Equation (2.39),  $R_{\text{iso-cov}}$  is the thermal convection resistance of isolation.  $h_{\text{iso}}$  is inside convection coefficient.  $A_8$  is the isolation area.



$$R_{\text{iso-conv}} = \frac{1}{h_{\text{iso}} A_8} \quad (2.39)$$

In Equation (2.40),  $R_{\text{end-conv}}$  is the thermal convection resistance of end winding.  $h_{\text{isofr}}$  is outside forced cooling convection coefficient.  $A_9$  is the isolation area.

$$R_{\text{end conv}} = \frac{1}{h_{\text{isofr}} A_9} \quad (2.40)$$

Analytical thermal results are investigated for final geometry in Chapter 4.

## 2.6. Material Selection

In the proposed design; core material, disc material, fan type and heat sink must be selected properly because this material has direct or indirect effect on torque vs speed curve.

### 2.6.1. Core material

There are several core materials: low carbon steel, silicon steel, %49 Nickel, %80 Nickel and Cobalt Alloy steel. Each material has some advantages and disadvantages which are seen in Table 2.1. According to the table, steel 1010 low carbon steel is selected. It is affordable, easy to process. Due to stator is excited by DC current, core loss is not too significant, and permeability and saturation flux densities are proper for the properties of proposed eddy current brake. The steels have similar thermal conductivity properties. BH curve of steel 1010 is shown in Figure 2.13. In common calculations, stator and rotor reluctances are neglected yet after saturation nearly 1.0 tesla relative permeability decreases dramatically. Hence, core reluctances have to be calculated. Due to this nonlinear characteristic of the core material, for analytical calculations iterative Newton-Raphson method is performed.

Table 2.1. Core material comparison [47]

Material type	Core Loss	Saturation Flux Density	Permeability	Ease of Process	Cost
Low Carbon S.	Fair	Good	Good	Best	Low
Silicon Steel	Good	Good	Fair	Good	Low
%49 Nickel	Good	Fair	High	Care Require	Fair
%80 Nickel	Better	Low	Best	Care Require	Fair
Cobalt Alloy	Good	Best	Good	Care Require	High

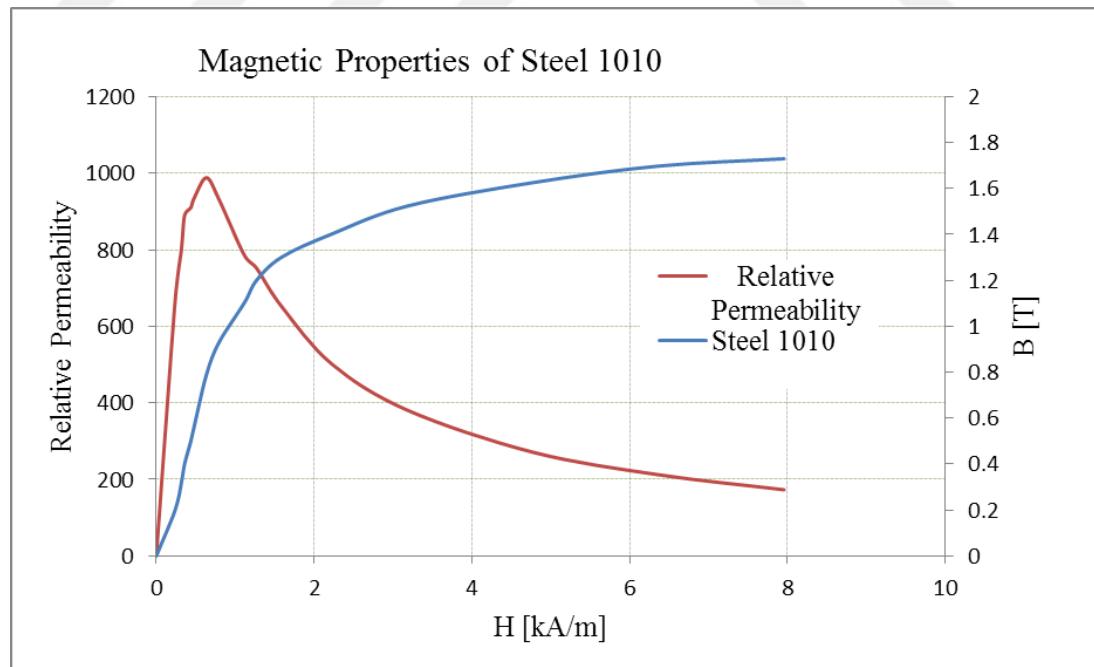


Figure 2.13. B H curve of steel 1010 [45]

### 2.6.2. Disc material

Disc material selection is essential for the torque vs speed curve. Via Equation (2.9), high conductive disc materials have more eddy current generating capacity but increasing eddy current also decreases magnetic flux density on airgap. Due to the reason, disc material must be selected according to the required nominal speed value. Due to disc thickness is very low, thermal conductivity is not essential parameter, but it is calculated in the thesis. Taking these parameters into consideration, the torque-speed characteristic for different disc materials will be evaluated and the final decision will be made in Chapter 4. In Figure 2.14, thermal and electrical conductivity of different disc materials are shown at 20°C.

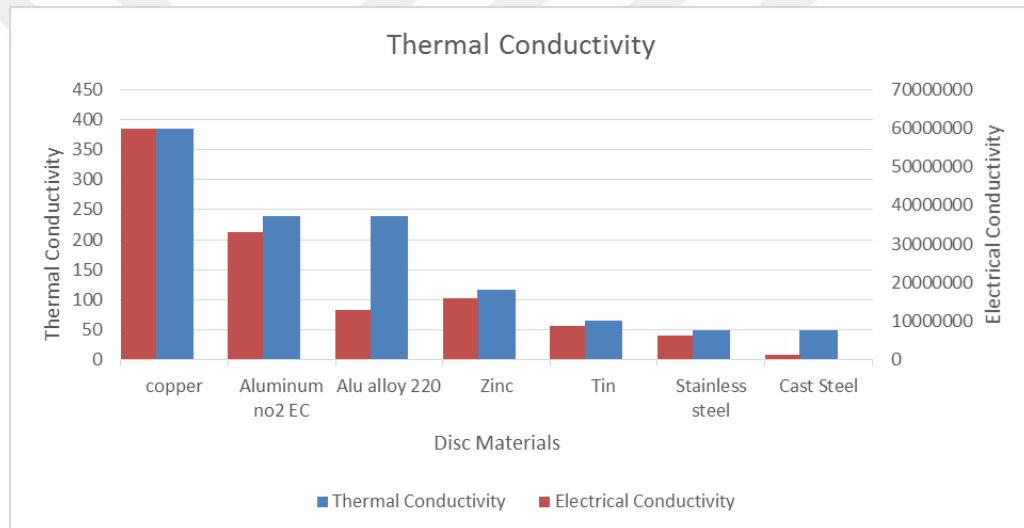


Figure 2.14. Thermal and electrical conductivity of the disc material at 20 ° C

In Figure 2.15, electrical conductivities versus temperature of different disc materials are shown. Materials electrical conductivities changes with temperature. Due to during brake, disc temperature radically increases, brake torque characteristics may change significantly.

In Equation (2.41), graph in Figure 2.16 is derived from Equation (2.19), all constants represented with A, B and C values:

$$T_b(w) = Aw\sigma_e^{-B\sigma w} e^{C\sigma w^{0.5}} \quad (2.41)$$

In Equation (2.42), Point at  $T_b(w)=0$  is the critical speed of the ECB. If  $e^{C_{(sw)}^{0.5}}$  is neglected, critical speed value is:

$$w = \frac{1}{B\sigma} \tag{2.42}$$

$B = 1.123E-09$  for proposed design.

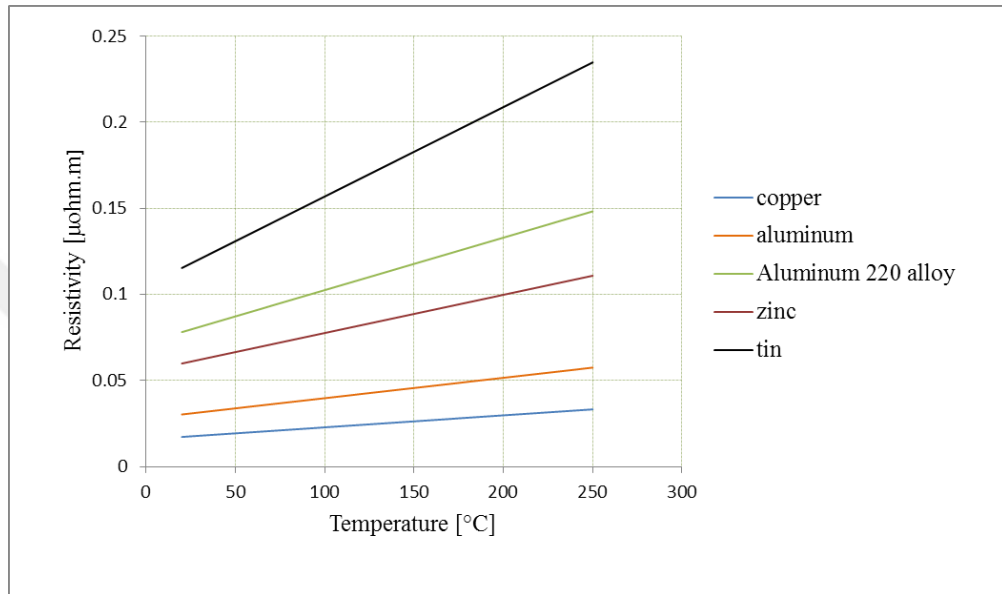


Figure 2.15. Electrical resistivity versus temperature for disc material

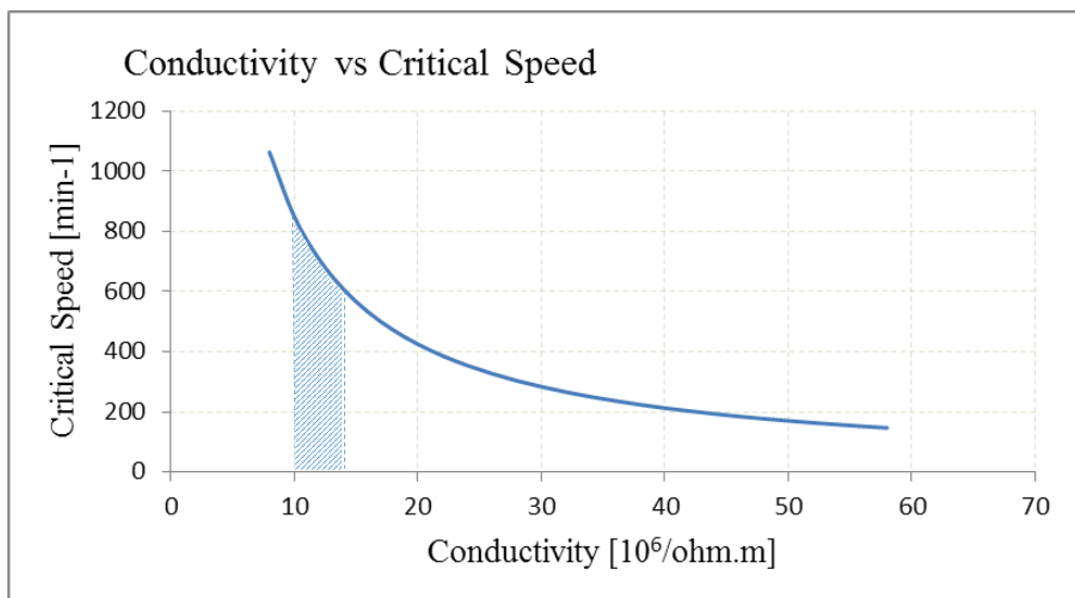


Figure 2.16. Conductivity of the disc material vs critical speed

As seen in Figure 2.16, to have a critical speed in range 600-800, conductivity of the disc material must be in range 10-13 Mega Siemens. In Figure 2.17, costs of the different disc materials are shown. Copper and tin metals have cost disadvantages. Unless, they are unique for the operation, they are not preferable.

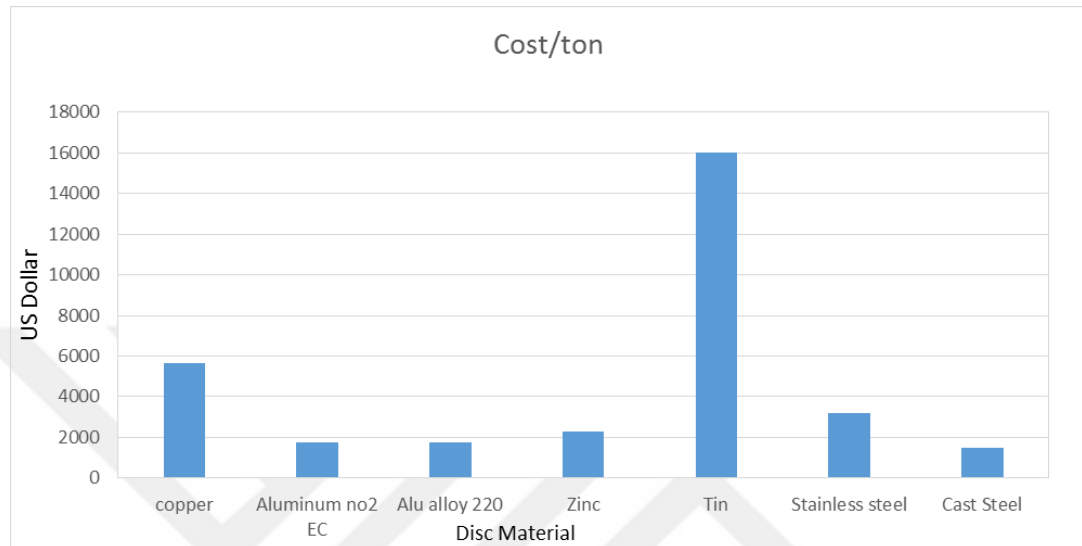


Figure 2.17. Cost for different disc materials

### 2.6.3. Heat sink

Heat Sink Selection is significant due to temperature increase on copper isolation and conductivity of the disc. The generated heat must be exhausted so efficiently that

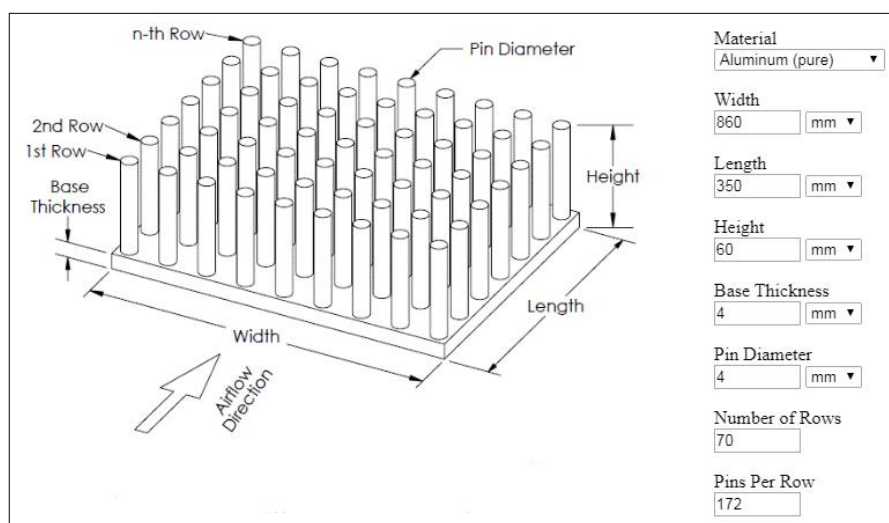


Figure 2.18. Linear projection of proposed 3D cylindrical heat sink

winding temperature would not exceed 180°C for H class windings. Heat sink is selected round pin type as shown in Figure 2.18. because it has the wider cooling area than flat pin type and has lower thermal resistance. To calculate heat sink side, online calculator was used [48]. According to the available heat sink and forced cooling fan data, heat sink thermal resistance is 0.00166°C/W. The resistance of the heat sink is inversely proportional to CFM rate of the fan. There is also radial ventilation way of the design. With this, rotating heat sink will create vacuum effect in the surface, and it results additional air flow, it will provide additional cooling. However, due to complexity of the calculations, it requires CFD software analysis; the calculation is not included for the thesis.

#### 2.6.4. Fan

Fan has a significant effect on thermal resistance because the cfm -cubic flow in a minute- rate changes conduction coefficient. Blade shapes, blade angle, number of blades on fan are the main factors affecting CFM. To have a reference, an automotive fan blade is selected which is shown in Figure 2.19, [49]. At 2380 min<sup>-1</sup> it has 2500 cfm. By using online calculator, for 8-inch diameter fan blades, LFM value is 501.34 [49]. This LFM value is used on thermal resistance calculations.



Figure 2.19. Selected fan blades to have a reference cfm ratio

### **3. COMPARISON OF THE GEOMETRICAL VARIATIONS ON PROPOSED ECB BY ANALYTICAL CALCULATIONS AND FEA SIMULATIONS**

According to the book design of rotating electrical machines [15], current density at windings must be between  $3 \text{ A/mm}^2$  and  $8 \text{ A/mm}^2$ . The current density is selected as  $5 \text{ A/mm}^2$  due to thermal concerns. To compare the effect of ECB variables on brake torque, while one variation is changing, other variables are taken as constant during simulation. As a beginning, regarding average manufacturability parameters of the module, airgap distance is selected as 2 mm. Disc thickness is selected as 2 mm. Pole pitch ratio is selected as a 0.3. Number of poles is selected as 12 regarding Equation (2.4) and Equation (2.5).

#### **3.1. Disc Conductivity Comparison**

As discussed, conductivity of disc has a direct effect on torque speed curve. In Figure 3.1, torque speed curves of ECB with different disc materials are seen. Copper disc has the maximum torque value at low speed, because it generates more eddy current on the disc, Equation (2.10). However, at higher speed, while generated eddy current value increases proportional to speed, also armature reaction increases and opposes to main flux density. This reduces magnetic flux density on the disc. Via Equation (2.10) and Equation (2.12), due to torque is proportional to square of magnetic flux density, torque for ECB with copper disc begin to decrease at lower speed than other ECBs. Regarding the opposite edge, due to high resistance of stainless steel, maximum speed of the ECB is lower than other ECBs while critical speed is higher than other ECB. As a brief, to decide disc material, working range must be taken into consideration. In the thesis, regarding required speed range and brake torque values, Alu alloy 220 has a proper speed vs torque curve, seen in Figure 3.2. Also, as an option, Zinc disc may be used according to the thermal result of the disc.

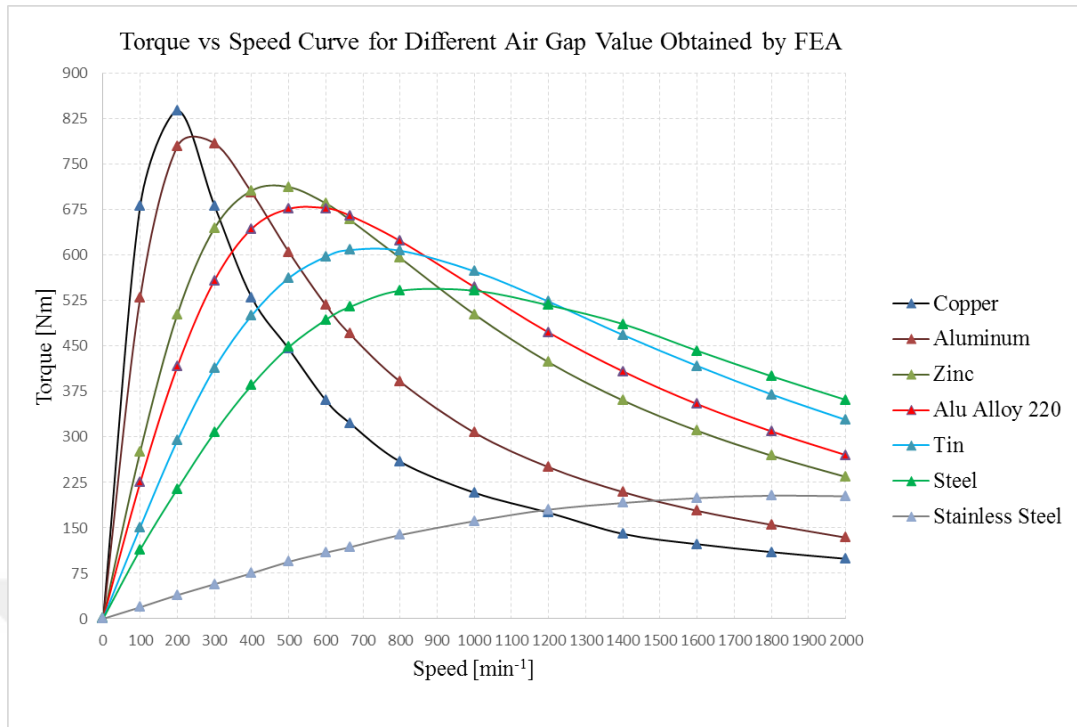


Figure 3.1. Torque speed curve for different disc material obtained by 2D FEA

If the temperature on the disc increases beyond expected value, due to increase of the resistance on disc Equation (2.18), disc material must be reselected.

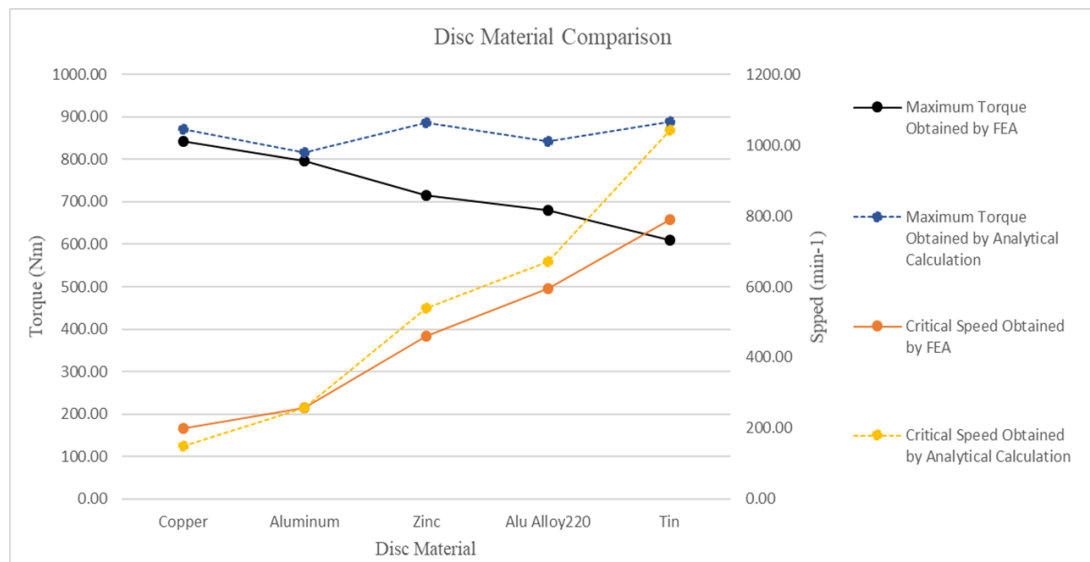


Figure 3.2. Maximum torque and critical speed values

In Figure 3.3, results of analytical calculations are seen. In table 5, analytical calculation parameters are given, and the calculation is performed by using Equation



(2.19). In analytical calculations, critical speed values have %1 error comparing to FEA results. However, maximum torque results have error. With decreasing conductivity, the error increases. The reason of it is that flux density waveforms in the

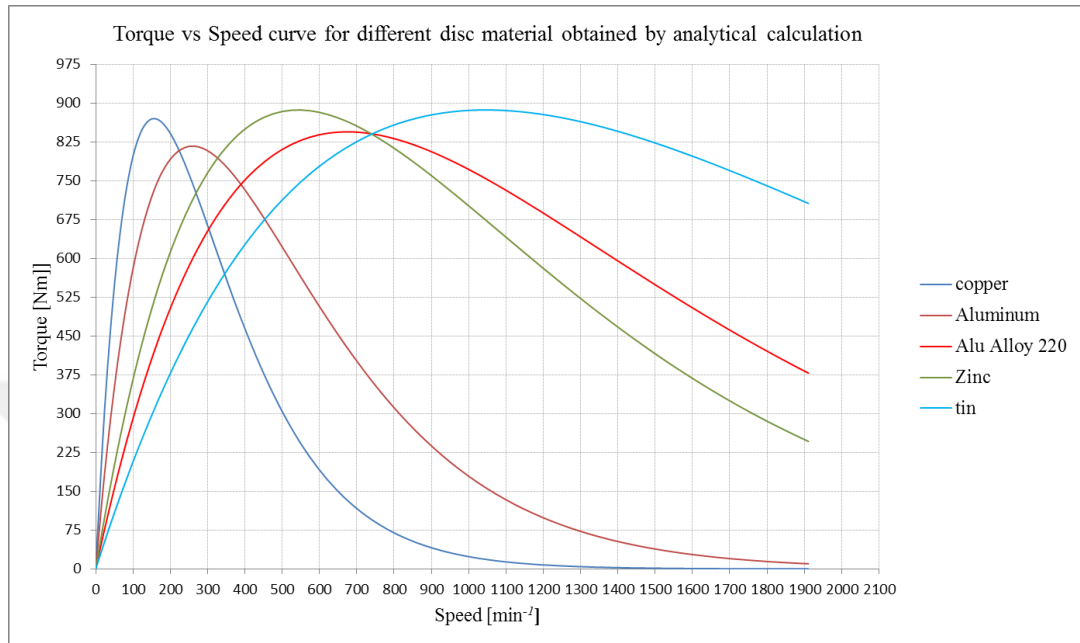


Figure 3.3 .Torque speed curve for different disc material obtained by analytical calculations

disc are different. Even if average values of flux densities are the same via analytical approach with Reynold's number, their rms values are different. Hence the correction coefficient K may differ for each disc material.

Table 3.1.Parameters used in analytical calculations for different disc materials

$A_w$ [mm <sup>2</sup> ]	540.25	Characteristic length [mm]	3.61
$J$ [A/mm <sup>2</sup> ]	5	Radius [m]	0.119

Table 3.1. (Continued) Parameters used in analytical calculations for different disc materials

Ni [At]	2701.25	t [m]	0.002
R <sub>gap</sub> [H <sup>-1</sup> ]	293373.2	τ	0.3
R <sub>tooth</sub> [H <sup>-1</sup> ]	5896.3	l [m]	0.35
R <sub>yoke-rt/4</sub> [H <sup>-1</sup> ]	1362	K	1.6
R <sub>yoke-st/4</sub> [H <sup>-1</sup> ]	2627	σ [S/m]	Variable
B <sub>0</sub> [T]	0.837	p	12
μ <sub>0</sub> [H/m]	4π·10 <sup>-7</sup>		

### 3.2. Pole Pitch Ratio

To create maximum torque within the initial parameters, pole pitch ratio analysis is performed. Equation (3.1) shows calculation of the pole pitch ratio.  $a_{\text{tooth}}$  is half of the pole angle.  $a_{\text{pp}}$  is half of the tooth angle shown in Figure 3.4.

$$\tau = \frac{a_{\text{tooth}}}{a_{\text{pp}}} \quad (3.1)$$

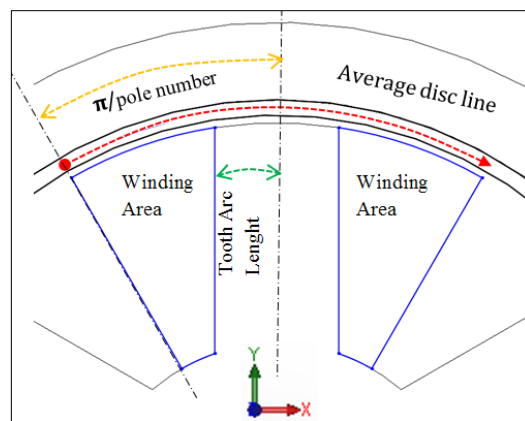


Figure 3.4. Determination of angle for pole pitch calculation

Pole pitch ratio values are simulated between % 15 and %30. The recommended tooth slot pitch is between 7mm to 45 mm. if, as an initial parameter, number of poles is selected 12, tooth length changes between 9.1mm to 18.22 mm. According to the equation (2.4), the smaller pole pitch ratio increases winding area and for constant current density design, it increases magneto motive force equation (2.5). Due to this, until optimum value; torque-speed curve of ECB has better curve while stator tooth is becoming small. However, after the optimum value, the tooth core begins to saturate. After that point, due to nonlinear curve of the electrical steel, Condition,  $R_g \gg R_{t0}$  changes and  $R_{t0}$  increases radically. This decreases magnetic flux density on disc. As seen in Figure 3.5., after %22,5 pole pitch ratio, maximum torque curve begins to decrease.

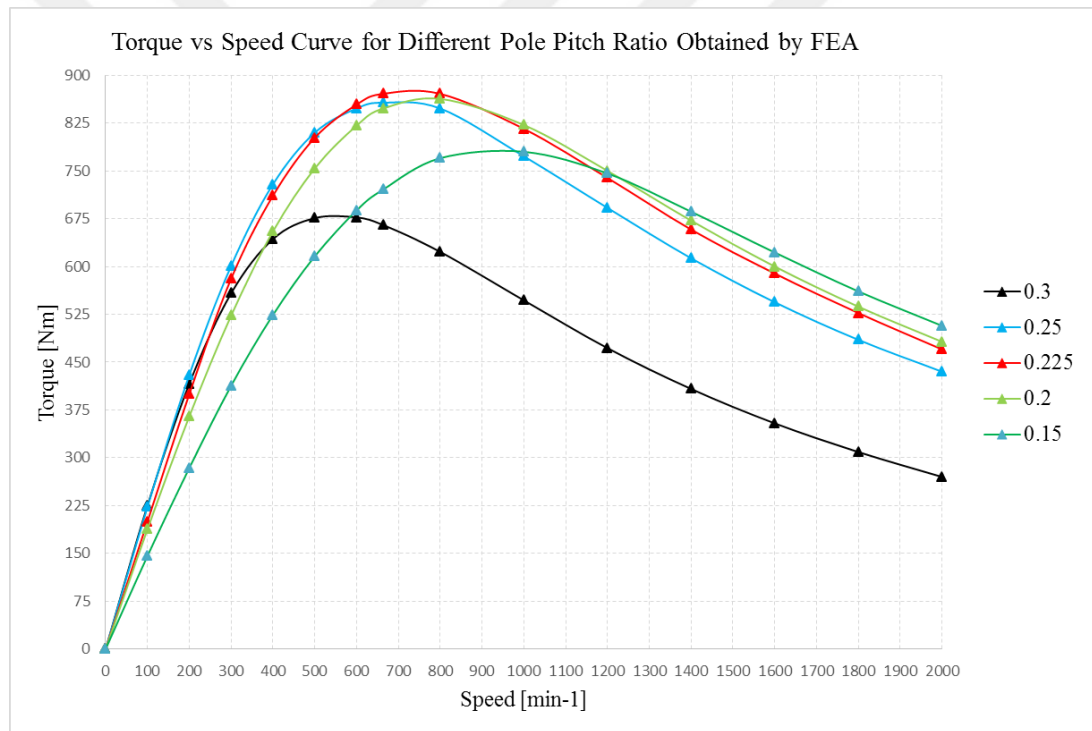


Figure 3.5. Torque vs speed curves of different pole pitch ratio obtained by 2D FEA

If we analyze the critical speed, it is seen that stators having lower pole pitch ratio has higher critical speed values. In other words, geometries having thinner tooth are affected less from armature reaction. That is why; as a second magneto motive force source, generated eddy current in Figure 2.3, has a magnetic flux way passing through stator tooth. Thicker pole tooth provides lower reluctance on the way of the flux. Due

to this, at constant airgap geometry thicker tooth geometries are much more affected from armature reaction. As a result, thicker tooth ECB have lower critical speed. Critical speed and Maximum Torque curves are seen in Figure 3.5. For



Figure 3.6. Maximum torque and critical speed values of different pole pitch ratios

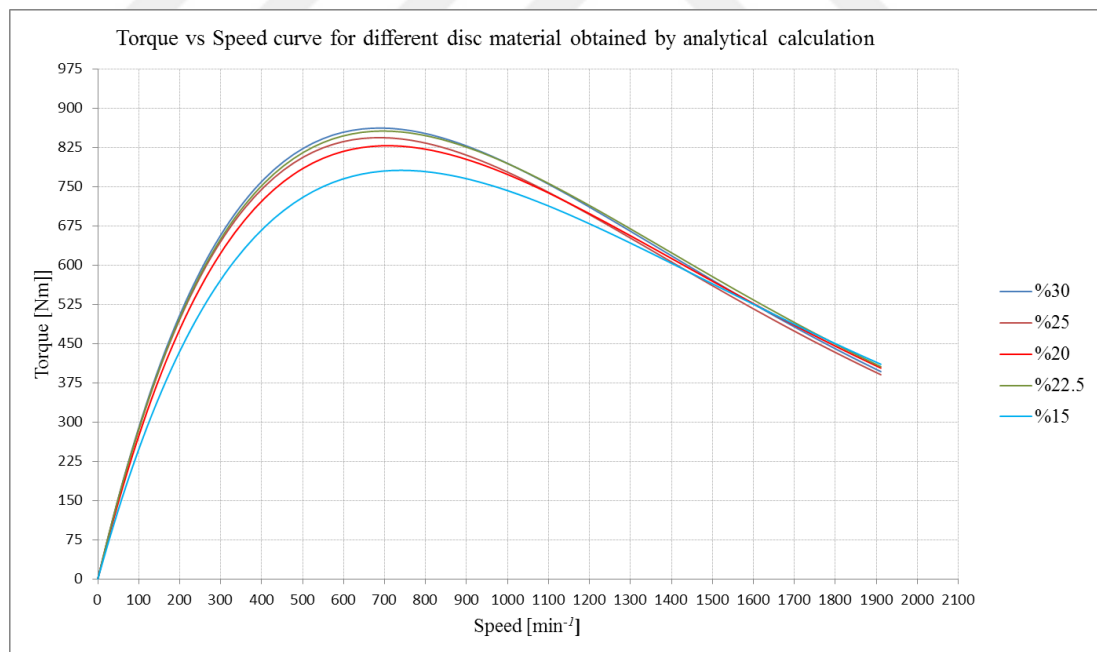


Figure 3.7. Torque speed curve for different pole pitch ratio obtained by analytical calculations

required ECB properties %22.5 pole pitch ratio is selected. In Figure 3.7, results of analytical calculations are seen. In Table 3.2, analytical calculation parameters are given, and the calculation is performed by using Equation (2.18). For  $B_0$  calculation, relative permeability of core is assumed constant by neglecting saturation. Even if this kind of calculation approach has an error on linear region, it has more accurate results on stable and reduction region due to armature reaction. Comparing to FEA simulation, critical speed value of %15 is quite different. The reason of it is saturation. Saturated cores have higher critical speed.

Table 3.2. Parameters used in analytical calculations for different pole pitch ratios

$\tau$ [%]	30	25	22.5	20	15
$A_w$ [mm <sup>2</sup> ]	540.25	600.71	630.38	659.71	711.68
$N_i$ [At]	2701.25	3003.55	3151.9	3298.55	3558.4
$R_{gap}$ [H <sup>-1</sup> ]	293373.2	359469.1	385363	411518.9	475906
$R_{tooth}$ [H <sup>-1</sup> ]	5549	6658.87	7434	8355	11100
$R_{yoke-rt}/4$ [H <sup>-1</sup> ]	2160	2160	2160	2160	2160
$R_{yoke-st}/4$ [H <sup>-1</sup> ]	1495	1495	1495	1495	1495
$B_0$ [T]	0.837	0.917	0.968	1.034	1.084
Characteristic length [mm]	3.61	3.54	3.5	3.44	3.29

### 3.2.1. Small scaled prototype comparison on pole pitch ratio

In the beginning of the thesis, a prototype work was performed. The aim of the prototype work was to validate the analytical results with experimental results. However, due to financial restrictions the work was finished with performed simulation.

Table 3.3. Prototype ECB dimensions and nominal design parameter

Parameter	Value
Rotor Yoke $r_o$	70 mm
Rotor Yoke $r_i$	56 mm
Stator Yoke $r_o$	18 mm
Stator Yoke $r_i$	10 mm
Stator Tooth Length	34 mm
Axial Length	30 mm
Disc Thickness	2 mm
Air Gap Distance	2 mm
Disc Material	Aluminum
Core Material	Steel 1010
Nominal Speed	1000 $\text{min}^{-1}$
Maximum Torque	10 Nm
Nominal Current density on windings	5A/ $\text{mm}^2$

According to the simulation performed, maximum torque is detected at  $0.2 \tau$ . It is similar to the proposed ECB results as seen in Figure 3.8.

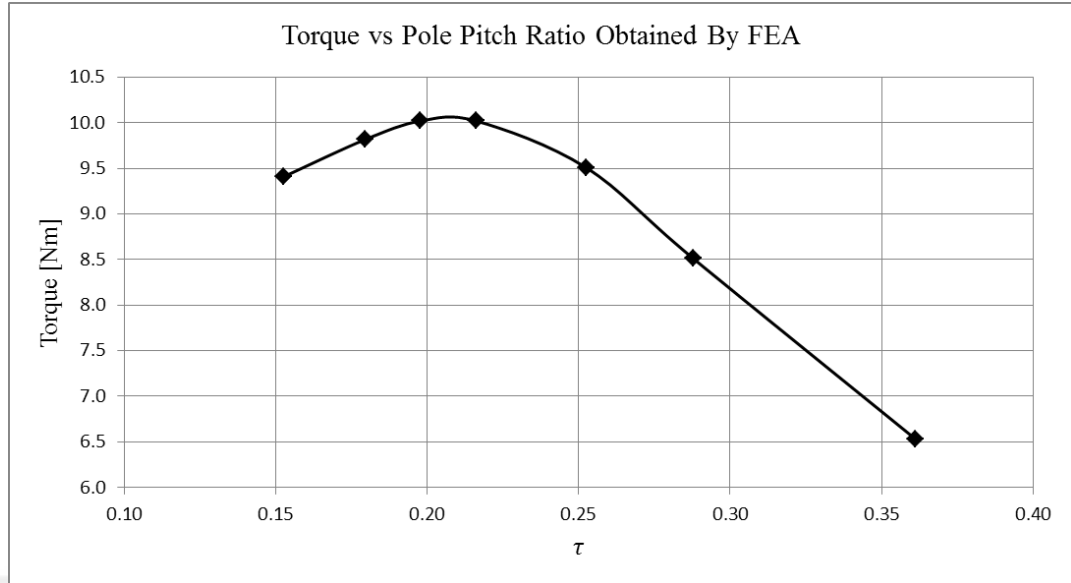


Figure 3.8. Small Scaled ECB Torque vs Pole Pitch Ratio Curve at 1000 min<sup>-1</sup> obtained by 3D FEA

### 3.3. Number of Pole

Via Equation (2.4), increasing pole number decreases winding area. At constant current density design which causes decrease in magneto motive force. Due to  $R_g \gg R_{steel}$  and  $R_g \approx R_{al}$  conditions, equation may be derived as:

$$Ni = R_g B A_g \quad (3.2)$$

$$R_g = \frac{l_g}{A_g \mu_0} \quad (3.3)$$

Equation (3.4) is derived via Equation (2.5) and Equation (2.1):

$$Ni = \frac{4l_g}{\mu_0} B \quad (3.4)$$

As a result, increased pole number decreases magnetic flux density on the disc. Then squarely proportional to decrease of B, torque per pole decreases while total torque increases proportional to pole number. As a result, total torque decreases inversely proportional to pole number as seen in Figure 3.10. If it is closely investigated, it would be seen that from 4 poles to 6 poles linearly decrease disappears. This is due to saturation on the electrical steel.

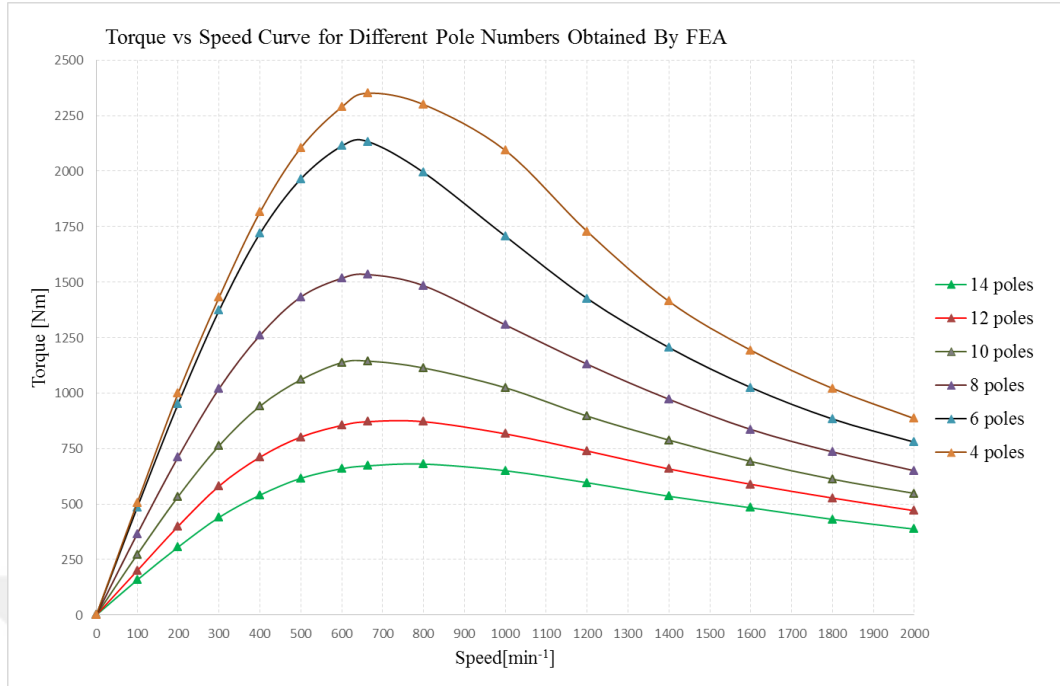


Figure 3.9. Torque Speed Curve For different number of poles obtained by 2D FEA

At four pole magneto motive force is so high that it would saturate the core despite armature reaction, increase total reluctance and decrease magnetic flux density on the disc. It is also seen in Figure 3.9 that number of poles has no effect on critical speed. According to the simulation result, 4 and 6 poles geometry has a small difference. To choose 4 poles geometry will increase both end-winding distance and axial length of the ECB. Via this, 6 poles geometry is selected. Another design criteria is production cost. With increasing number of poles, production cost increases exponentially. In Figure 3.11, results of analytical calculations are seen. In table 9, analytical calculation parameters are given, and the calculation is performed by using Equation (2.19). For calculation of  $B_0$  with 6 and 8 poles geometries, total magneto motive force [At] is divided by 0.6 which is the  $e^{-R^m}$  value at maximum torque. Due to geometries with 4 and 6 poles have saturation, at stable and reduction region armature effect is eliminated by saturation.



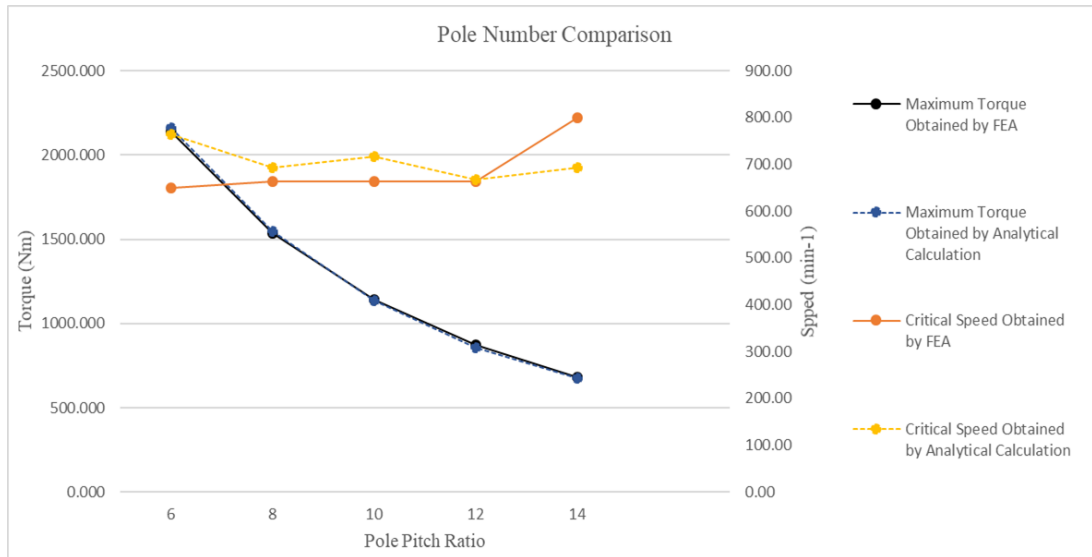


Figure 3.10. Maximum torque and critical speed values for different pole numbers

Hence, in analytical approach,  $B_0$  is calculated by adding negative magneto motive.

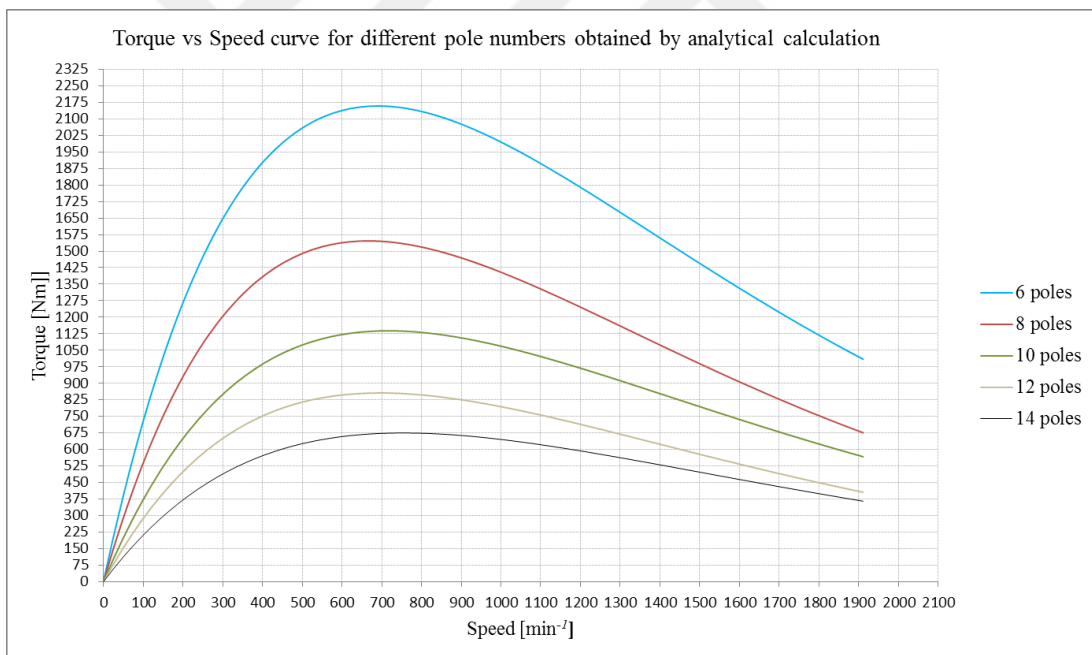


Figure 3.11. Torque speed curve for different pole numbers obtained by analytical calculations

Comparing to FEA simulation, critical speed values have maximum %6 errors. Maximum torque values have maximum %2 errors.

Table 3.4. Parameters used in analytical calculations for different pole numbers

p	6	8	10	12	14
$A_w$ [mm <sup>2</sup> ]	1331.26	989.29	771.99	630.38	529.44
Ni [At]	6656.3	4946.45	3859.95	3151.9	2647.2
$R_{gap}$ [H <sup>-1</sup> ]	182611.7	222149	276044	385363	419104
$R_{tooth}$ [H <sup>-1</sup> ]	561924	303750	280805	7434	8641
$R_{yoke-rt}/4$ [H <sup>-1</sup> ]	4320	3240	2592	2160	1851
$R_{yoke-st}/4$ [H <sup>-1</sup> ]	2980	2240	1792	1495	1281
$B_0$ [T]	1.55	1.33	1.10	0.968	0.829
Characteristic length [mm]	3.73	3.65	3.57	3.5	3.42

### 3.3.1. Small scaled prototype comparison on number of poles

It is also seen in Figure 3.12, while number of poles increasing, due to decreased winding area and then total magneto motive force, total torque is decreasing. It is similar to Figure 3.11. Total torque is proportional with  $B_{gap}^2 p$ , as seen in Figure 3.12 and Figure 3.13, despite of increasing number of poles, dominant effect of  $B_{gap}$  linearly decreases total torque.

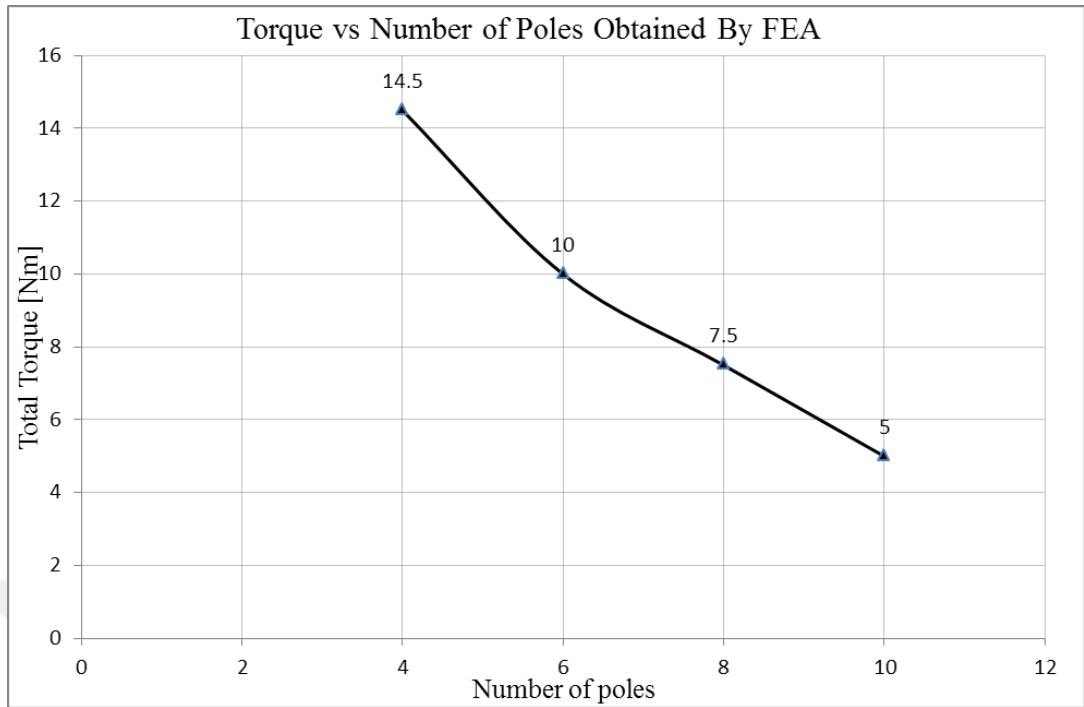


Figure 3.12. Total torque vs number of poles at  $1000 \text{ min}^{-1}$  obtained by 3D FEA

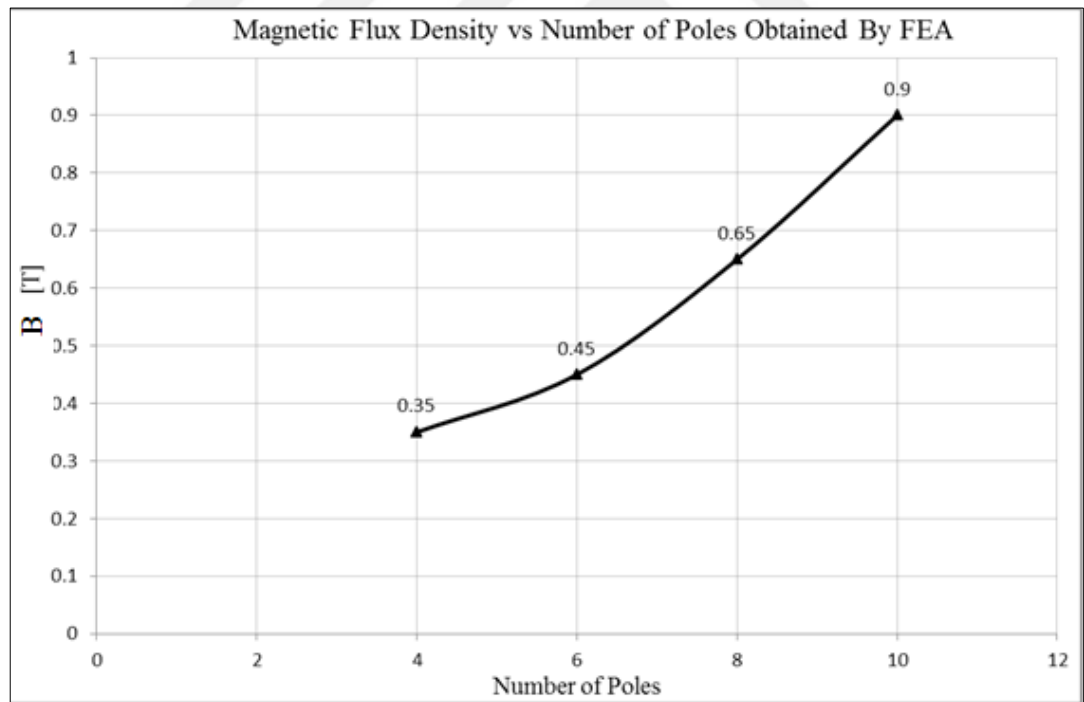


Figure 3.13.  $B_{\text{gap}} \text{ max}$  vs number of poles at  $1000 \text{ min}^{-1}$  obtained by 3D FEA

### 3.4. Disc Thickness

At low speed region, the thicker disc contains more current proportional to disc thickness via Equation (2.13). However, at middle and high speed region, proportional to generated eddy current, they are affected to armature reaction and magnetic flux in the disc decreases. As a result thinner disc contains less eddy current, is effected less from armature reaction at same speed and have higher critical speed value, Figure 3.14. As seen in Figure 3.15, there is small difference at maximum torque for different disc thickness. Then selection must be done by critical speed. 1.5mm disc thickness is selected.

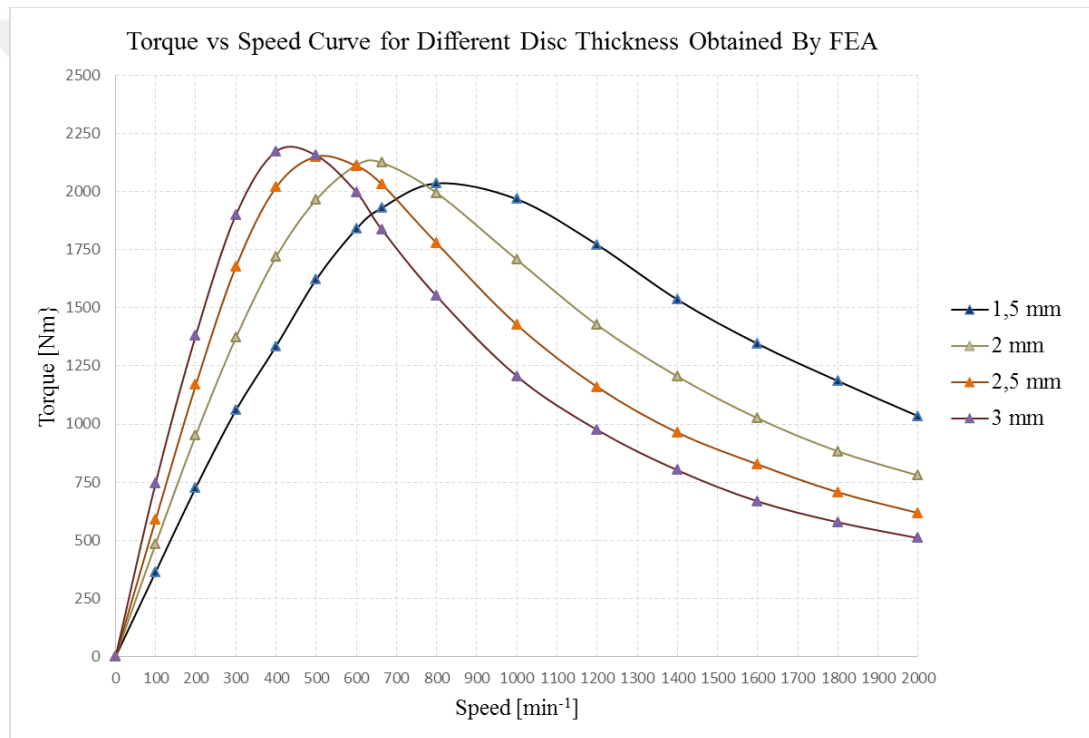


Figure 3.14. Torque speed curve for different disc thicknesses obtained by 2D FEA

In Figure 3.16, results of analytical calculations are seen. In table 3.5, analytical calculation parameters are given. Comparing to FEA simulation, critical speed values have maximum %6 errors. Maximum torque values have maximum %3.5 errors.

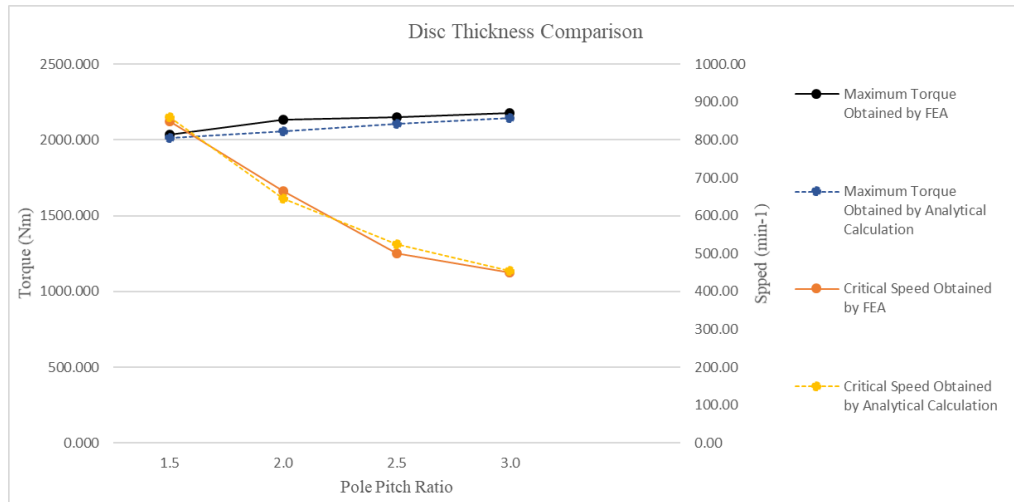


Figure 3.15. Maximum speed and critical speed for different disc thicknesses

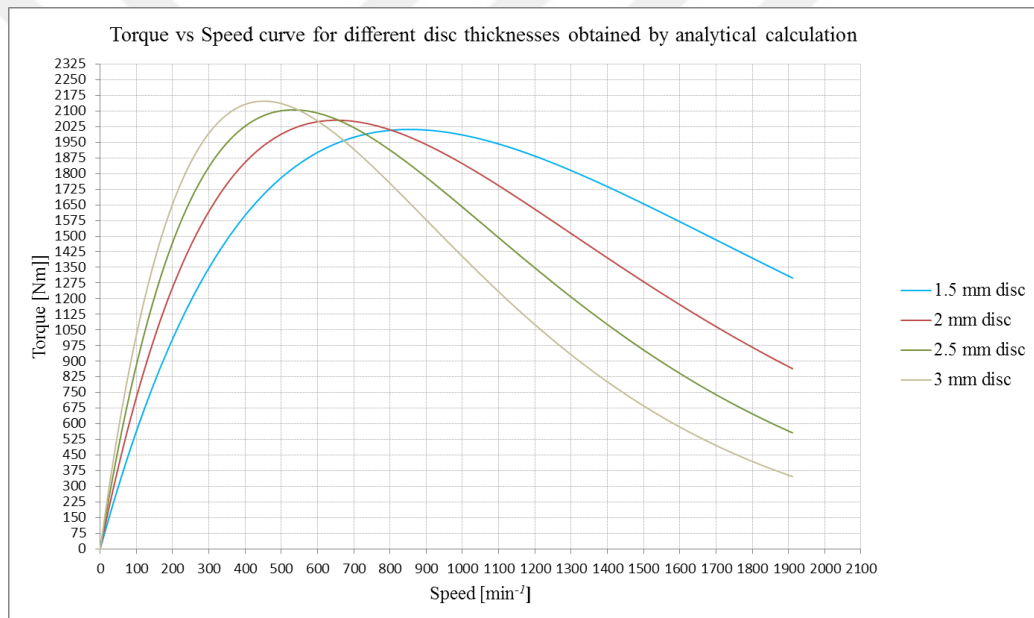


Figure 3.16. Torque speed curve for different disc thicknesses obtained by analytical calculations

Table 3.5. Parameters used in analytical calculations for different disc thicknesses

Disc Thicknesses [mm]	1.5	2	2.5	3
Characteristic length [mm]	3.73	3.65	3.57	3.5

### 3.4.1. Small scaled prototype comparison on disc thicknesses

As seen in Figure 3.17, similar to Figure 3.14, thicker discs are affected much more by armature effect. Comparing small scaled and the proposed ECB, they have similar characteristic about disc thickness. In prototype work, 2mm disc was selected because

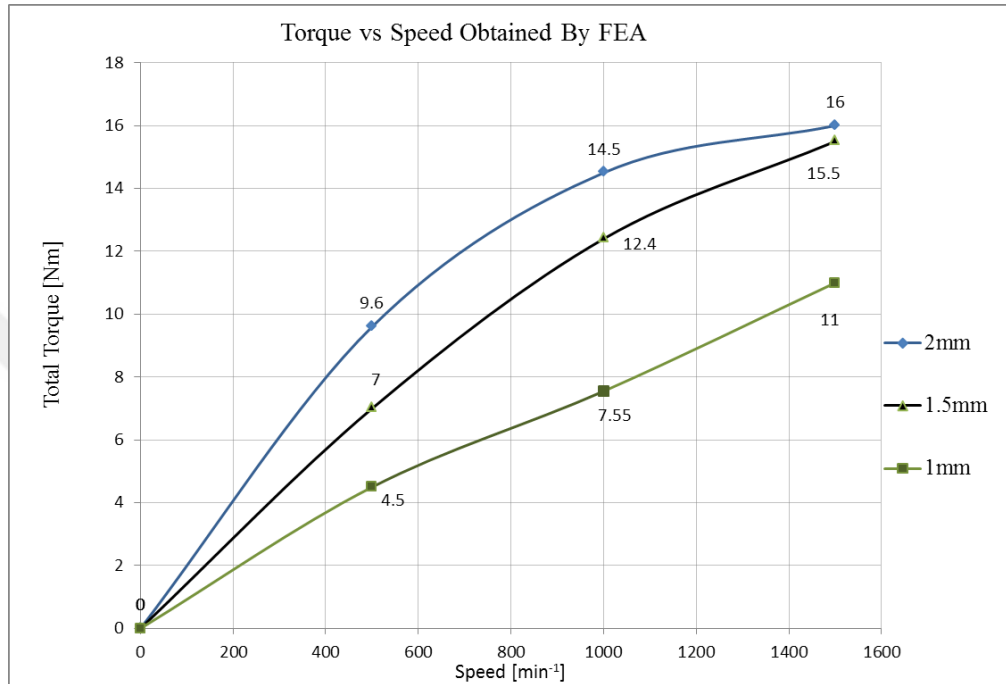


Figure 3.17. Speed vs torque curve with different disc thickness at 1000 min<sup>-1</sup> obtained by 3D FEA

the curve was proper for speed and curve requirement of the test setup. However, in the proposed ECB, disc thickness is selected 1.5 mm due to difference in requirement.

### 3.5. Airgap Distance

From Equation (2.3), increasing airgap increases reluctance. Increasing reluctance causes to decrease flux and airgap flux density on the disc, Equation (2.1), Equation (2.2). Higher flux density results a higher torque output, seen in Figure 3.18. Due to mechanical constraints, smaller airgap than 1.5mm is not affordable. Because of the better torque output, 1.5mm airgap is selected. Figure 3.20, results of analytical calculations is seen. In table 10, analytical calculation parameters are given.

Comparing to FEA simulation, critical speed values have error less than %1. Maximum torque values have maximum %2.3 errors.

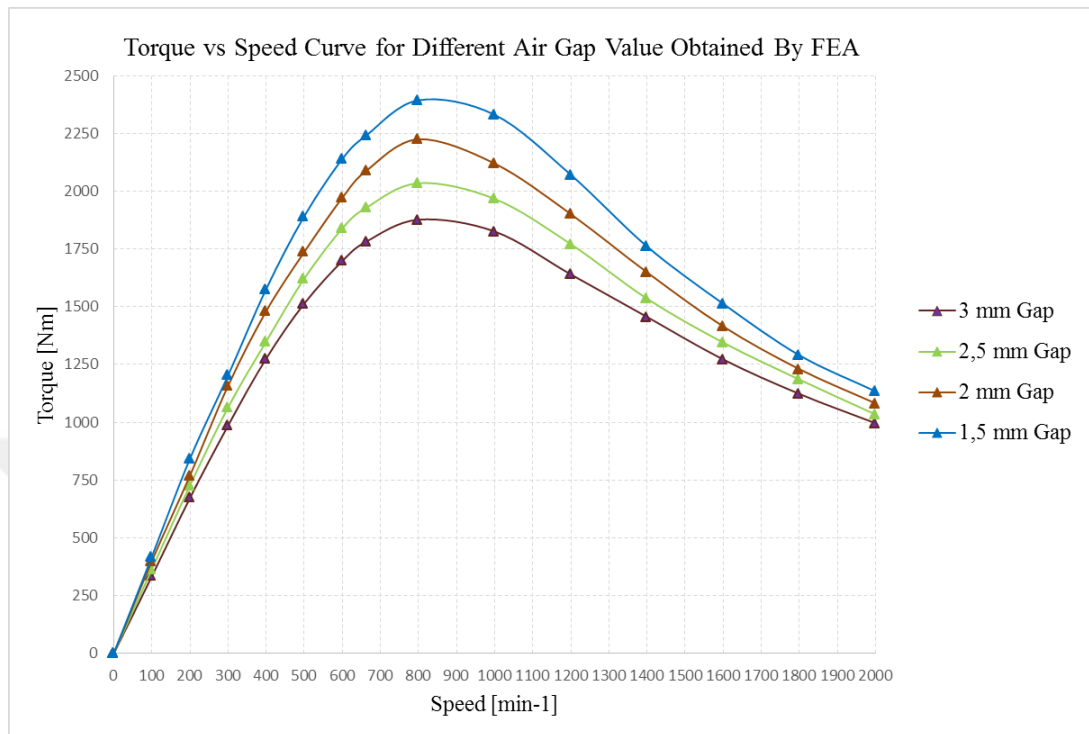


Figure 3.18. Torque speed curve for different airgap obtained by 2D FEA

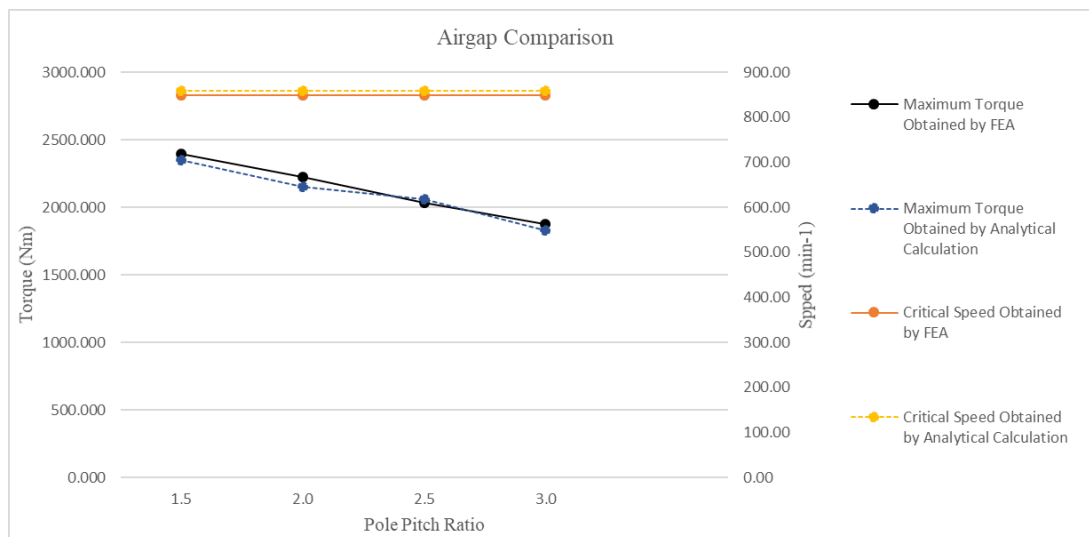


Figure 3.19. Maximum speed and critical speed for different airgaps

Table 3.6. Parameters used in analytical calculations for different air gaps

Airgap [mm]	1.5	2	2.5	3
$R_{gap} [H^{-1}]$	109566.6	146088.8	182611.7	219133.2

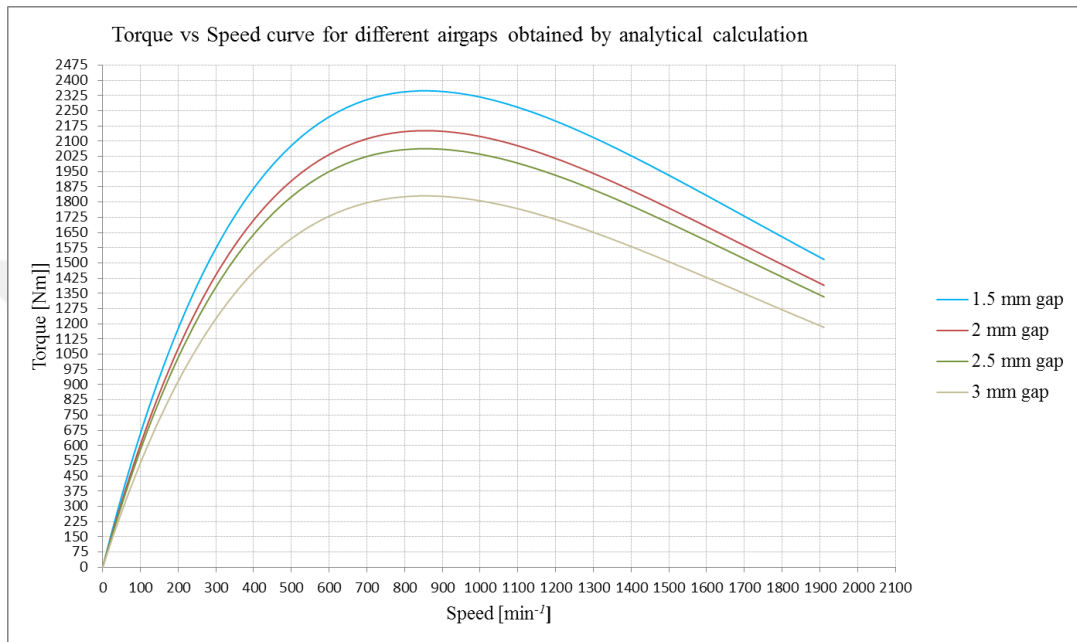


Figure 3.20. Torque speed curve for different airgap obtained by analytical calculations

### 3.5.1. Small scaled prototype comparison on number of poles

As seen in Figure 3.21, small scaled ECB and the proposed ECB have similar torque vs speed curve with changing air gap.



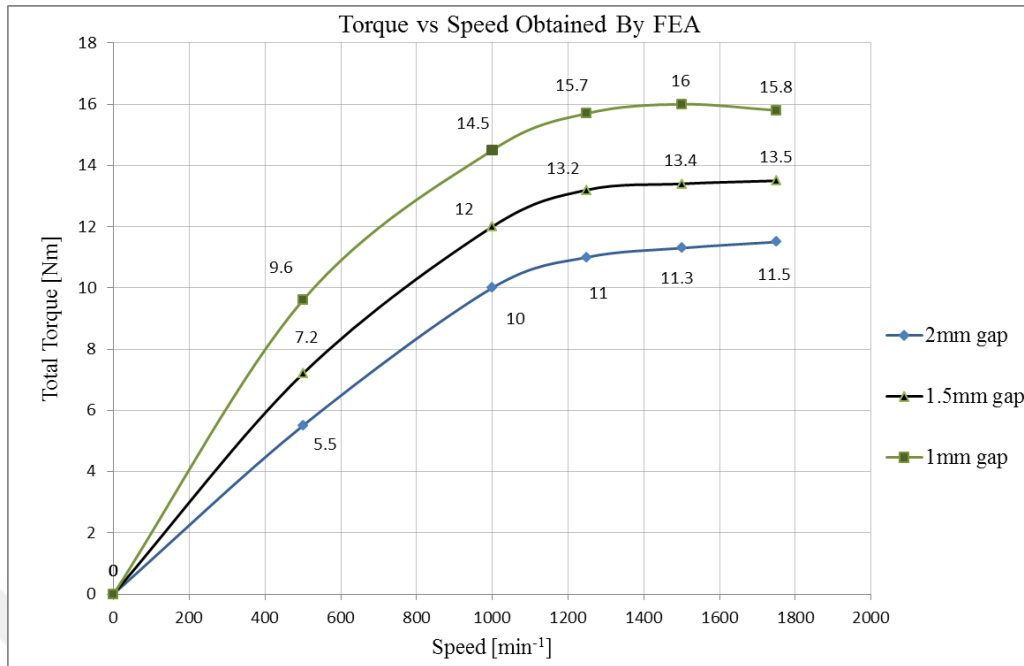


Figure 3.21. Air gap distance vs total torque obtained by 2D FEA

### 3.6. Rotor Thickness

In previous analysis, not to affect torque curve negatively, rotor thickness is selected in wide thickness. It means that to reduce volume, rotor thickness can be reduced

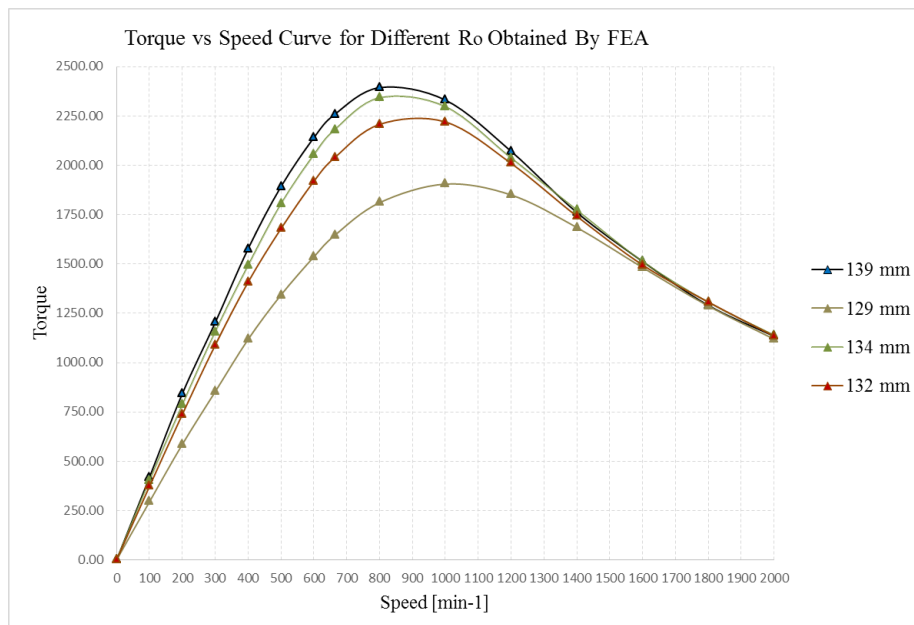


Figure 3.22. Speed vs torque graph for different rotor yoke thicknesses obtained by 2D FEA

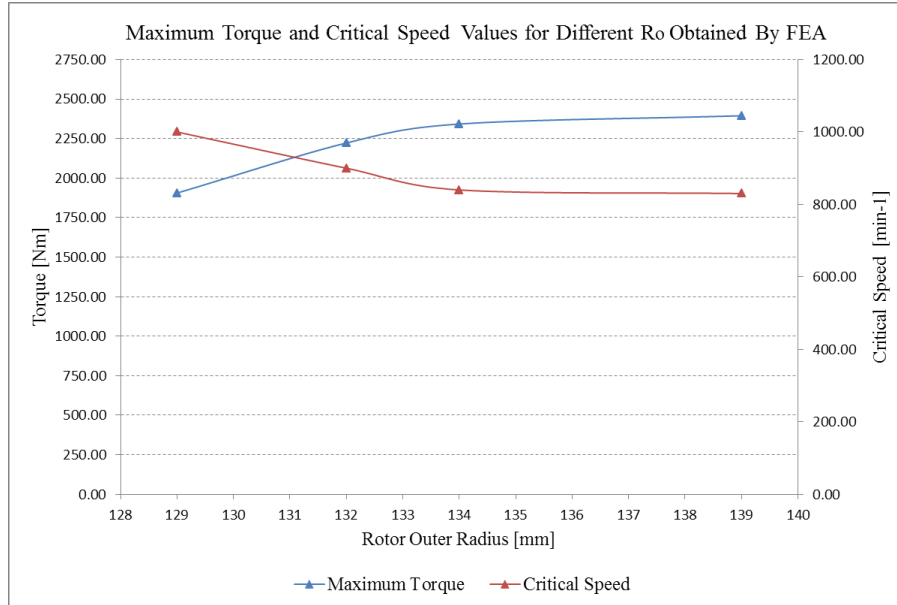


Figure 3.23. Critical speed and maximum torque vs rotor thickness graph obtained by 2D FEA

until rotor saturated. The saturation level is about to 1.7-2.0 Tesla. After that value, due to radically increased magnetic resistance of rotor yoke, magnetic flux density on the disc decreases radically. Then total brake torque decreases proportional to decrease of square of the magnetic flux density via Equation (2.19). The results are seen in Figure 3.22 and Figure 3.23.

### 3.7. Thermal Calculation

Based on selected final geometry and thermal equations, disc temperature and winding temperatures are calculated. The calculation parameters are shown in Table 12. The temperature values according to analytical approach are shown Table 13.

Table 3.7. Thermal calculation results for final geometry

$k_{alu}$ [W/m K]	240	$R_{conv}$ [K/W]	0.386
$k_{st}$ [W/m K]	51.9	$R_{air}$ [K/W]	4.38
$h_{conv-st}$ [W/m <sup>2</sup> K] (low speed air)	10	$R_{st-cond}$ [K/W]	0.081

Table 3.7. (Continued) Thermal calculation results for final geometry

$h_{\text{conv-fr}}$ [W/m <sup>2</sup> K] (forced air)	100	$R_{\text{st-conv}}$ [K/W]	2.09
$k_{\text{air}}$ [W/m K]	0.026	$R_{\text{cu-cond}}$ [K/W]	$4.93 \cdot 10^{-3}$
$k_{\text{cu}}$ [W/m K]	401	$R_{\text{iso}}$ [K/W]	1.01
$k_{\text{iso}}$ [W/m K]	0.44	$R_{\text{iso-conv}}$ [K/W]	1.9
$R_{\text{alu/2}}$ [K/W]	$1.2 \cdot 10^{-5}$	$R_{\text{conv-end}}$ [K/W]	0.57
$R_{\text{steel}}$ [K/W]	$1.0 \cdot 10^{-3}$	Winding Power [kW]	0.47
$R_{\text{heatsink}}$ [K/W]	$1.67 \cdot 10^{-3}$	Brake Power [kW]	60
Heat Sink LFM [m.min <sup>-1</sup> ]	500		

Table 3.8. Temperature findings for 60kW continuous brake operation at 800 min<sup>-1</sup>

Location	Temperature °C
Ambient	25
Disc	185
Winding	156
Inside Air	72
Rotor	125

## 4. RESULTS

### 4.1. Final Geometry and Parameters of Designed ECB

After performed FE analysis and analytical calculations final parameters of proposed ECB is determined as in Table 4.1.

Table 4.1. Final Design for proposed ECB

Parameter	Value
Axial Length	350 mm
Rotor Yoke $r_i$	134 mm
Rotor Yoke $r_o$	119 mm
Stator Tooth Length	27.3 mm
Stator Yoke $r_o$	60 mm
Stator Yoke $r_i$	75mm
Air Gap Distance	1.5 mm
Disc Thickness	1.5 mm
Nominal Speed	664 $\text{min}^{-1}$
Disc Material	Alu 220 Alloy
Core Material	Steel 1010
Nominal Current density on windings	5A/ $\text{mm}^2$
Total Weight	224.6 kg
Total Volume	0.295 $\text{m}^3$

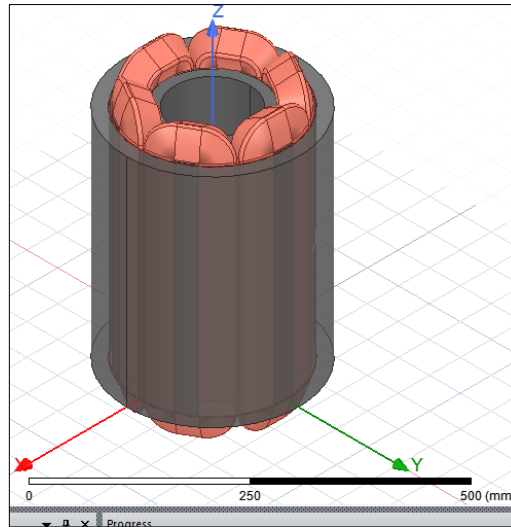


Figure 4.1. 3D View of designed ECB

In Figure 4.1, 3D model is seen. Rotor view is modified as semi-transparent for windings and stator tooth to be seen well.

#### 4.2. Controlling Proposed ECB by Constant Current

In Figure 4.2, torque speed curves of final design ECB with different excitations are seen. Increasing current density also increases torque curve and critical speed.

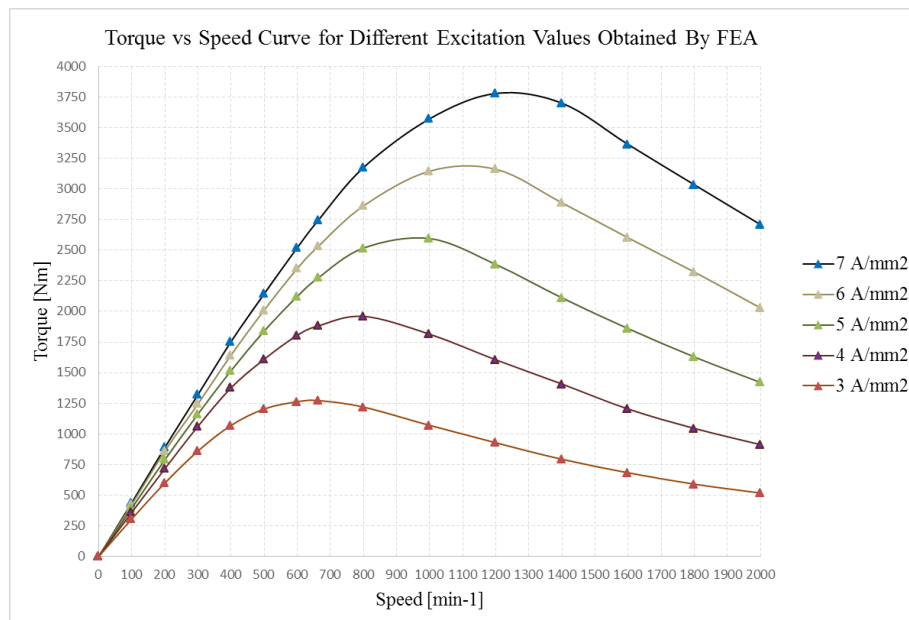


Figure 4.2. Torque speed curve for each current density ratio obtained by 3D FEA

However, the increase is not same for each graph line. For curves of  $3\text{A/mm}^2$ ,  $4\text{A/mm}^2$  and  $5\text{A/mm}^2$ , increase in linear region is proportional to square of current. After  $5\text{A/mm}^2$ , the ratio decreases due to saturation at core. The other effect of increased current density is that it causes armature reaction to be dominant at higher speed. Hence, increasing current density also increases critical speed.

### **4.3. Results and Conclusions**

#### **4.3.1. Performed analysis**

Analysis are performed in condition that simulation end time is 0.1 second, time step is 0.0001 second, 2D finite element method is used for proposed ECB. At 100, 200, 300, 400, 500, 600, 664, 800, 1000, 1200, 1400, 1600, 1800, 2000  $\text{min}^{-1}$  values, simulations are repeated. The rpm range is determined according to the truck speed limits. Ansys Maxwell 2D FE software is used. Steady state torque result of the simulation is used on comparison graphs.

For prototype version, simulation end time is 0.1 second, time step is 0.0001 second, and 3D finite element method is used. The prototype version of work data is less than proposed geometry due to execution time difference of 2D and 3D FE analysis.

For final geometry of proposed ECB 3D FE analysis are performed in condition that simulation end time is 0.1 second, time step is 0.0001 second, and speed is 664  $\text{min}^{-1}$  which is equal to 25 km/h in the truck. The results are shown in this chapter. Simulations and analytical calculations of geometrical variations are performed procedural way which is shown in Figure 4.3. At the beginning, average geometrical parameter is defined according to average production limitation such as disc thickness, airgap length. Then simulations and analytical calculations are initiated with the parameters. Then in each step, best parameter is selected for next step. The success of the procedure is shown in Figure 4.4. Torque/volume ratio increases beyond required value. However, the design ECB should not be used beyond 60kW power brake continuously because beyond thermal limitations, high temperature can cause windings faults and mechanical faults.

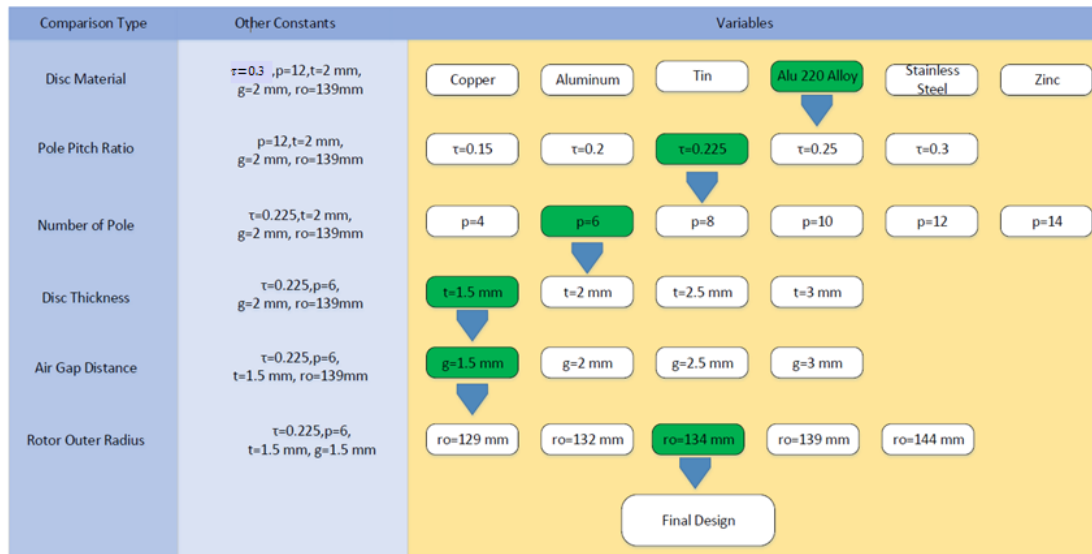


Figure 4.3. Performed analysis

### 4.3.2. Results

As seen Figure 4.3, horizontal line describes geometrical variations steps. There is an initial geometry. After each step, maximum torque/volume ratio and critical speed

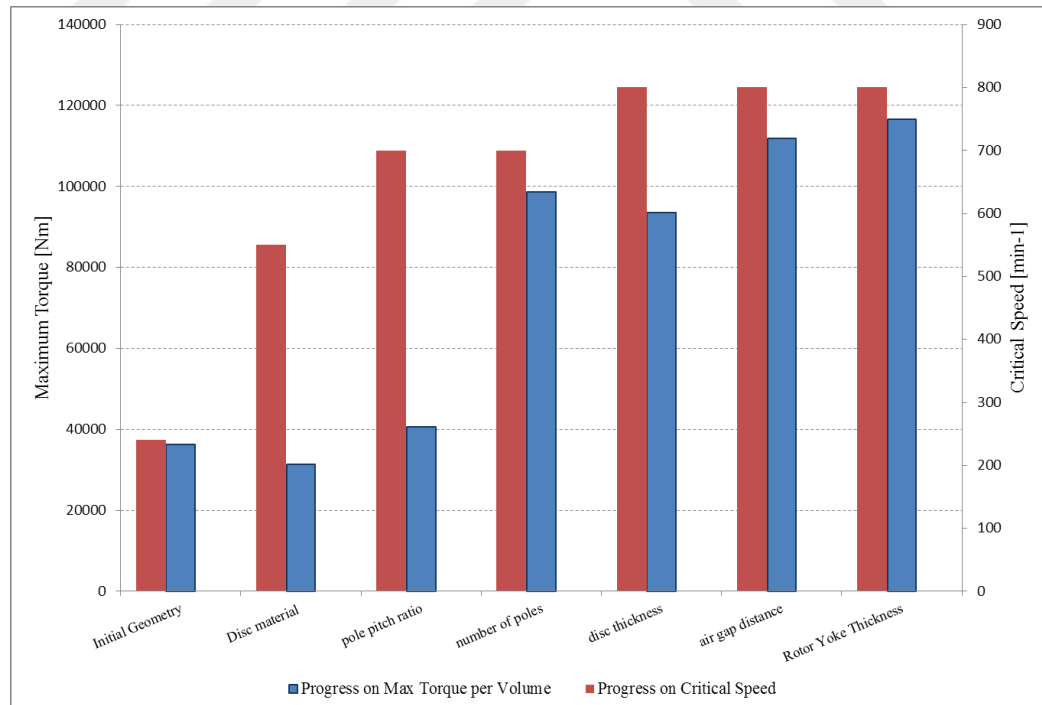


Figure 4.4. Geometrical variation result for each step

values are changing. In other words, the graph is a visual summary of the variation results. 900 Nm at 664 min<sup>-1</sup> are the brake requirements. However, the results show

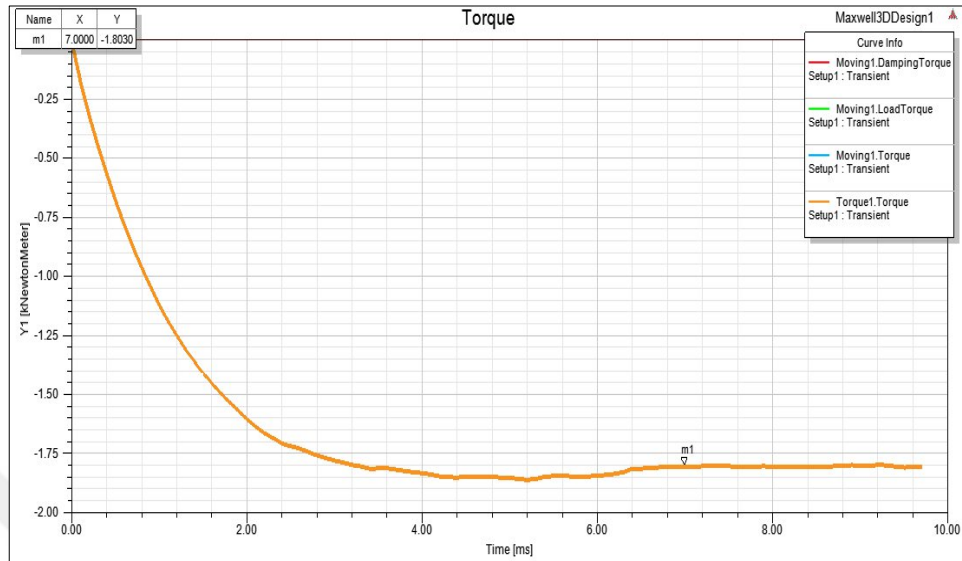


Figure 4.5. Torque vs time response curve obtained by 3D FEA

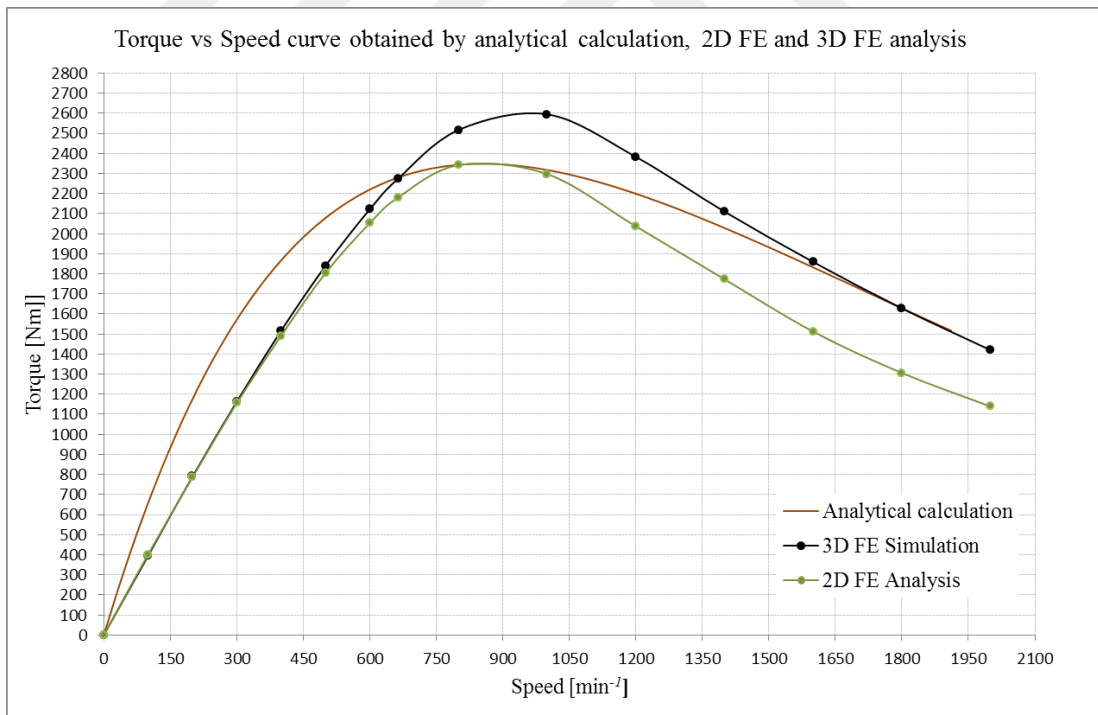


Figure 4.6. Comparison of the torque speed curve for 2D FE, 3D FE and analytical calculation



that for the volume, according to magnetic analysis, much more power than requirement can be achieved. In other words, the limiting factor is not magnetic properties of the proposed ECB. The limiting factors are mechanical factors and thermal factors. They dominate the maximum brake torque. Response time of secondary brake is another important parameter. In Figure 4.5, torque vs response time is seen. It takes 3 milliseconds to reach steady state. Due to this short reaction time, as mentioned before, ECB brakes have great advantages than hydraulic retarders. In Figure 4.6, comparison of 2D FE, 3D FE and analytical calculations are seen for final geometry. As seen from the three curves, critical speed values are nearly same. At linear region, while 2D and 3D FE analysis are quite same, analytical approach has some error because saturation effect is neglected. In linear region, independent of Reynolds number approach  $B_0$  can be used constant. At stable region, while 2D FEA and analytical approach is quite similar, 3D FEA has higher values. It is resulted from fringing effect on axial direction. 3D geometry has a larger gap area and lower gap reluctance. Hence, with constant magneto motive force, flux density in airgap becomes larger. Proportional to square of magnetic flux density in airgap, output torque of the ECB is changing. At reduction region, 3D FEA and 2D FEA difference.

Table 4.2. Comparison of the Retarders

	Power-Mela Discharge Resistor	Super Capacitor [51]	Telma A50 90	Hydraulic Retarder	Proposed Design
Power density [W/kg]	1428	1600	720	1016	267
Volume [m <sup>3</sup> ]	0.06	0.042	0.034	0.065	0.295

Table 4.2. (Continued) Comparison of the retarders

Brake Limitation	Thermal low speed	High SOC low speed	Thermal and low speed	Thermal, hydraulic leakage, low speed	Thermal and low speed
Voice	quiet	quiet	quiet	noisy	quiet
Complexity	low	high	medium	high	high
Response time	low	low	low	high	low

is resulted from the same reason at stable region. However, 2D FEA and analytical calculation difference is resulted from nonlinear characteristics of core material. As

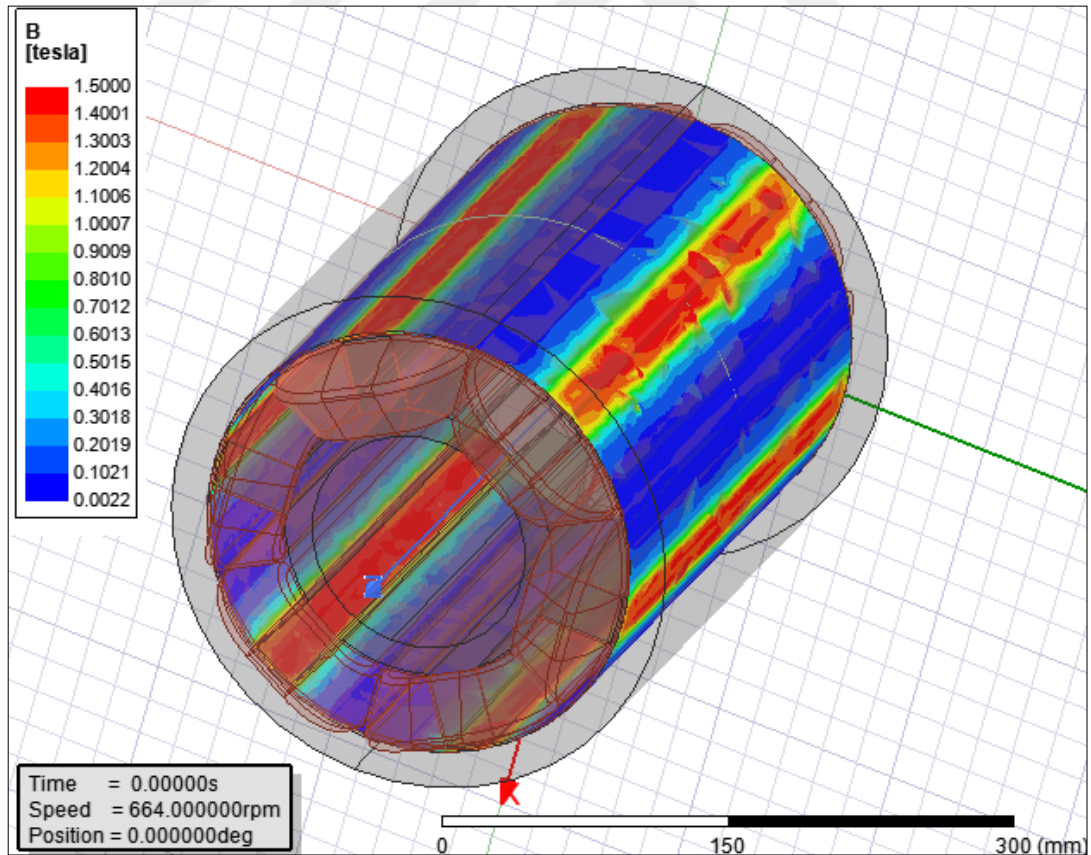


Figure 4.7. Flux density on the disc at t=0 obtained by FEA

mentioned before, to correct output torque curves for saturated ECB geometries, magneto motive force is divided by 0.6 which is equal to  $e^{-R_m}$  at critical speed. Hence, at maximum torque point, armature reaction is eliminated by saturation and results are corrected. However, in reduction region saturation cannot eliminate the armature reaction, hence compensation magneto motive force which is added, causes the results be higher. In table 4.2, comparison of five different retarder systems is shown. These are RFEE-ECB, AFEE-ECB with LV, discharge resistor, super capacitor and hydraulic retarders. As seen maximum power density belongs to super capacitor yet high SOC limitation of capacitor is critical parameter. Second highest power density belongs discharge resistor module. As a volume or packaging factor, Telma ECB has advantages. Hydraulic retarder has significant disadvantages due to high noise, high complexity and low response time. According to the table, most feasible brake module is discharge resistor. As a second alternative axial ECBs may be a good option.

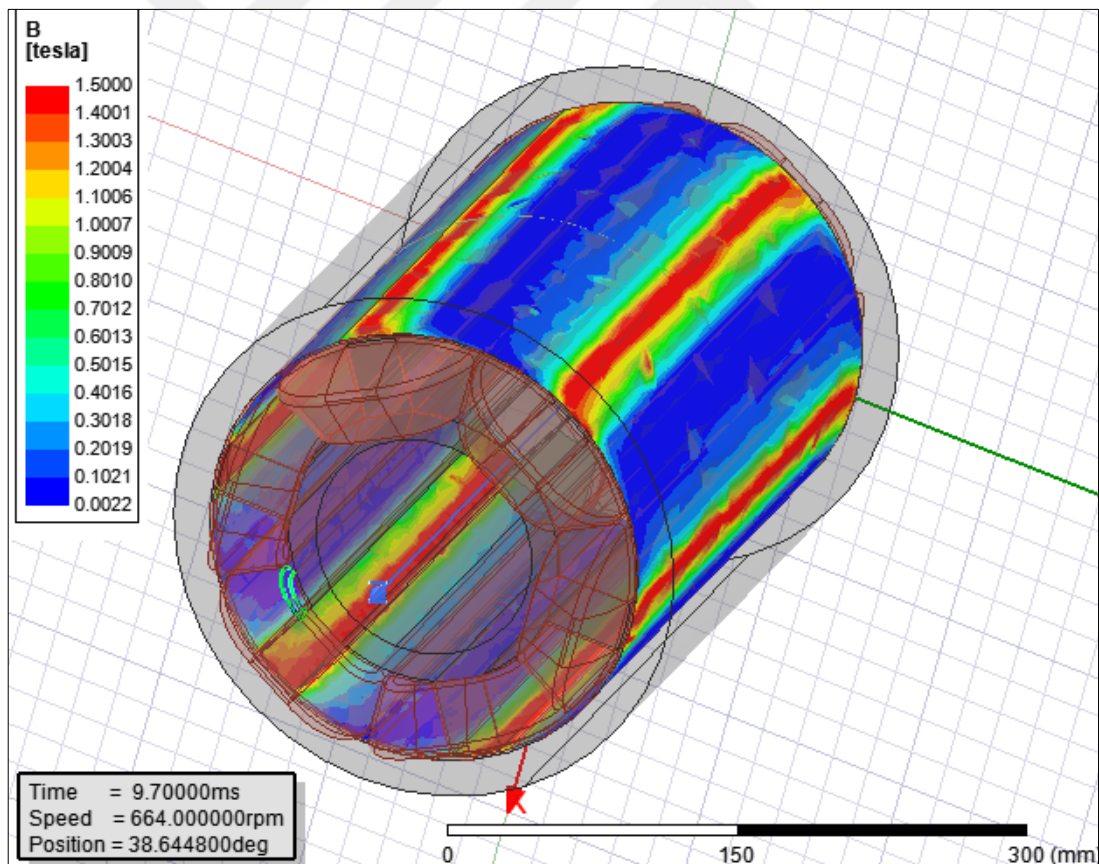


Figure 4.8. Flux density on the disc at t=9.7ms steady state obtained by FEA

In Figure 4.7, and In Figure 4.8; flux densities at  $t=0$  and  $t=9.7$  ms are seen. At  $t=0$ , while the flux density is trapezoidal, at steady state the shape changes into triangular shape. This is due to armature reaction on the disc. Increasing eddy current on disc opposes the main flux and changes it.

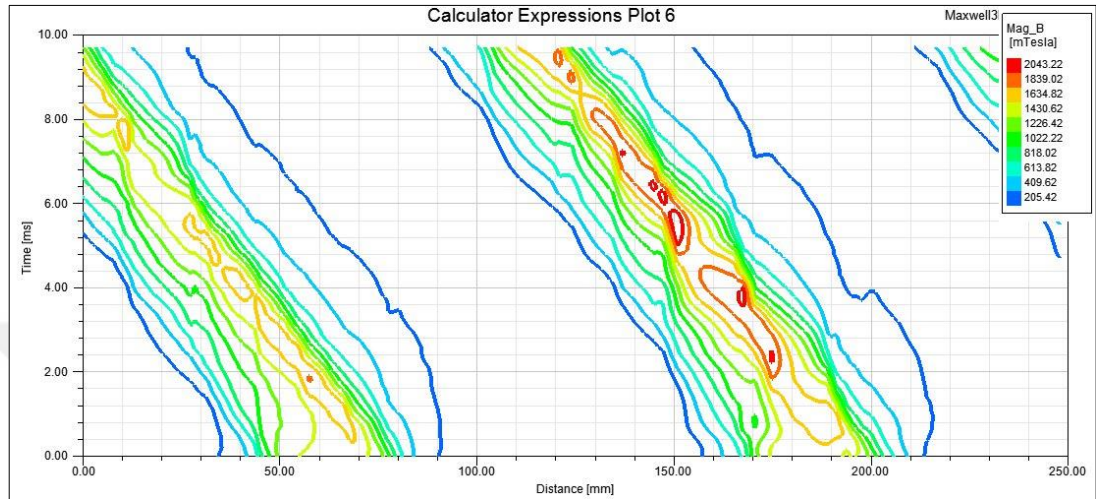


Figure 4.9. Contour drawing of the flux density on a line in the middle of the disc at  $664 \text{ min}^{-1}$  obtained by FEA

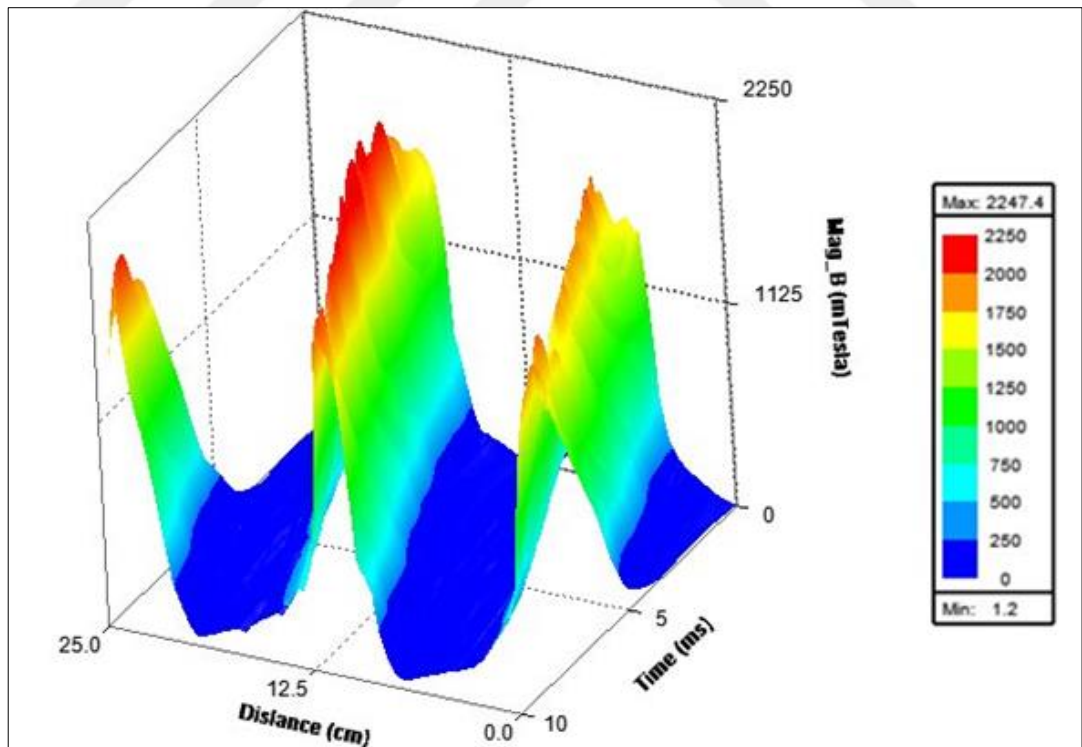


Figure 4.10. 3D drawing of the flux density on the line at  $664 \text{ min}^{-1}$  obtained by FEA

There is more detailed graph in Figure 4.9. In simulation, a line centered in the disc is located. That line covers two poles. Then absolute flux density on that line is

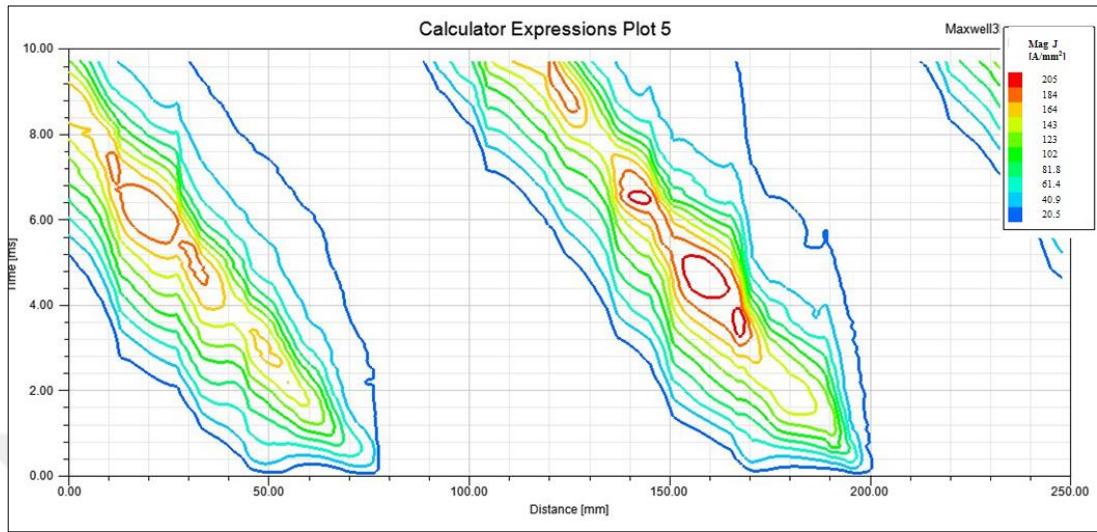


Figure 4.11. Contour drawing of the eddy current density on the line at  $664 \text{ min}^{-1}$  obtained by FEA

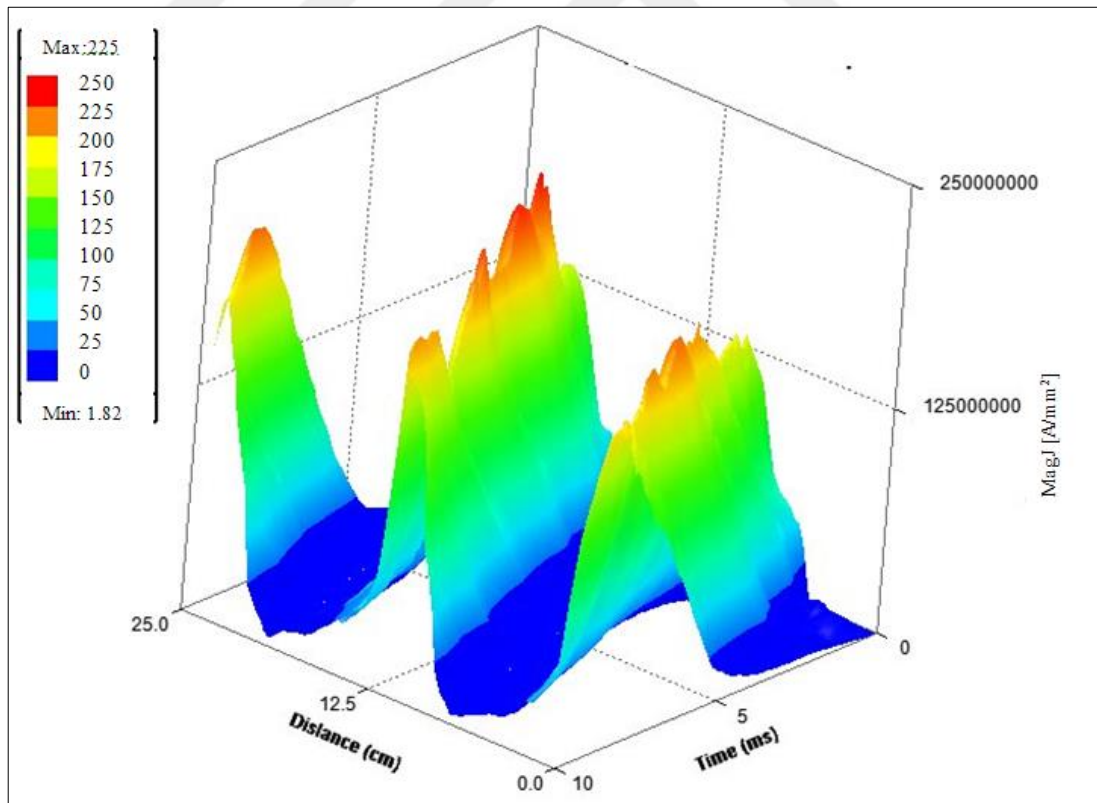


Figure 4.12. 3D drawing of the Eddy Current on the line at  $664 \text{ min}^{-1}$  obtained by FEA

drawn. As seen, initially flux lines in trapezoidal shape and at the same level with stator tooth. With increasing speed, both shape of the flux density changes and form a flux density shift through movement direction. Figure 4.10 is the same graph with Figure 4.9 as different drawing version. If the Figure 4.9 and Figure 4.11 are compared, armature reaction relation would be observed. At  $t=0$  there is no generated eddy current on disc and there is no deterioration on the flux density shape.

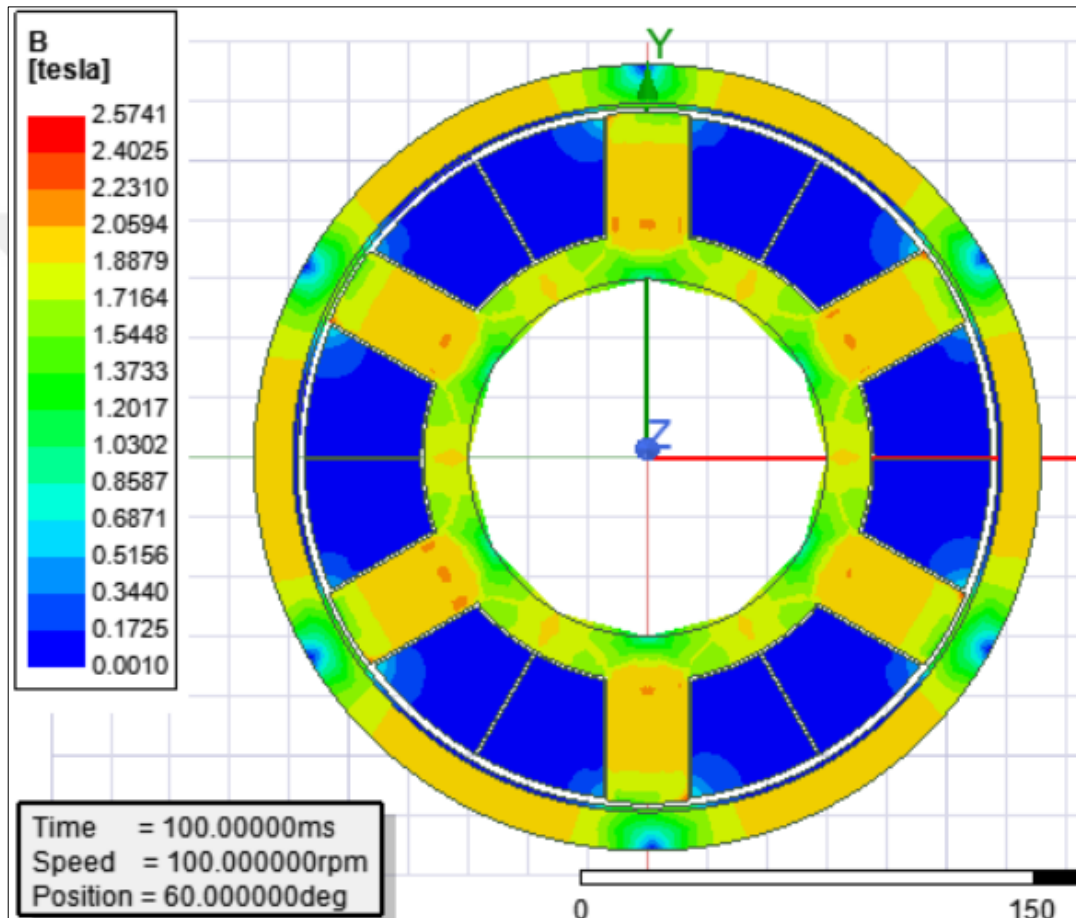


Figure 4.13 Magnetic flux density in the stator core at  $100 \text{ min}^{-1}$  obtained by FEA

With increase of eddy current, both maximum flux density decreases and shifts through direction of movement of the disc. Figure 4.12 is the same graph with Figure 4.11 as different drawing version. In Figure 4.7, and In Figure 4.8; flux densities in the stator core at  $100 \text{ min}^{-1}$  and at  $664 \text{ min}^{-1}$  are seen. At  $100 \text{ min}^{-1}$ , stator core is highly saturated. while armature reaction increases with increasing speed, saturation in the stator teeth decreases due to increasing armature reaction. To see the eddy current vector directions, Figure 4.13 and Figure 4.14 are drawn with some hidden parts such

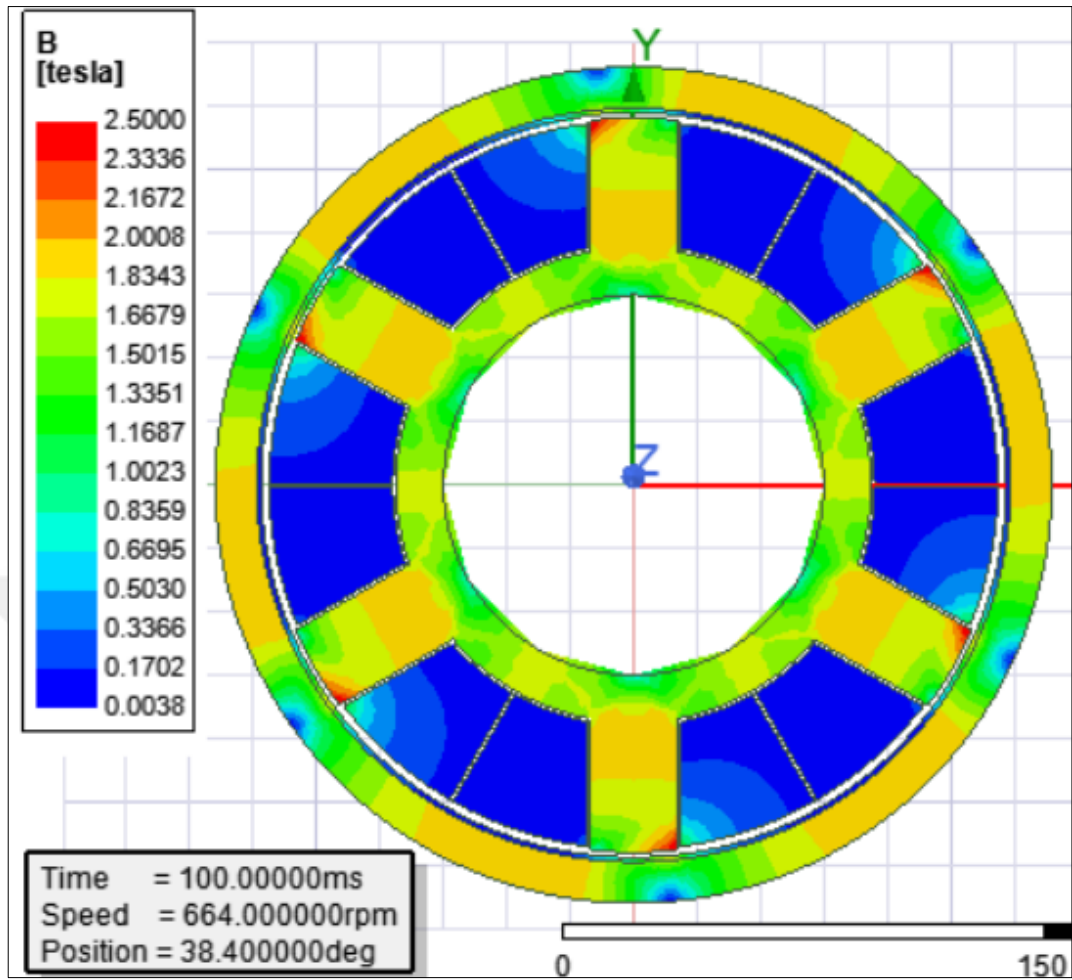


Figure 4.14. Magnetic flux density in the stator core at  $664 \text{ min}^{-1}$  obtained by FEA

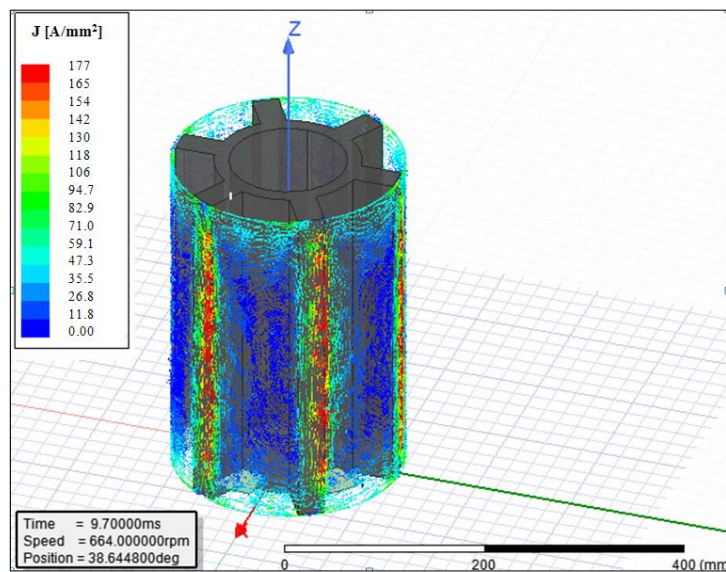


Figure 4.13. 3D view of eddy current vectors obtained by FEA

as rotor yoke and disc. In Figure 4.15, 3D drawing of eddy current vectors for the small scaled of the ECB is seen. As a brief, considering right hand rule, three magneto motive sources exist on the ECB. First is on the tooth excited by winding current. Second is eddy current generated on the disc at right edge of the tooth. Third is eddy current

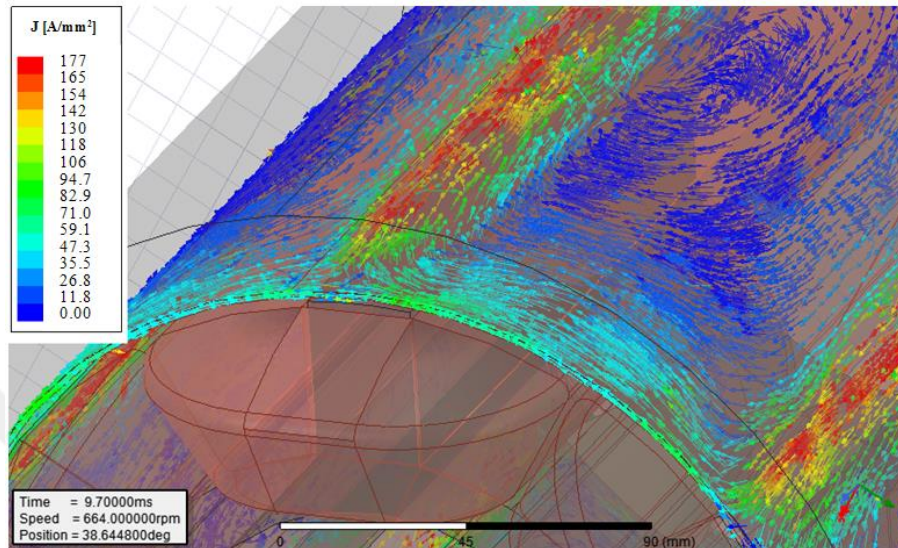


Figure 4.14. Closer 3D view of eddy current vectors obtained by FEA

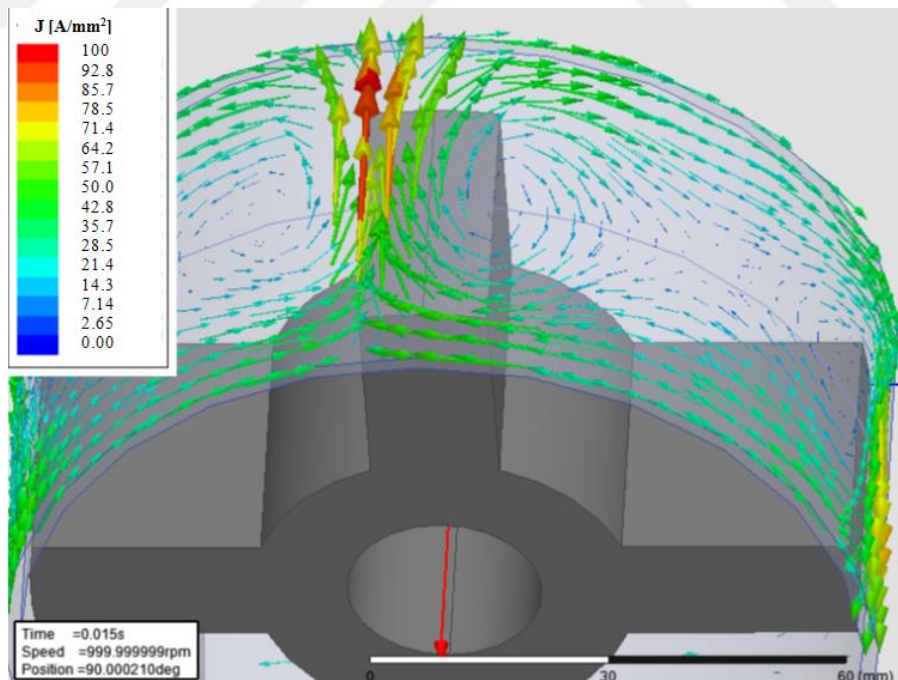


Figure 4.15. 3D drawing of eddy current vectors for the small scaled of the ECB obtained by FEA



generated on the disc at left edge of the tooth. If these three circulating currents are thought as if magnet, braking mechanism can be understood easily. Magnet at stator is pushed back by second magnet on the rotor and pulled by third magnet on the rotor. The polarity of the magnets on rotor is changing by the movement direction of the rotor.



## 5. CONCLUSIONS AND FUTURE WORKS

Design of proper and safe ECB for fully electric truck is performed. The brake module provides better and safer solution than other brake mechanism. The R13 regulation may be fully covered by the solution. The design results also show that an ECB module supplied by high voltage source, with reasonable power/volume is possible for EV truck.

The disadvantage of the proposed ECB is that it is not capable to brake sufficiently at low speed and too high speed. If adjusted time varying current is applied coils instead of DC current, ECB can brake at every speed in range of maximum torque [52]. In future works, the control method of designed ECB may be worked in more detailed.

The other disadvantages of the system are that power density is low compared to discharge resistor. The mechanical integration of the system is much more complicated than discharge resistor and supercapacitor systems.

As a result, comparing to new generation secondary brake system, proposed system has high cost, high weight, high volume and high density. To use the system is not feasible. However, the proposed system is still superior to hydraulic retarder and to ECB supplied by low voltage battery. It is quieter, safer and faster than hydraulic retarder. It is more feasible than LV ECB due to voltage source.

Due to rotating heat sink will create vacuum effect, it will also affect heat sink thermal conduction ratio. It will affect directly thermal resistance of the heat sink, temperature on disc. Then it will affect resistance of the disc and maximum torque capability of the designed ECB. To have concrete results, thermal and fluent CFD works may be performed in future works.

Also, Fan has a significant effect on thermal resistance. It has a cfm value changing by propelled design. In future, propeller design may be performed by FE analysis tools.

A new heat sink design may be performed. Heat sink can have a both fan propeller and heat sink function. With that design there may be no extra fan blade coupled by axle. After these advanced simulations, experimental observation may be performed or without the advanced simulations, to have know-how, experimental setup may be performed to collect academics data.



## REFERENCES

- [1] URL-1: <https://www.who.int/sustainable-development/transport/health-risks/climate-impacts/en/> (Accessed on: 29.09.2019).
- [2] Song, M., Zhu, D., Zhang, L., Wang, X., Chen, Y., Mi, R., ... Lau, L. W. M. (2013). Improved charging performances of Li<sub>2</sub>O<sub>2</sub> cathodes in non-aqueous electrolyte lithium-air batteries at high test temperatures. *2013 International Conference on Materials for Renewable Energy and Environment*. doi:10.1109/icmree.2013.6893723.
- [3] Wilcke, W. W., & Kim, H.-C. (2016). The 800-km battery lithium-ion batteries are played out. Next up: lithium-air. *IEEE Spectrum*, **53**(3), 42–62. doi:10.1109/mspec.2016.7420398.
- [4] Proposal for draft amendments to regulation No. 13 (Braking).UK GRRF-56-2, 22 September 2004.
- [5] Mendonca, P., da Silva, J. F. A., Sousa, D. M., & Pinto, S. F. (2014). An approach to recover braking energy of a tram. *2014 IEEE 5th International Symposium on Power Electronics for Distributed Generation Systems (PEDG)*. doi:10.1109/pedg.2014.6878708.
- [6] Li, Y., Zhang, J., Lv, C., Kong, D., & He, C. (2013). Research of Regenerative Braking System for Electrified Buses Equipped with a Brake Resistor. *2013 IEEE Vehicle Power and Propulsion Conference (VPPC)*. doi:10.1109/vppc.2013.6671704.
- [7] Albertz, D., Dappen, S., & Henneberger, G. (1996). Calculation of the 3D nonlinear eddy current field in moving conductors and its application to braking systems. *IEEE Transactions on Magnetics*, **32**(3), 768–771. doi:10.1109/20.497353.
- [8] Li, P., Ma, J., & Fang, Y. (2011). Design and analysis of hybrid excitation rail eddy current brake system of high-speed train. *Proceedings of 2011 IEEE International Conference on Service Operations, Logistics and Informatics*. doi:10.1109/soli.2011.5986624.
- [9] Gulbahce, M. O., Kocabas, D. A., & Nayman, F. (2013). Investigation of the effect of pole shape on braking torque for a low power eddy current brake by finite elements method. *2013 8th International Conference on Electrical and Electronics Engineering (ELECO)*. doi:10.1109/eleco.2013.6713844
- [10] URL-2: [www.telma.com/produits/fonctionnement](http://www.telma.com/produits/fonctionnement). (Accessed on: 29.09.2019).

- [11] Gay, E. "Contactless magnetic brake for automotive applications." Ph.D. thesis, University of Texas, USA, 2005.
- [12] Karakoc, K. (2019). Design of a Magnetorheological Brake System Based on Magnetic Circuit Optimization.
- [13] Fallah, S. (2014). Electric and Hybrid Vehicles - Technologies, Modeling and Control: A Mechatronic Approach..
- [14] Meistrick, Z., "Jacobs New Engine Brake Technology," SAE Technical Paper 922448, 1992.
- [15] URL-3: [https://www.jacobsvehiclesystems.com/sites/default/files/2018-08/jacobs\\_vehicle\\_systems\\_HPDP\\_sellsheet.pdf](https://www.jacobsvehiclesystems.com/sites/default/files/2018-08/jacobs_vehicle_systems_HPDP_sellsheet.pdf) (Accessed on: 03.11.2019).
- [16] EXHAUST BRAKING SYSTEM-REVIEW PAPER, *International Journal of Innovative Research in Technology*([www.ijirt.org](http://www.ijirt.org)) ,ISSN: 2349-6002 ,Volume 4 ,Issue 10 ,Page(s):261-264 ,March 2018.
- [17] URL-4: [https://www.jacobsvehiclesystems.com/sites/default/files/2018-09/Exhaust\\_Brake\\_Sellsheet.pdf](https://www.jacobsvehiclesystems.com/sites/default/files/2018-09/Exhaust_Brake_Sellsheet.pdf) (Accessed on: 03.11.2019).
- [18] Zheng, H., Lei, Y., & Song, P. (2017). Hydraulic retarders for heavy vehicles: Analysis of fluid mechanics and computational fluid dynamics on braking torque and temperature rise. *International Journal of Automotive Technology*, **18**(3), 387–396. doi:10.1007/s12239-017-0039-z.
- [19] URL-5: <https://d2euiryrvxi8z1.cloudfront.net/asset/445934742530/a94351daf63d92ba2baa676a778f95e5> (Accessed on: 03.11.2019).
- [20] URL-6: <https://www.telmausa.com/Downloads/OC442066.pdf> (Accessed on: 03.11.2019).
- [21] Feng, Q. S., & Li, H. (2012). Design of Electric Vehicle Energy Regenerative Braking System Based on Super Capacitor. *Applied Mechanics and Materials*, 157-158, 149–153. doi:10.4028/www.scientific.net/amm.157-158.149.
- [22] Jin, L., Zheng, Y., Li, J., & Liu, Y. (2015). A study of novel regenerative braking system based on supercapacitor for electric vehicle driven by in-wheel motors. *Advances in Mechanical Engineering*, **7**(3), 168781401557376. doi:10.1177/1687814015573762.
- [23] Naseri, F., Farjah, E., & Ghanbari, T. (2016). An Efficient Regenerative Braking System Based on Battery/Supercapacitor for Electric, Hybrid and Plug-In Hybrid Electric Vehicles with BLDC Motor. *IEEE Transactions on Vehicular Technology*, 1–1. doi:10.1109/tvt.2016.2611655.

- [24] Garcia, P., Fernandez, L. M., Garcia, C. A., & Jurado, F. (2010). Energy Management System of Fuel-Cell-Battery Hybrid Tramway. *IEEE Transactions on Industrial Electronics*, **57**(12), 4013–4023.
- [25] URL-7: [https://secureservercdn.net/184.168.47.225/ec2.afe.myftpupload.com/wp-content/uploads/2019/08/68190\\_power\\_MELA\\_BC.pdf](https://secureservercdn.net/184.168.47.225/ec2.afe.myftpupload.com/wp-content/uploads/2019/08/68190_power_MELA_BC.pdf) (Accessed on: 07.11.2019).
- [26] Smythe, W. R. (1942). On Eddy Currents in a Rotating Disk. *Transactions of the American Institute of Electrical Engineers*, **61**(9), 681–684.
- [27] Singh, A. (1977). Theory of eddy-current brakes with thick rotating disc. *Proceedings of the Institution of Electrical Engineers*, **124**(4), 373.
- [28] Hong-Je Ryoo, Jong-Soo Kim, Do-Hyun Kang, Geun-Hie Rim, Yong-Ju Kim, & Chung-Yuen Won. (n.d.). Design and analysis of an eddy current brake for a high-speed railway train with constant torque control. Conference Record of the 2000 IEEE Industry Applications Conference. Thirty-Fifth IAS Annual Meeting and World Conference on Industrial Applications of Electrical Energy (Cat. No.00CH37129).
- [29] Anwar, S. (2004). A Parametric Model of an Eddy Current Electric Machine for Automotive Braking Applications. *IEEE Transactions on Control Systems Technology*, **12**(3), 422–427.
- [30] Liu, C. Y., Jiang, K. J., & Zhang, Y. (2011). Design and use of an eddy current retarder in an automobile. *International Journal of Automotive Technology*, **12**(4), 611–616.
- [31] Sharif, S., Faiz, J., & Sharif, K. (2012). Performance analysis of a cylindrical eddy current brake. *IET Electric Power Applications*, **6**(9), 661.
- [32] Wang, J., Lin, H., & Fang, S. (2016). Analytical Prediction of Torque Characteristics of Eddy Current Couplings Having a Quasi-Halbach Magnet Structure. *IEEE Transactions on Magnetics*, **52**(6), 1–9.
- [33] Gulec, M., Yolacan, E., & Aydin, M. (2016). Design, analysis and real time dynamic torque control of single-rotor–single-stator axial flux eddy current brake. *IET Electric Power Applications*, **10**(9), 869–876.
- [34] Gulec, M., & Aydin, M. (2016). Modelling and analysis of a new axial flux permanent magnet biased eddy current brake. *2016 XXII International Conference on Electrical Machines (ICEM)*.
- [35] Cho, S., Liu, H.-C., Ahn, H., Lee, J., & Lee, H.-W. (2017). Eddy Current Brake With a Two-Layer Structure: Calculation and Characterization of Braking Performance. *IEEE Transactions on Magnetics*, **53**(11), 1–5.

- [36] Tarvirdilu Asl, Rasul & YÜKSEL, HÜSEYİN & keysan, ozan. (2019). Multi-objective design optimization of a permanent magnet axial flux eddy current brake. *Turkish Journal of Electrical Engineering and Computer Sciences*. 27. 998-1011. 10.3906/elk-1802-65.
- [37] Jin, Y., Kou, B., Li, L., & Pan, D. (2018). Thermal Analysis of a Hybrid Excitation Linear Eddy Current Brake. *IEEE Transactions on Industrial Electronics*, 1–1.
- [38] URL-8: <https://www.volvotrucks.com.tr/tr-tr/trucks/volvo-fmx.html> (Accessed on: 29.09.2019).
- [39] URL-9: [https://www.tm4.com/wp-content/uploads/2019/05/TM4-SUMO-HD\\_web-brochure.pdf](https://www.tm4.com/wp-content/uploads/2019/05/TM4-SUMO-HD_web-brochure.pdf) (Accessed on: 29.09.2019).
- [40] Andersson, R. (2012). Online Estimation of Rolling Resistance and Air Drag for Heavy Duty Vehicles.
- [41] Pyrhonen, J., Jokinen, T. and Hrabovcova, V. (2014). *Design of Rotating Electrical Machines*. 2nd ed. Chichester: Wiley, p.284.
- [42] URL-10: <https://www.simscale.com/docs/content/simwiki/numerics/what-is-the-reynolds-number.html> (Accessed on: 21.11.2019).
- [43] URL-11: <https://www.wikizeroo.org/index.php?q=aHR0cHM6Ly9lbi53aWtpcGVkaWEub3JnL3dpa2kvUmV5bm9sZHNfbnVtYmVy> (Accessed on: 21.11.2019).
- [44] URL-12: <https://www.wikizeroo.org/index.php?q=aHR0cHM6Ly9lbi53aWtpcGVkaWEub3JnL3dpa2kvTWFnbnV0aWNfUmV5bm9sZHNfbnVtYmVy> (Accessed on: 21.11.2019).
- [45] URL-13: <https://www.sfu.ca/~mbahrami/ENSC%20388/Notes/Steady%20Conduction%20Heat%20Transfer.pdf> (Accessed on: 29.09.2019).
- [46] Gulec, M., Aydin, M., Lindh, P., & Pyrhonen, J. (2018). Investigation of Braking Torque Characteristic for a Double-Stator Single-Rotor Axial-Flux Permanent-Magnet Eddy-Current Brake. *2018 XIII International Conference on Electrical Machines (ICEM)*. doi:10.1109/icelmach.2018.8506890.
- [47] URL-14: <http://protolam.com/> (Accessed on: 29.09.2019).
- [48] URL-15: <https://myheatsinks.com/calculate/plate-fin-heat-sink-calculator/> (Accessed on: 29.09.2019).
- [49] URL-16: <https://www.summitracing.com/int/parts/flx-398/overview/> (Accessed on: 29.09.2019).

- [50] URL-17: <https://www.engineering.com/calculators/airflow.htm> (Accessed on: 29.09.2019).
- [51] URL-18: [https://www.maxwell.com/images/documents/240V\\_3\\_75F\\_ds\\_3001973\\_da\\_tasheet.pdf](https://www.maxwell.com/images/documents/240V_3_75F_ds_3001973_da_tasheet.pdf) (Accessed on: 27.11.2019).
- [52] K. Karakoc, A. Suleman and E. J. Park, "Optimized Braking Torque Generation Capacity of an Eddy Current Brake With the Application of Time-Varying Magnetic Fields," in *IEEE Transactions on Vehicular Technology*, vol. 63, no. 4, pp. 1530-1538, May 2014.





## **PERSONAL PUBLICATIONS**

**M. B. Topcuoglu**, Z. Bingul and M. Gulec, "Design and Analysis of a Radial Flux Electrically Excited Eddy Current Brake," *2019 IEEE 28th International Symposium on Industrial Electronics (ISIE)*, Vancouver, BC, Canada, 2019, pp. 1498-1505.

Best Presentation List in Automotive Session *2019 IEEE 28th International Symposium on Industrial Electronics (ISIE)*, Vancouver, BC, Canada, 2019



## **CURRICULUM VITAE**

Mustafa Barış Topçuoğlu was born in Ankara in 1990. He graduated from Ankara Atatürk Anadolu High school in 2008. He graduated from Middle East Technical University, Electrical and Electronics Engineering in 2014. He has five years job experience. He began his Master education in Kocaeli University, Mechatronics Engineering in 2017. He is currently work on automotive company at electrical vehicle projects.

